Spring 2018

Adaptive data analysis for damage detection and system identification in civil infrastructure

Hongya Qu

Department: Civil, Architectural and Environmental Engineering

ADAPTIVE DATA ANALYSIS FOR DAMAGE DETECTION AND SYSTEM IDENTIFICATION IN CIVIL INFRASTRUCTURE

by

HONGYA QU

A DISSERTATION

Presented to the Faculty of the Graduate School of the

MISSOURI UNIVERSITY OF SCIENCE AND TECHNOLOGY

In Partial Fulfillment of the Requirements for the Degree

DOCTOR OF PHILOSOPHY

in

CIVIL ENGINEERING

2018

Approved by:

Genda Chen, Advisor
Neil L. Anderson
Mohamed ElGawady
Lesley H. Sneed
Guirong Yan

ABSTRACT

Time-varying structural systems are often encountered in civil engineering. As extreme events occur more frequently and severely in recent years, more structures are loaded beyond their elastic conditions and may thus experience damage in the years to come. Even if structures remain elastic, energy dissipation devices installed on structures often reveal hysteretic behaviors under earthquake loads. Therefore, it is imperative to develop and implement novel technologies that enable the identification and damage detection of time-varying systems. In this dissertation, adaptive wavelet transform (AWT) and multiple analytical mode decomposition (M-AMD) are proposed and applied to identify system properties and detect damage in structures. AWT is an optimized time-frequency representation of dynamic responses for the extraction of features. It is defined as an average of overlapped short-time wavelet transforms with time-varying wavelet parameters in order to extract time-dependent frequencies. The effectiveness of AWT is demonstrated by various analytical signals, acoustic emission and impact echo responses. M-AMD is a response decomposition method for the identification of weakly to moderately nonlinear oscillators based on vibration responses. It can be used to accurately separate the low and high frequency components of time-varying stiffness and damping coefficients in dynamic systems. The efficiency and accuracy of the proposed M-AMD are evaluated with three characteristic nonlinear oscillators and a ¼-scale 3-story building model with frictional damping under seismic excitations. Finally, AWT-based M-AMD is applied to decompose the measured dynamic responses of a 1/20-scale cable-stayed bridge model tested on four shake tables and evaluate the progression of damage under increasing earthquake loads.

ACKNOWLEDGMENTS

I would like to express sincere thanks to Dr. Genda Chen for his insightful advice, careful guidance, constant encouragement and generous support during the development of this research work. I am also indebted to the committee members: Dr. Neil L. Anderson, Dr. Mohamed ElGawady, Dr. Lesley H. Sneed and Dr. Guirong Yan. Their valuable suggestions and comments are essential to the accomplishment of the work.

Financial support to complete this study was provided in part by the U.S. National Science Foundation under Award No. CMMI1538416 and by the Missouri University of Science and Technology. The findings and results presented in this dissertation are those of the author only, and do not necessarily represent those of the sponsors. In addition, shake table test data of the 1/20-scale cable-stayed bridge model were provided by Professor Jianzhong Li from Tongji University, Shanghai, China.

I would like to express my sincere gratitude to the strong support received over the years from the Department of Civil, Architectural, and Environmental Engineering at Missouri S&T. Thanks are also due to Dr. Chen's students and visiting scholars for their support and assistance during various research tasks.

Last, but not the least, I would like to express eternal gratitude to my wife and parents for their everlasting love and support.

TABLE OF CONTENTS

Page

LIST OF ILLUSTRATIONS

Page

LIST OF TABLES

Page

1. INTRODUCTION

1.1. STRUCTURAL HEALTH MONITORING

Structural health monitoring (SHM) is the process of implementing a damage detection and characterization strategy for engineering structures. As a popular research subject for decades, SHM aims to provide a prognosis and diagnosis tool for structural condition at any moment during the service life of an engineering structure. It includes four stages: (1) detecting the existence of damage in the structure, (2) locating the damage, (3) identifying the types of damage, and (4) quantifying the severity of the damage. All the stages revolve around the advanced knowledge of sensor deployment, data acquisition, signal feature extraction, and condition evaluation.

Techniques in SHM can be classified into two categories: local and global. For the local approach, it is often referred to as nondestructive evaluation, which includes acoustic emission, impact echo, and infrared thermography inspection. These methods require that the portion of a structure being inspected must be accessible. Due to these limitations, they are often limited to the damage detection on or near the surface of the structure. The global approach, however, is to assess the system condition of complex structures, and it generally observes the changes in the vibration features of these structures.

For both local and global approaches, the identification of application specific data features that allows the damage to be identified is the most important process and receives the most attention from the researchers. This is due to the reason that all the four stages of the SHM process rely on a robust data interpretation method. Common features can be extracted from measured system responses with signal processing techniques in time domain, frequency domain or time-frequency domain.

1.2. SIGNAL PROCESSING TECHNIQUES

Extracting components and associated features from a measured dynamic signal is one of the critical steps in SHM. Stationary signals with time-invariant features can be decomposed using simple filtering techniques. However, signals such as wind-induced vibration and earthquake responses may not be stationary. In such a case, time-varying parameters must be identified in order to capture instantaneous characteristics. The techniques that are used for nonstationary signal analysis can generally be divided into two categories: representation and decomposition.

Representation is a method to show the variation of a parameter over time from a signal. The time-frequency representation of a signal is a typical example. Whereas, decomposition is to separate a signal into individual components for further analysis. The empirical mode decomposition (EMD) [1] and analytical modal decomposition (AMD) [2] are typical examples. The two categories are sometimes combined to achieve a complete signal analysis. Daubechies et al. [3] developed the synchro-squeezed wavelet transform (SSWT) and combined it with EMD to extract time-varying features, and Chen and Wang [2] developed and utilized AMD together with wavelet transform for signal decomposition. To better understand a signal, signal representation and decomposition are both important in acquiring the crucial characteristics hidden in an original signal.

1.2.1. Signal Representation. For time-frequency representation, many signal processing techniques have recently been proposed and used in practical applications. They include short time Fourier transform (STFT) [4], Wigner-Ville distribution (WVD) [5], Hilbert transform [1, 6, 7] and continuous wavelet transform (CWT) [8-10]. These techniques have their own advantages and disadvantages. STFT can capture the basic time-

frequency features of a signal with different window lengths for better time or frequency resolution, but fail to yield both resolutions simultaneously due to the Uncertainty Principle and fixed window length at each transform. WVD has the highest energy concentration, but is relatively difficult to yield instantaneous frequency characteristics. By introducing a scaling factor and a shifting factor, CWT can introduce high time resolution with a low scaling factor, and high frequency resolution with a high scaling factor at any given time. However, the time and frequency resolutions are often compromised for a desirable representation in time-frequency domain.

Adaptive wavelet concepts are widely used in signal processing techniques. Zhang and Benveniste proposed the Wavelet Neural Network (WNN) by combining the wavelet and neural network to adaptively capture desired features [11]. Genetic Algorithm (GA) has also been utilized to optimize the mother wavelet in some applications [12]. More recently, Nazimov et al. tried to optimize the central frequency and other coefficients of Morlet mother wavelet to gain better representation [13]. AMD analysis for time-variant features relies heavily on time-frequency representation techniques, particularly wavelet transform, and various optimization means of traditional wavelet transform are done by researchers. A wavelet ridge extraction method was proposed for instantaneous frequency identification [14]. SSWT was developed for more accurate time-frequency representation [3]. A further step was taken to propose a generalized synchro-squeezed transform to detect gear box faults [15].

1.2.2. Signal Decomposition. For signal decomposition, the Hilbert Transform method has received increasing attention in the field of system identification and damage detection [16-19] in the past two decades. Huang et al. developed the well-known Hilbert-

Huang Transform (HHT) method [1, 6, 20]. The HHT method was then applied into the detection of faults in mechanical systems [21, 22]. In combination with the random decrement technique, the natural frequencies and damping ratios of linear structures under ambient vibration were successfully identified [23, 24]. Based on the EMD, The time and location of damage were further determined by identifying the damage-induced response pulses due to a sudden change of structural stiffness [25]. A few investigators have attempted to address the mixed mode problem associated with the EMD. The minimum cutoff frequency criterion was established in the EMD sifting process to ensure that the frequency bandwidths of intrinsic mode functions are separated [26]. The subjective intervention to the EMD process may unintentionally distort the intrinsic mode functions. The wavelet packet transform was utilized to decompose a signal into a set of narrowband components [27]. A band-pass filter was applied on the measured free vibration time histories for the modal parameter identification of a multi-degree-of-freedom (MDOF) system [23, 24]. The waves' beating phenomena was taken advantage of to facilitate the EMD process [78]. A small intermittent fluctuation was decomposed from a large ocean wave by injecting a known time function into the original signal [29]. The wave-group method may not be applicable to flexible structures since their natural frequencies are already low. More recently, the singular value decomposition and band pass filtering techniques can be used to extract the parameters of closely-spaced modes [30]. As the space between two modal frequencies becomes small, the challenge of consistently and reliably identifying the properties of linear structures remains.

The EMD [1], Hilbert Vibration Decomposition (HVD) [7], and the AMD [2] allow the inclusion of both main and super harmonics. However, the HVD faces serious

challenges when applied to separate low amplitude harmonics from noises [31]. It is more suited to dealing with the free vibration of a SDOF system due to complications in mathematical formulation [32] while the EMD has the mode mixed problem in engineering applications with closely-spaced frequencies. Only the AMD is applicable to both cases.

1.3. NONDESTRUCTIVE EVALUATION APPROACHES

Nondestructive testing can be divided into various methods (e.g. acoustic emission, impact echo, Eddy-current, infrared and thermal testing) based on different scientific principles. These techniques, due to the unique principles, may find themselves well suited to certain applications. Thus, choosing the right method and technique is an important part of the performance of evaluation. Here, acoustic emission (AE) and impact echo (IE) methods are reviewed in detail, as they are of direct relevance to this study.

1.3.1. Acoustic Emission. For elevated structures, visual inspection as current practice in bridge maintenance can be subjective, difficult, expensive, dangerous, and disruptive. An attempt was thus made in early 1970s to apply AE into the detection, localization, and assessment of damage in highway structures [33]. Since then, further attempts have been made to understand damage mechanisms [34], detect fatigue-induced cracks in steel and concrete structures [35-37], evaluate reinforcement corrosion in reinforced concrete (RC) structures, and detect corrosion-induced cracks in RC structures [38-40].

As a nondestructive detection method, AE has been used for bridge cable monitoring due to its simplicity in sensor attachment and low attenuation [41-47]. In particular, Physical Acoustics Corporation tested the Anthony Wayne Bridge to

demonstrate the potential of AE technology in cable monitoring [48]. Most of these researchers analyzed AE waveform in time domain for the detection and identification of wire fracture [49-51], impact source [52], and inter-wire friction [53]. AE waveforms were also analyzed in frequency domain with the change in Fourier spectra [54]. To preserve key time-varying features in frequency domain, STFT and wavelet-based techniques were applied to verify modeling techniques [45], accuracy improvement of source localization algorithms [55], damage assessment of deteriorated RC structures [56], and denoising effect of filtering techniques [57]. Most, if not all, of these time-frequency analyses were applied to the AE signals of fiber reinforced polymer composite materials [58-60], and glass fiber reinforced polymer bridge cables [61]. Little has been done to understand the full potential of time-frequency analysis of AE signals for the extraction of pre-fracture features in damage prediction of steel cables and distinguish pre-fracture and fracture signals from fracture-induced echoes and noises so that false prediction and detection cases of wire fracture can be prevented.

1.3.2. Impact Echo. Corrosion, stress, or a combination of both can cause defects in concrete slabs such as delamination, voids, and cracks. If not treated in time, these defects would expand, influencing structural durability. Thus, the effectiveness of defect detection is of vital importance for maintenance strategy optimization. Among many techniques such as IE, short-wavelength penetrating radiation (x-rays and gamma rays), ground penetrating radar, microwave, and infrared thermography, IE proposed by Carino et al. [62] has been widely used and proven effective in structural geometry identification, flaw detection, and acoustic behavior of interfaces [63]. Its effectiveness was validated through testing of concrete slabs with artificial defects placed at predetermined locations

[64]. The IE method was applied to detect delamination [65, 66] and flaws in concrete slabs in combination with ultrasonic surface waves [67-69].

STFT, Gabor transform, and wavelet transform have recently been applied to analyze ultrasonic signals [70-72]. Among these time-frequency analysis methods, wavelet transform appears to be the most powerful and widely used [73]. Chiang and Cheng used the wavelet transform of IE signals to inspect steel and PVC tubes [74]. Shokouhi et al. showed that wavelet transform is more efficient than STFT for the extraction of time-frequency information from test data [72]. The marginal spectrum of wavelet transform was used together with Fourier transform to extract more accurate results in the frequency domain [75]. Epasto et al. also used the wavelet transform of IE signals for fire-damaged concrete evaluation [75]. Celaya et al. used a Portable Seismic Property Analyzer (PSPA) to assess debonding in concrete slabs with the aid of wavelet transform [77].

1.4. OBJECTIVES OF STUDY

The overall goal of this research work is to develop adaptive wavelet transform (AWT) and multiple analytical mode decomposition (M-AMD), and to enable the proper and wide application of these methods in various science and engineering disciplines. The main focus of this project are non-parametric identification of numerical signals and damage detection of time-varying systems including both linear structures with time-dependent properties and nonlinear structures without bifurcations, jumps, and chaotic behaviors.

To date, the AMD is a mathematically proven adaptive data analysis method for continuous time series. In engineering applications, however, structural responses are often

sampled at certain rate over a finite length of time. Their time-frequency characteristics are unknown before the AMD is applied, making it a challenge to select bisecting frequencies. These frequencies are key to the successful application of the AMD. However, how the sampling rate and finite length affect the decomposition accuracy has yet to be understood, quantified, and validated with experimental data from realistic structures.

A hypothesis is made to apply the AMD into the non-parametric identification and damage detection of a general structure. That is, AMD can accurately decompose each of the measured dynamic responses of a structure into many components that are mutually exclusive in frequency domain. For responses with time-dependent frequency characteristics, the frequency domain must be divided by time-varying bisecting frequencies. As the divided frequency ranges become so narrow that only one instantaneous mode of vibration is included in each range, a small perturbation of structural properties over time will be amplified in some of the narrowband components. As such, instantaneous system properties can be identified from the "zoom-in" components with high accuracy and high sensitivity to the causative perturbation, and their difference from those of a corresponding undamaged system can be used as an indicator for damage detection.

The specific objectives of this project include:

(1) Develop and characterize AWT for the determination of time-dependent frequencies so that optimal time-frequency resolution can be applied into every area of interest. Thus, AWT can be either used solely for time-frequency signal analysis or in combination with AMD for bisecting frequency extraction.

(2) Establish and evaluate a sampling rate and finite length criterion that guarantees an accurate decomposition of discrete time series, namely Optimized AMD.

(3) Derive the M-AMD algorithm based on the optimized algorithm, which gives a computationally efficient and accurate solution of the stiffness and damping coefficients of weakly-to-moderately nonlinear systems from free and forced vibration.

(4) Test the hypothesis and validate the robustness, accuracy, and efficiency of the AWT and M-AMD in system identification and damage detection of complex structures with different nonlinear mechanisms using shake table test data.

1.5. RESEARCH SIGNIFICANCE

Time-varying structural systems are commonly encountered in civil engineering. For example, long-span (flexible) bridges vibrate in complex mode shapes with closely-spaced natural frequencies that vary over time as vehicles or trains move across them. As extreme events such as earthquakes, hurricanes, tornados, and floods have occurred more frequently and severely in recent years, more buildings and bridges will be loaded beyond their in-service conditions and thus may experience structural damage such as concrete cracks, steel yielding and buckling in the years to come. Even if structures remain elastic under extreme events, due to the installation of more energy dissipation devices for protection from dynamic effects, the structure-device systems often reveal hysteretic behaviors. Therefore, it is imperative to develop and implement novel technologies that enable the identification and damage detection of such time-varying systems.

CWT is an advanced signal processing tool that gives a varying frequency resolution at each give time. It preserves accurate low frequency components and captures

transient high frequency features. However, there still exists the limitation of signal distortion for time-varying structural systems, when the wavelet parameters are optimized in the global sense in the current practice. Therefore, AWT is developed with time-varying mother wavelet parameters, which results in non-uniform time-dependent frequency characteristics. By taking advantage of the fully automatic parametric optimization algorithm based on CWT, an overlapping and averaging short-time wavelet transform or AWT with time-varying scaling factors and center frequencies in a complex Morlet wavelet is proposed for time series with strongly time-dependent frequencies.

AMD is a mathematically proven data analysis method for continuous time series. In engineering applications, signals obtained from sensors that monitor structural responses are often time-dependent and sampled over a finite time length. This poses a challenge for AMD: the finite discretized signals often distort AMD results to certain degree. Thus, how the bisecting frequency is selected and affects the decomposition accuracy together with sampling rate and finite length needs to be understood, quantified, and validated with experimental data from practical applications.

Identifying instantaneous modal parameters is crucial to observe structural abnormalities for nonlinear systems. However, how to correctly and accurately implement a robust algorithm to identify these parameters remains a challenge. Current methods are suffering from issues such as mode mix, noise contamination and parametric interference. M-AMD takes advantage of the repetitive applications of optimized AMDs to tackle the challenge of the identification of fast-varying stiffness and damping coefficient in nonlinear structures. It acts as the denoising filter, mode decomposition window and parameter separator, which simultaneously solve the existing issues with existing methods.

For damage detection and non-parametric identification, AWT and M-AMD are assumed to be able to identify and decompose each signal component from the measured dynamic responses of a structure. These components are mutually exclusive in frequency domain, including time-invariant and time-variant responses that are filtered with corresponding bisecting frequencies. Abnormality that is extracted especially from the time-varying bisecting frequencies for certain components can thus be identified from the amplified filtered results with high accuracy and high sensitivity to the causative perturbation.

1.6. DISSERTATION ORGANIZATION

This dissertation consists of seven sections. These sections are organized and briefly discussed as follows.

In Section 1, the concepts of structural health monitoring are introduced. The state-of-the-art development in signal processing techniques and two nondestructive evaluation approaches utilized in this dissertation (AE and IE) is reviewed. The objectives and significance of this study are presented.

In Section 2, the time-frequency resolution limitation in CWT is first reviewed. AWT is then defined as an average of short-time CWT segments that are staggered over time. Two algorithms are proposed to determine the optimal time-varying wavelet parameters from an arbitrary dynamic response with no prior knowledge. The characteristics and performance of the proposed AWT are then evaluated using an analytical signal of two closely-spaced frequency-modulated sinusoids and two delta functions over time. Synchro-squeezed adaptive wavelet transform (SSAWT) is then

proposed by integrating the synchro-squeezing technique to AWT, to achieve sharper and more accurate time-frequency results. Next, the characteristics and performance of the proposed SSAWT are evaluated using an analytical signal of two closely-spaced frequency-modulated sinusoids.

In Section 3, two seven-wire steel strands were axially loaded and unloaded in displacement control, each with the cross section of one wire reduced up to 90% in 10% increment and instrumented with one AE sensor at each end of the strand. AE parameters (hits, energy, and counts) were used to detect and locate two wire fracture cases. Pre-fracture signals were identified and differentiated from fracture signals, fracture-induced echo responses, and artificial tapping noises by analyzing them with AWT and comparing their features in time-frequency domain for the early detection of wire fracture in bridge cables.

In Section 4, the proposed AWT is applied into the impact echo responses experimentally recorded from a concrete slab, providing a more accurate and efficient way of delamination detection than the CWT. SSAWT is also applied to the IE responses experimentally recorded from a concrete slab to identify its thickness or detect embedded delamination defects. The identified results are compared with those by the conventional CWT, SSWT and the recently developed AWT, which gives more accurate identification results.

In Section 5, M-AMD are proposed and developed to identify the stiffness and damping coefficients of a weakly to moderately nonlinear systems from vibration responses. Based on free vibration, the efficiency and accuracy of the proposed M-AMD are evaluated with three characteristic nonlinear oscillators: Duffing, Bouc-Wen, and

spherical bearing models. Their dependence on the degree of nonlinearity is investigated with the Duffing system. Under forced vibration, the M-AMD is evaluated with the nonlinear Duffing oscillator under harmonic loads and a ¼-scale 3-story building model with frictional damping under seismic excitations.

In Section 6, the optimized AMD is developed for more robust and consistent signal decomposition with the AWT acting as the preprocessing technique. Numerical examples including the Duffing oscillator are used to demonstrate the proposed algorithm's feasibility to successfully decompose the nonlinear responses. The shake table test of a 1/20 scale cable-stayed bridge model was then performed for the identification of nonlinear behaviors.

In Section 7, the main findings and conclusions of this study are summarized and further researches are recommended.

2. ADAPTIVE WAVELET TRANSFORM

2.1. LIMITATION OF CWT

Due to non-selectivity in time-frequency resolution over time, the scalogram obtained from CWT is often distorted to certain degree. Specifically, the Heisenberg's uncertainty principle constrains the product of time and frequency resolutions equal to 2 rad. For the scaled wavelet in CWT, the following limitation is applicable to any type of mother wavelet. Without any loss of generality, a continuous complex Morlet wavelet is taken as an illustrative example. When the center frequency $\omega_c > 5$ rad/s, the simplified Morlet wavelet $\psi(t)$ as a function of time, t, can be approximated by:

$$\psi(t) = \frac{1}{\sqrt{\pi t_b}} e^{\frac{t^2}{t_b}} e^{i\omega_c t}, \tag{1}$$

and its Fourier transform, $\hat{\psi}(\omega)$, as a function of frequency, ω, is:

$$\hat{\psi}(\omega) = e^{-(2\pi)^2(\omega-\omega_c)^2}. \tag{2}$$

The resolution of the simplified mother wavelet in time and frequency domains can be obtained respectively from:

$$\Delta_\psi = \left[\frac{\int_{-\infty}^{+\infty}(t-t^*)^2|\psi(t)|^2 dt}{\int_{-\infty}^{+\infty}|\psi(t)|^2 dt}\right]^{\frac{1}{2}}, \tag{3}$$

$$\Delta_{\hat{\psi}} = \left[\frac{\int_0^{\infty}(\omega-\omega^*)^2|\hat{\psi}(\omega)|^2 d\omega}{\int_0^{\infty}|\hat{\psi}(\omega)|^2 d\omega}\right]^{\frac{1}{2}}. \tag{4}$$

where $i = \sqrt{-1}$ is an imaginary unit; t_b (= 2 s in this study) and ω_c in Equations (1) and (2) represent the time-domain bandwidth and the center frequency of the mother wavelet, respectively; Δ_ψ and $\Delta_{\hat{\psi}}$ are the radii of $\psi(t)$ and $\hat{\psi}(\omega)$, respectively; $t^* = 0$ and $\omega^* = \omega_c$, and $|.|$ denotes the modulus of a complex function. As shown in Figure 2.1, each rectangle represents how well two close peaks can be separated in various parts of the time-

frequency domain. The short and long sides of the rectangle symbolize high and low resolution, respectively. For the simplified Morlet wavelet, $\Delta_\psi = 1/\sqrt{2}$ s and $\Delta_{\hat{\psi}} = 1/\sqrt{2}$ rad/s are calculated. The product of time and frequency resolution corresponding to any rectangle is $(2a\Delta_\psi)(2\Delta_{\hat{\psi}}/a) = 2$ rad, a constraint on time and frequency resolution that is referred to as the Heisenberg's uncertainty principle. Here, $a \in [a_h, a_l]$ represents the scaling factor in CWT in which a_l and a_h correspond to low and high frequency components, respectively. The time and frequency resolution of the CWT with a fixed scaling factor remain unchanged over time, as illustrated in Figure 2.1. Note that b and b' represent the two values of shifting factor in the CWT.

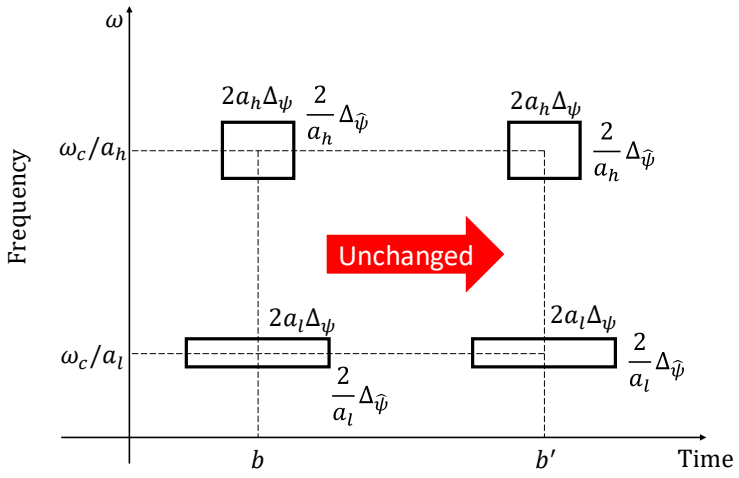

Figure 2.1. Time and frequency resolution of CWT

The frequency resolution, $\frac{2}{a}\Delta_{\hat{\psi}}$, as indicated in Figure 2.1, represents a minimum frequency difference of two signals that can be separated apart at the specified time and frequency. To illustrate this point, a cosine function of time with a single frequency component is taken as an example: $f(t) = cos(2\pi 2000t)$. After the function is discretized at a sampling rate of $F_s = 8000$ Hz, its wavelet transform with a fixed center frequency of

2 Hz is presented in Figure 2.2(a) in the form of scalogram. At the frequency of the signal, 2000 Hz, the scaling factor is $a = 8$. Thus, the thickness of a ridgeline of the scalogram or the frequency resolution of two such ridgelines is $F_s\Delta_{\hat{\psi}}/a = 8000/8\sqrt{2} = 707$. For two cosine functions with frequencies of 2000$\pm$353.5 Hz, the scalogram from their wavelet transform barely shows a separation of the two signals as indicated in Figure 2.2(b).

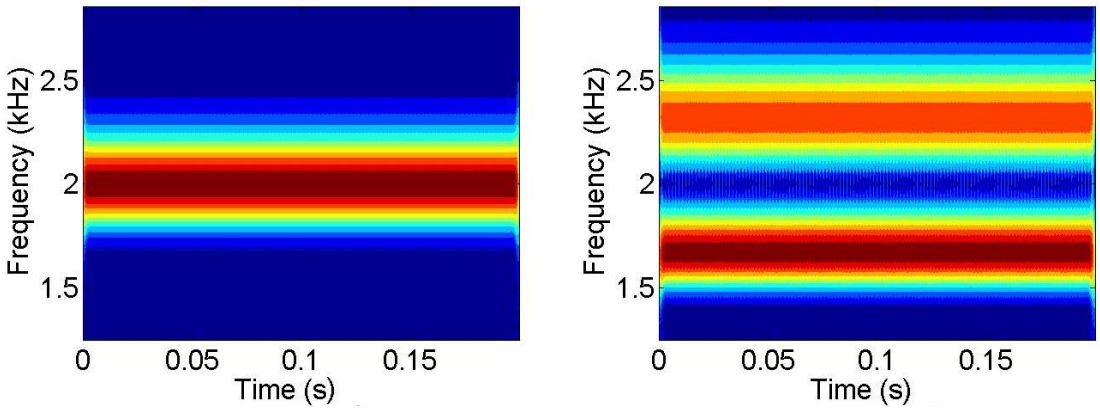

(a) One frequency component (b) Two frequency components

Figure 2.2. Scalograms from the wavelet analysis of cosine functions

2.2. ADAPTIVE WAVELET TRANSFORM ALGORITHM

To enable the selectivity of time and frequency resolution over time, time-varying center frequency and scaling factor are introduced in the Morlet wavelet so that a desirable time-frequency representation of a signal can be achieved in a time-frequency window of interest. This concept is realized in two steps.

2.2.1. Definition and Formulation. The first step is to introduce a short-time CWT or STCWT. Like the STFT, a rectangular window function $w_{\tau,T_\tau}(t)$ over $[\tau, \tau + T_\tau]$ is selected and a CWT is performed for the segment of an original signal $x(t)$ over $[\tau, \tau + T_\tau]$. Here, T_τ represents the window length at time τ. The STCWT can then be defined as:

$$STCWT(a,b;\ \tau,T_\tau) = \int_{-\infty}^{\infty} x(t) w_{\tau,T_\tau}(t)\, \overline{\psi_{a,b}(t)} dt. \quad (5)$$

where $\overline{\psi_{a,b}(t)}$ represents the complex conjugate of the wavelet function ψ with scaling and shifting factors of a and b, respectively. Due to low t_b (=2) of the simplified Morlet wavelet, the STCWT segment in Equation (5) is negligible unless the shifting factor b falls into the time window $[\tau+\Delta_\psi/2,\ \tau+T_\tau-\Delta_\psi/2]$. As a result, simply stitching STCWT segments together over non-overlapping time windows leads to a discontinuous and locally distorted time-frequency representation of the signal, similar to the recently published multi-bandwidth wavelet transform [79].

The second step is to remove the STCWT discontinuity at any transition time instants between two non-overlapping windows by staggering selected windows over time, as shown in Figure 2.3. At any time instant, all the STCWT segments overlapped in time are averaged based on the number of overlapped segments. Let a signal $x(t)$ of duration T start at time τ_0, end at time $\tau_0 + T$, and be sampled at time step Δt. Over the entire duration T of the signal, $n+1$ windows of length T_τ are introduced as illustrated in Figure 2.3 with starting times of τ_0, τ_1, …, τ_k, τ_{k+1}, …, and τ_n. Any two consecutive starting times, τ_k and τ_{k+1} ($k = 0, 1, \ldots, n-1$), are spaced by a sampling period Δt. In general, $\tau_n = \tau_0 + T - T_{\tau_n}$ and $\Delta t < T_{\tau_n} < T$.

Mathematically, the proposed AWT can be expressed into:

$$AWT(\omega,b) = \sum_{k=0}^{n} \frac{q_k}{p_k} STCWT\left[a(\tau_k), b; \tau_k, T_{\tau_k}\right]$$

$$= \sum_{k=0}^{n} \frac{q_k}{p_k} \int_{-\infty}^{\infty} x(t) w_{\tau_k,T_{\tau_k}}(t) \frac{1}{\sqrt{2\pi a(\tau_k)}} e^{-\frac{(t-b)^2}{2a^2(\tau_k)}} e^{\frac{-i\omega_c(\tau_k)(t-b)}{a(\tau_k)}} dt$$

$$= \sum_{k=0}^{n} \frac{q_k}{p_k} \frac{1}{\sqrt{2\pi\omega_c(\tau_k)/\omega}} \int_{\tau_k}^{\tau_k+T_{\tau_k}} x(t) e^{-\frac{(t-b)^2\omega^2}{2\omega_c^2(\tau_k)}} e^{-i\omega(t-b)}\, dt. \quad (6)$$

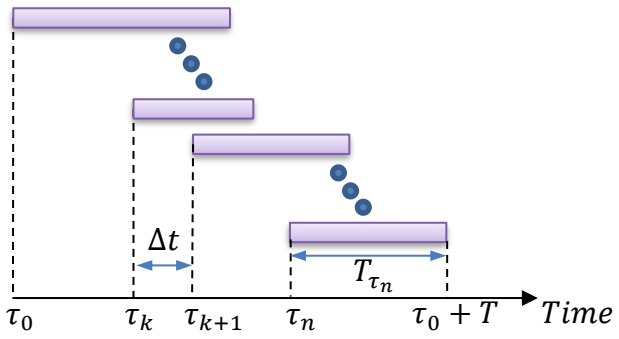

Figure 2.3. Windows overlapped in time

where $n = (T - T_{\tau_n})/\Delta t$, p_k represents the number of significant STCWT segments spanning each time ($1 \leq p_k \leq k$ at τ_k), q_k is an amplitude normalization factor to ensure that energy is appropriately distributed over time, and the center frequency $\omega_c(\tau_k)$ and the scaling factor $a(\tau_k)$ are constant within the k^{th} window length T_{τ_k} but change proportionally over time τ_k. For example, Equation (6) includes one significant STCWT segment at time τ_0, two segments at time τ_1, …, and $p_k = sum\{l_i | l_i = 1 \; for \; \tau_i + T_{\tau_i} \geq \tau_k, l_i = 0 \text{ otherwise}; i \in [1, k]\}$ segments up to time τ_k. In Equation (6), $\omega_c(\tau_k)/a(\tau_k) = \omega$, which is independent of time τ_k. By keeping the ratio between the center frequency and the scale factor unchanged over time, the phase of the proposed STCWT for various segments of a signal remains the same at each frequency of interest as that of the CWT. The amplitude of the STCWT, however, differs from that of the CWT due to the time-varying center frequency. To preserve energy over time, the energy of various segments is normalized to follow the distribution of the CWT. That is, the "root-mean-square" amplitude of the STCWT for the T_{τ_k} segment associated with $a(\tau_k)$ is normalized by the "root-mean-square" amplitude of the corresponding segment in the CWT of the overall signal. In other words, a normalization factor q_k is defined by:

$$q_k = \sqrt{\frac{\int_{\tau_k}^{\tau_k+T_{\tau_k}} \int_{a_h}^{a_l} |CWT(a,b)|^2 \, da db}{\int_{\tau_k}^{\tau_k+T_{\tau_k}} \int_{a_h}^{a_l} \left| STCWT\left[a(\tau_k), b; \tau_k, T_{\tau_k}\right]\right|^2 da(\tau_k) db}} \tag{7}$$

in which $|\cdot|$ represents the modulus of a complex transform function and $CWT(a,b) = \int_{-\infty}^{\infty} x(t)\,\overline{\psi_{a,b}(t)}dt$ denotes the CWT of the signal $x(t)$ with scaling and shifting factors of a and b, respectively. In Equation (7), the double integrations in the domain of a and b or $a(\tau_k)$ and b for each segment represent the total energy of the k^{th} segment of the CWT and STCWT in a frequency range of interest.

Unlike the STFT, AWT includes the information through two time parameters: shifting factor as used in the CWT and duration of the window function. The introduction of two time parameters allows a modification of time and frequency resolution over time for a desirable time-frequency representation of a signal as schematically illustrated in Figure 2.4. Like the CWT, the time and frequency resolution of the AWT can be changed at any time. Unlike the CWT, the scaling factor and the center frequency introduced in the AWT are time-dependent, resulting in selectable time and frequency resolution over time, as clearly indicated in Figure 2.4. Note that $\omega_c/a_l = \omega_c'/a_l'$ and $\omega_c/a_h = \omega_c'/a_h'$. Here, ω_c', a_l', and a_h' are proportional to ω_c, a_l, and a_h, respectively, at a different time as alluded in the following section.

2.2.2. Optimization of Time-varying Parameters. Figure 2.4 also shows the required frequency resolution of a signal at low and high frequencies, ω_{rl} and ω_{rh}, the required time resolution at low and high frequencies, t_{rl} and t_{rh}, and their corresponding scaling factors, a_l and a_h. At any time, the required frequency and time resolution are locally limited by the resolution of CWT. In terms of scaling factors, this limit yields

$$\frac{2\Delta_{\hat{\psi}}}{\omega_{rl}} < a_l < \frac{t_{rl}}{2\Delta_{\psi}} \text{ and } \frac{2\Delta_{\hat{\psi}}}{\omega_{rh}} < a_h < \frac{t_{rh}}{2\Delta_{\psi}}. \quad (8)$$

After the scaling factor bounds, a_l and a_h, are selected from Equation (8), the range of the scaling factor is equally divided with a step of Δa. At any particular scaling factor a_j, the frequency of interest ω_j can be related to the center frequency of the Morlet wavelet ω_{cj} by:

$$\omega_j = \frac{\omega_{cj}}{a_j} \quad (\omega_{rl} < \omega_j < \omega_{rh}, a_h < a_j < a_l). \quad (9)$$

As discussed previously, ω_{cj} is proportional to the scaling factor a_j to facilitate the averaging of STCWT segments. For example, when the center frequency is ω_c, the scaling factor ranges from a_l to a_h with a step size of Δa. When the center frequency is increased to $\lambda\omega_c$, the scaling factor ranges from λa_l to λa_h with a step size of $\lambda\Delta a$. Here, λ (≥1) is a positive number and $\omega_c = a_l\omega_{rl}$ represents the lowest center frequency selected.

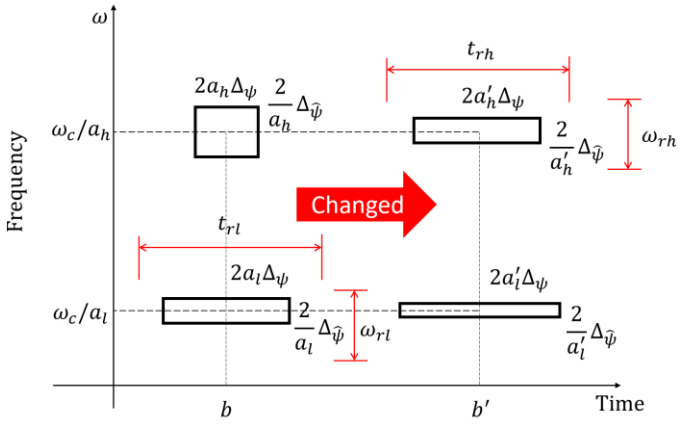

Figure 2.4. Required time and frequency resolution for a desirable time-frequency representation of a signal

For an unknown signal, the time-varying parameters in STCWT are determined following a flow chart of two optimization algorithms for time and frequency resolution

updating as summarized in Figure 2.5. First, the signal is analyzed with CWT with parameters (a, ω_c) that are based on the general signal characteristics. If the signal characteristics are unknown, ω_c is preferably set to 2π, which is close to the lower boundary for the simplified Morelet mother wavelet so that the best time resolution is guaranteed in the optimization procedure. At each time τ_k, an instantaneous frequency spectrum of the signal can be obtained from the CWT, giving a total of M dominant frequency bands at a predetermined threshold amplitude. When $M > 0$, each frequency bandwidth centered at frequency F_i $(i = 1,2, \dots, M)$ is referred to as the thickness (C_T^i) of a ridgeline of the spectrum at the threshold value. The corresponding scaling factor is represented by a_i. The time-dependent center frequency $F(\tau_k) = 0$ is initialized at time τ_k.

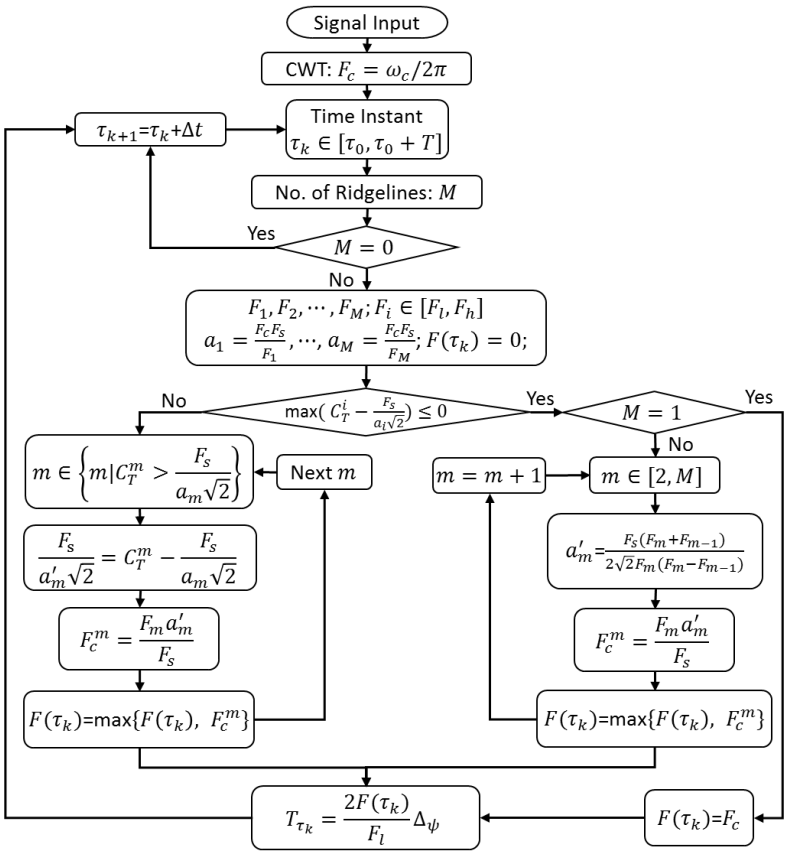

Figure 2.5. AWT algorithm for time-varying center frequency and window length

If all the ridgelines are relatively thin or $\max(C_T^i - F_s/a_i\sqrt{2}) \leq 0, i = 1,2,\dots,M$, $F(\tau_k) = F_c$ when $M = 1$ and $F(\tau_k) = \max\{F(\tau_k), F_c^m\}$ is determined recursively when $M \geq 2$. In the later case, the frequency resolution is reduced as much as possible so long as two individual ridgelines remain separable. In doing so, the corresponding time resolution is locally improved to its maximum. The new scaling factor a'_m and thus the new center frequency F_c^m are inversely proportional to the difference in two adjacent dominant frequencies ($F_m - F_{m-1}$), where $m = 2,3,\dots,M$.

When one or more of the ridgelines are relatively thick or $\max\{ C_T^i - F_s/a_i\sqrt{2}\} > 0, i = 1,2,\dots,M,$ all the thicker ridgelines are reduced to the required frequency resolution $F_s/a_m\sqrt{2}$ to enable the separation of potentially two frequency components that have been lumped into one ridgeline. In this case, the new scaling factor a'_m is determined from $\frac{F_s}{a'_m\sqrt{2}} = C_T^m - \frac{F_s}{a_m\sqrt{2}}$. Accordingly, the new center frequency F_c^m and the final time-dependent center frequency can be determined as above. To satisfy the required frequency resolution at all ridgelines, the final center frequency is selected as the maximum value of the candidate(s). That is, $F(\tau_k) = \max\{F(\tau_k), F_c^m\}$ recursively. The final scaling factor range is determined to ensure that the frequency range of interest remains unchanged. Correspondingly, the time-dependent window length can be determined from $T_{\tau_k} = \frac{2F(\tau_k)}{F_l}\Delta_\psi$. The above procedure is repeated until all the time instants in the range of interest have been considered.

In practical applications, the ridgeline thickness of a weak signal tends to disperse significantly. It is thus necessary to determine a triggering threshold of frequency bands, which corresponds to the required ridgeline thickness. The peak of an instantaneous

spectrum is first normalized to one as shown in Figure 2.6 in the case of a single frequency component signal. A threshold value is then determined when its horizontal line (green in Figure 2.6) intercepts the spectrum at two points (red dots in Figure 2.6) around the peak with a frequency spacing or bandwidth equal to the required ridgeline thickness calculated at the dominant frequency with given wavelet parameters.

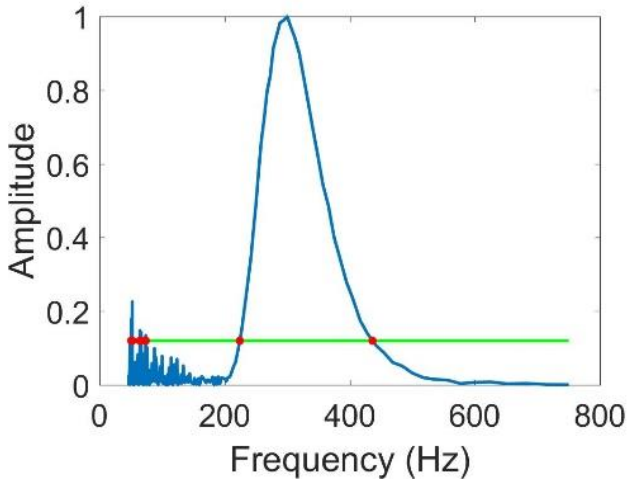

Figure 2.6. Threshold value determination

To understand the threshold sensitivity to the dominant frequency and sampling frequency of signals, a cosine function with its frequency ranging from 1 kHz to 4 kHz at 100 Hz increment was analyzed using the CWT with $F_c = 2$ Hz when the theoretical ridgeline frequency ranges from 353 Hz to 1414 Hz. Figure 2.7(a) shows the variation of the threshold value with the increasing frequency of the cosine function when sampled at $F_s = 10$ Hz. The threshold value fluctuates between 0.08 and 0.11 of the peak value. Similarly, for a cosine function with a frequency change of 100 Hz to 400 Hz, which was sampled at $F_s = 1$ kHz and analyzed with the CWT with $F_c = 1$ Hz, the threshold value fluctuates between 0.11 and 0.13 of the peak as shown in Figure 2.7(b).

The second study is to understand the influence of sampling frequency. For a cosine function with a frequency of 500 Hz and a wavelet transform with a center frequency of 1 Hz, the sampling rate was changed from 2 kHz to 5 kHz. As shown in Figure 2.8, the change of sampling frequency does not influence the threshold value significantly so long as the Shannon-Nyquist sampling theory is satisfied.

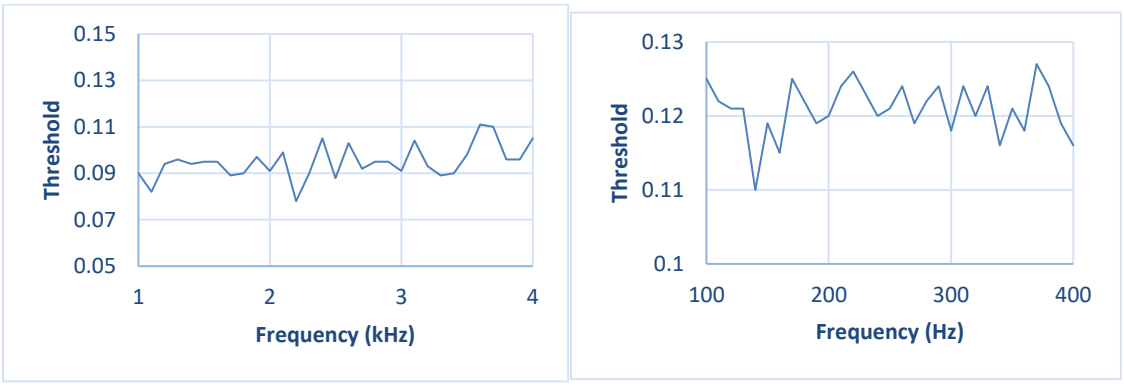

(a) $F_c = 2$ Hz, $F_s = 10$ kHz (b) $F_c = 1$ Hz, $F_s = 1000$ Hz

Figure 2.7. Threshold value variation with signal frequency changing

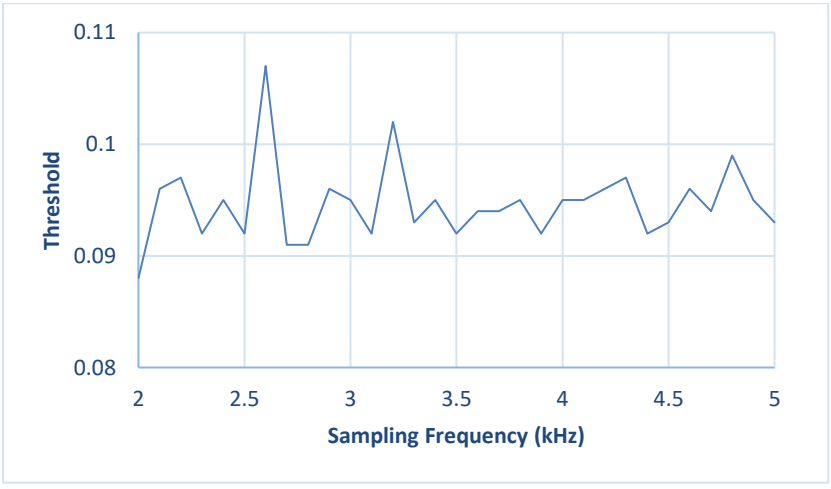

Figure 2.8. Threshold variation with sampling frequency increase

Based on the above parametric studies, the threshold value ranges from 8% to 13% of the peak value with any change in center frequency, signal frequency and sampling

frequency. This small fluctuation is likely associated with numerical errors introduced when the wavelet function is truncated in integration as shown in Equation (5). To guarantee reliable identification, the threshold is set to be 15% of the corresponding peak.

2.3. CHARACTERISTICS AND PERFORMANCE OF AWT

To better illustrate limitations with the CWT and the advantages with the proposed AWT, an analytical signal is considered. It is a combination of two closely-spaced frequency-modulated sinusoidal functions and two closely-spaced delta functions, which represents the most demanding signal on both time and frequency resolution. The example signal $x(t)$ can be mathematically expressed into:

$$x(t) = cos[2\pi 2000t + 100\, sin(2\pi 10t)]$$
$$+ cos[2\pi 2600t + 100\, sin(2\pi 10t)] + K[\delta(t - 0.145) + \delta(t - 0.15)] \quad (10)$$

in which $K = 10$ is a gain factor, representing the relative significance on the delta and sinusoidal functions. The signal is sampled at 10 kHz in data analysis or $\Delta t = 10^{-4}$ s. Its theoretical scalogram in time-frequency domain is presented in Figure 2.9.

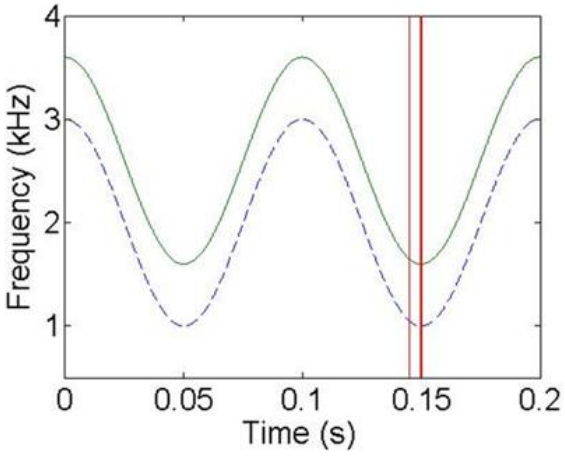

Figure 2.9. Theoretical scalogram of the combined sinusoidal and delta signal

The signal was analyzed with CWT ($F_c = 2$ Hz). The obtained scalogram is shown in Figure 2.10. It can be seen form Fig. 10 that the lowest and worst frequency resolution is achieved at time instants 0, 0.1 and 0.2 s, while the highest and best frequency resolution is at 0.05 and 0.15 s. The algorithm as described in Figure 2.5 is thus applied to improve the frequency and time resolution in the range as shown in Figure 2.10.

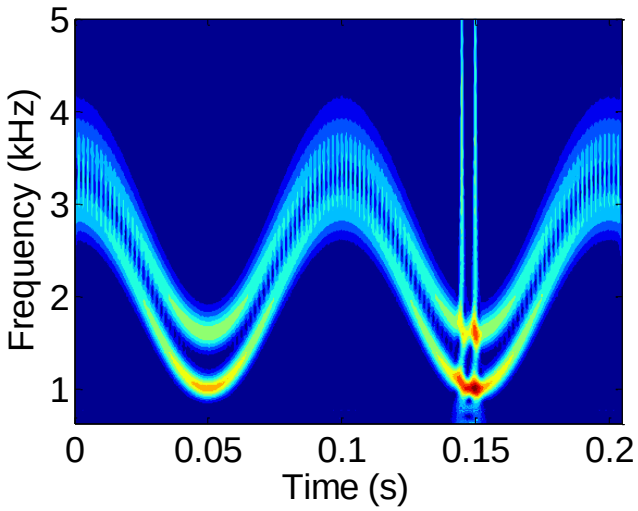

Figure 2.10. CWT representation of the signal

At time 0 s, the two frequency components are actually mixed together with a frequency range of 2590 Hz to 4170 Hz, resulting in a frequency bandwidth or ridgeline thickness of 1580 Hz, centered at 3380 Hz as shown in Figure 2.11(a). In this case, the scaling factor is $a_1 = \frac{F_c F_s}{F_1} = 2 \times \frac{10000}{3380} = 5.92$ and the ridgeline thickness of a single frequency component is $\frac{F_s \Delta_{\hat{\psi}}}{a_1} = \frac{F_1 \Delta_{\hat{\psi}}}{F_c} = \frac{3380}{2\sqrt{2}} = 1195$ Hz. Since the actual ridgeline thickness exceeds the thickness of single component, the scaling factor must be updated as $a_1' = \frac{F_s}{(1580 - \frac{F_s \Delta_{\hat{\psi}}}{a_1})\sqrt{2}} = 18.37$. The center frequency can thus be updated as $F_c = \frac{F_1 a_1'}{F_s} =$

$\frac{3380\times18.37}{10000} = 6.2$ Hz, which is larger than 0. Therefore, $F(0) = 6.2$ Hz. The final step is to determine the window length, $T_0 = \frac{2F(0)}{F_l}\Delta_\psi = \frac{2\times6.2}{1000\sqrt{2}} = 0.0088$ s, where $F_l = 1000$ Hz.

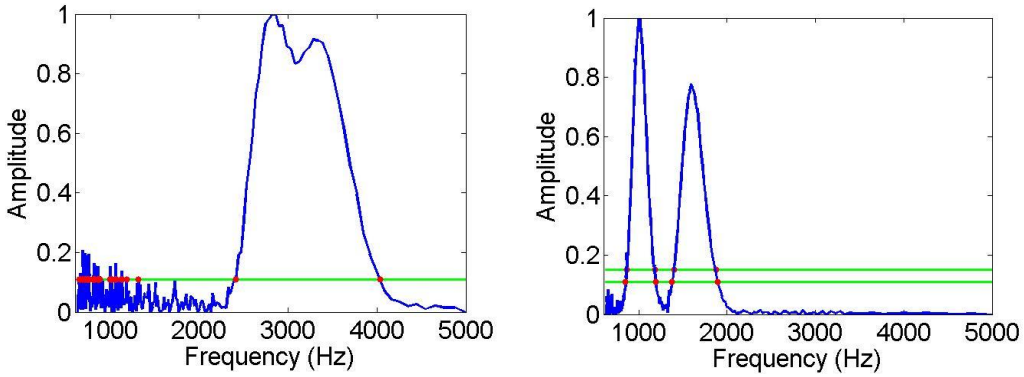

(a) 0 s (b) 0.05 s

Figure 2.11. Two instantaneous spectra without the effect of delta functions

At time 0.05 s, the instantaneous spectrum as presented in Figure 2.11(b) indicates a clear separation of two frequency components with a ridgeline thickness of 350 Hz and 550 Hz at peak frequencies of 1,000 and 1,600 Hz, respectively. The calculated scaling factors at the two peak frequencies are 20 and 12.5, and their corresponding ridgeline thicknesses are 354 Hz and 566 Hz, respectively. Since both identified ridgeline thicknesses are smaller than the calculated, the two frequency components are well separable in frequency domain. In this case, the time resolution can be improved with a new scaling factor at the second peak: $a_2' = \frac{F_s(F_2+F_1)}{2\sqrt{2}F_2(F_2-F_1)} = \frac{10000(1600+1000)}{2\sqrt{2}\times1600(1600-1000)} = 9.58$, which is less than the original scaling factors at the two peaks. The center frequency at this time is then calculated as $F(0.5) = F_c = \frac{F_2 a_2'}{F_s} = \frac{1600\times9.58}{10000} = 1.53$ Hz, and the window length is updated to $T_{0.5} = \frac{2F(0.5)}{F_l}\Delta_\psi = \frac{2\times1.53}{1000\sqrt{2}} = 0.0022$ s.

In addition to the above two extreme cases for the cosine functions, two special conditions must be discussed: energy leakage and delta functions. It can be seen from Figure 2.11 that energy leakage due to signal discretization and integration truncation is present at a frequency range of 500 Hz - 1000 Hz. The low-frequency peaks can be directly filtered out when their amplitudes are below 10%. Otherwise, they can be separated from other signal peaks by verifying that the frequency bandwidth of each peak at 5% remains significantly less than the theoretical thickness calculated from $F_s/a\sqrt{2}$. It can be seen from Figure 2.9 that the two delta functions occur at 0.145 s and 0.15 s. Figure 2.12 shows the instantaneous spectrum at 0.15 s when energy is distributed over a broadband of frequency with local concentrations at the frequencies of cosine functions. In this case, the signal threshold must be determined to be above the stationary component by identifying the baseline of the frequency distribution as indicated in Figure 2.12.

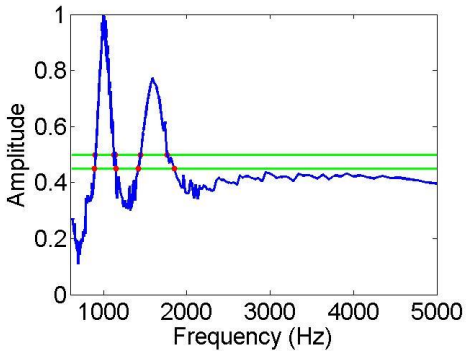

Figure 2.12. The instantaneous spectrum at 0.15 s with the effect of delta functions

Once the instantaneous spectra at all times have been analyzed by following the procedure given in Figure 2.5, the time-varying center frequency of the AWT can be determined and presented in Figure 2.13(a) as a function of time that is defined by the beginning of each window. The time-varying window length is proportional to the center

frequency as indicated in Figure 2.5. The variation of q_k over time is presented in Figure 2.13(b), which ensures that the energy distribution in the time and frequency plane is consistent with that of the CWT. It can be observed from Figure 2.13(b) that the normalization factor significantly fluctuates around the two delta functions due to their locally added energy. Using the obtained center frequency and window length, the AWT of the signal in Equation (10) results in the scalogram as shown in Figure 2.13(c). The AWT reveals a smooth transition at time instances of the discretized signal and exhibits higher resolution than the CWT as shown in Figure 2.10 in the high frequency range where improved frequency resolutions are used. Figure 2.13(c) is a high fidelity representation of Figure 2.9 in the time-frequency domain of interest.

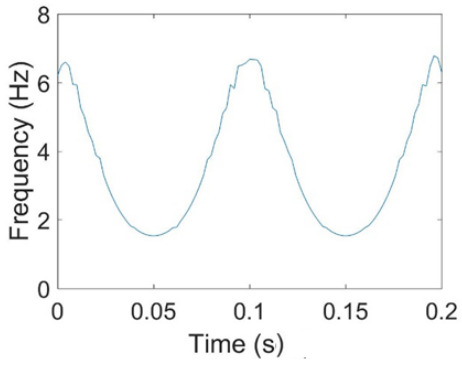

(a) Time-varying center frequency

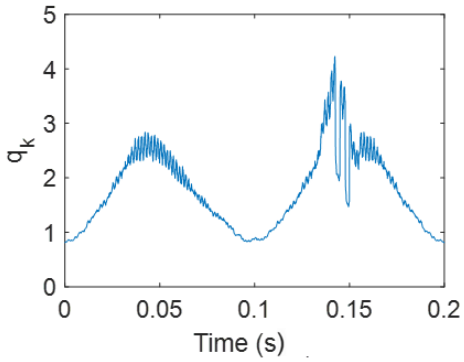

(b) Time-varying normalization factor

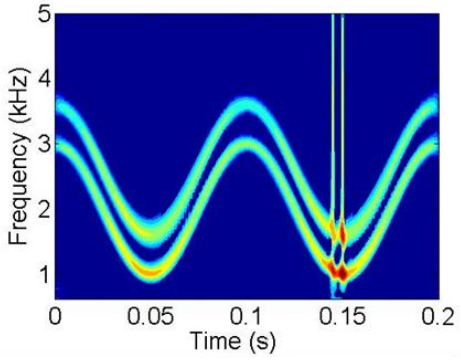

(c) Scalogram of the signal by AWT

Figure 2.13. Characteristic AWT parameters and results

To demonstrate the advantages of AWT over STCWT, the signal represented by Equation (10) was divided into 9 segments, each assigned an optimized center frequency of the Morlet mother wavelet. The STCWT scalogram of the signal is presented in Figure 2.14 by stitching together those of the non-overlapping segments. It can be clearly observed from Figure 2.14 that the overall scalogram is discontinuous and not smooth, leaving behind the stitching traces or sudden frequency jumps at transition times between the center frequencies due to end effects. Although direct, simply stitching the STCWTs would thus be unsatisfactory.

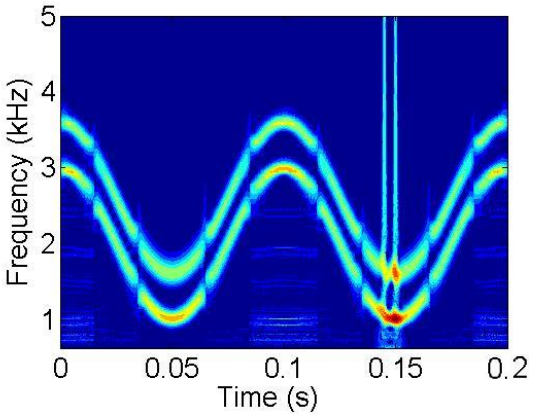

Figure 2.14. The STCWT scalogram by segmental stitching

To quantify the dispersion of ridgelines in scalogram, each instantaneous spectrum (wavelet coefficient) as shown in Figures 2.10 and 2.13(c) at any time, excluding the two delta functions for simplicity, was normalized by its total area and then treated as a probability density function so that the standard deviation of the spectral distribution over frequency can be evaluated. For comparison, two theoretic frequency curves as shown in Figure 2.9 excluding the delta functions were considered as two zero-thickness ridgelines in a spectrum of two pulses. The standard deviation of the theoretic spectrum can be

determined to be 300 Hz. Figure 2.15 shows the standard deviation (Std. Dev.) of spectral distributions as a function of time with the solid (blue) and dotted (red) lines representing the CWT and AWT, respectively. Figure 2.15 also includes a constant deviation of the two theoretic frequency lines in dashed line (green).

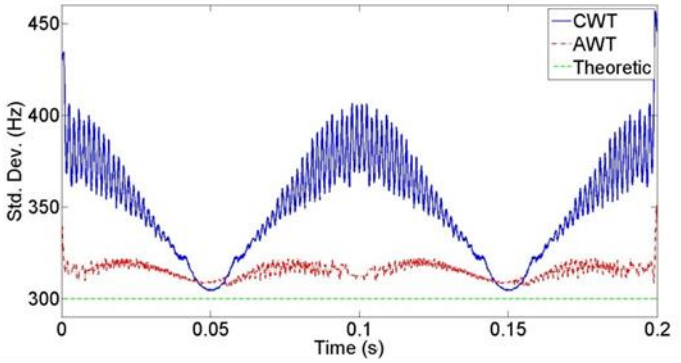

Figure 2.15. Standard deviations of CWT and AWT over time and its comparison with theoretic value

It can be seen from Figure 2.15 that the deviation of AWT is less fluctuating and smoother than that of CWT. This is because the frequency resolution has been improved by the AWT in most part of the time-frequency domain. At 0.05 s and 0.15 s, the deviation of CWT, 305 Hz, is slightly smaller than that of AWT, 309 Hz since the frequency resolution in the AWT was locally sacrificed for improved time resolution as discussed in the previous section, both exceeding the theoretic value, 300 Hz. At 0, 0.1, and 0.2 s, where CWT has the lowest frequency resolution, the deviation of CWT spectra reaches a maximum of 406 Hz in comparison with 315 Hz for the proposed AWT or approximately 22% reduction from the deviation of CWT. The variation range of the AWT, 309 Hz to 322 Hz, is only 4.3% of its lowest deviation while the range of the CWT, 305 Hz to 406 Hz, is 33.1% of its lowest deviation. The reduction in variation will significantly improve

the detectability of delamination as demonstrated in the following application example. Note that the end effect was not taken into account during the comparison.

2.4. SYNCHRO-SQUEEZED ADAPTIVE WAVELET TRANSFORM

Synchro-squeezing is a special case of reallocation methods. When integrated into the reversible SSWT, it can help sharpen the scalogram/ridgelines obtained from the CWT [78]. Before SSAWT is developed, the SSWT is briefly reviewed. The CWT represents the convolution of a signal, $x(t)$, and the conjugate of an appropriately chosen scaled mother wavelet, ψ:

$$W_x(a,b) = \frac{1}{\sqrt{a}} \int_{-\infty}^{\infty} x(t)\overline{\psi_{a,b}(t)}dt, \tag{11}$$

where $W_x(a,b)$ is the wavelet coefficient as illustrated in Figure 2.16(a) (module of the wavelet coefficient if it is a complex function) when $x(t) = cos(2\pi 8t)$. It represents how similar the signal is to the mother wavelet when shifted by a certain time b and scaled by a factor of a. The wavelet coefficient is synchro-squeezed and transferred from the time-scale plane to a time-frequency plane by:

$$SSWT\{x(t)\}(\omega,b) = \int_{A(b)} W_x(a,b)a^{-3/2}\delta(\omega_x(a,b) - \omega)da, \tag{12}$$

where $A(b) = \{a: W_x(a,b) \neq 0\}$, and $\omega_x(a,b) = -i\frac{1}{W_x(a,b)}\frac{\partial[W_x(a,b)]}{\partial b}$. The synchro-squeezed transform corresponding to Figure 2.16(a) is presented in Figure 2.16(b) (coefficient module). It is clearly seen from Figure 2.16(b) that the frequency of the signal is 8 Hz.

The AWT is based on the conventional CWT, both having line dispersions in each scalogram. This dispersive representation leads to inaccurate, distorted or even smeared results that often hinder readability. To overcome the shortfalls of AWT and SSWT, a

synchro-squeezing step is integrated into the AWT to develop a new method called SSAWT. According to Equations (6) and (12), SSAWT is defined as:

$$SSAWT\{x(t)\}(\omega, b) = \int_{A(b)} AWT\{x(t)\}(a, b)a^{-3/2}\delta(\omega_x(a, b) - \omega)da \quad (13)$$

SSAWT can yield a more accurate time-frequency representation without dispersion and adaptively vary the center frequency and bandwidth over time to optimize the signal representation at each time instant.

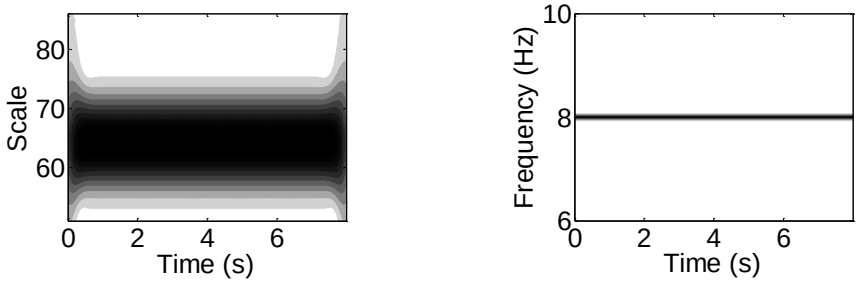

(a) CWT (b) SSWT

Figure 2.16. SSWT illustration of $x(t) = cos(2\pi 8t)$

2.5. EFFECTIVENESS OF SSAWT

To test the effectiveness of SSAWT to its full extent, a special signal is designed as expressed into Equation (14) to cover changing frequency combinations over time. It includes four time segments of 0.1 s each: two closely-spaced frequency-modulated sinusoidal functions, two closely-spaced high frequencies and a low frequency, two closely-spaced low frequencies and a high frequency, and one frequency. The signal function is sampled at 10 kHz and expressed into:

$$x(t) = \begin{cases} \cos(2\pi 2000t + 100\sin(2\pi 10t)) + \cos(2\pi 2500t + 100\sin(2\pi 10t)) & 0 \text{ s} < t \leq 0.1 \text{ s} \\ \cos(2\pi 3000t) + \cos(2\pi 3500t) + \cos(2\pi 1250t) & 0.1 \text{ s} < t \leq 0.2 \text{ s} \\ \cos(2\pi 1000t) + \cos(2\pi 1500t) + \cos(2\pi 3250t) & 0.2 \text{ s} < t \leq 0.3 \text{ s} \\ \cos(2\pi 2000t) & 0.3 \text{ s} < t \leq 0.4 \text{ s} \end{cases} \quad (14)$$

Figure 2.17(a) shows the module of the CWT coefficient referred to as scalogram of the signal. The top portion of the scalogram smears due to low frequency resolution. Such an issue could be resolved by simply increasing the center frequency of the mother wavelet if the signal had constant frequency components only. When the signal contains time-varying frequency components prior to 0.1 s as shown in Equation (14), the increase in center frequency can reduce time resolution, which could make two closed-spaced ridgelines difficult to resolve as well. On the other hand, the SSAWT of the signal as presented in Figure 2.17(b) shows thinner and separable ridgelines with a significantly improved identification accuracy. In fact, the identified ridgelines from the SSAWT coincide with the theoretic lines.

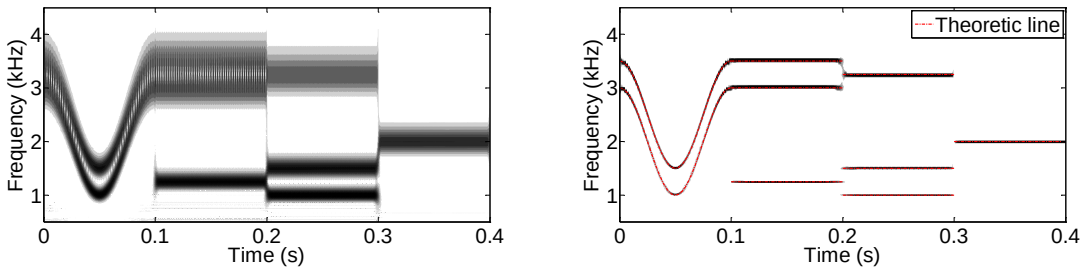

(a) CWT ($F_c = 1$ Hz) (b) SSAWT

Figure 2.17. Time-frequency representation of the numerical signal

The proposed SSAWT was performed by following the flow diagram in Figure 2.5 with the lowest frequency of interest $F_l = 500$ Hz and then by synchro-squeezing the ridgelines in scalogram. Based on the CWT given in Figure 2.17(a), several time instants were considered to illustrate how the proposed optimization algorithm works under different conditions. At 0.01 s as shown in Figure 2.18(a), two frequency components are mixed together and centered at 3,140 Hz between the two red dots (2,430 Hz and 3,850 Hz)

where the 15% threshold line crosses the ridgeline. In theory, the thickness of a ridgeline at 3,140 Hz is $F_1/(\sqrt{2}F_c)$ =3140/2$\sqrt{2}$=1110 Hz, which is smaller than the identified thickness (1,420 Hz). This comparison indicates that more than one components are included in the frequency range. The center frequency at this time is thus updated to $F(0.01) = F_1/(\sqrt{2}C_T^1 - F_1/F_c)$=3140/(1420$\sqrt{2}$-3140/2)=7.2 Hz.

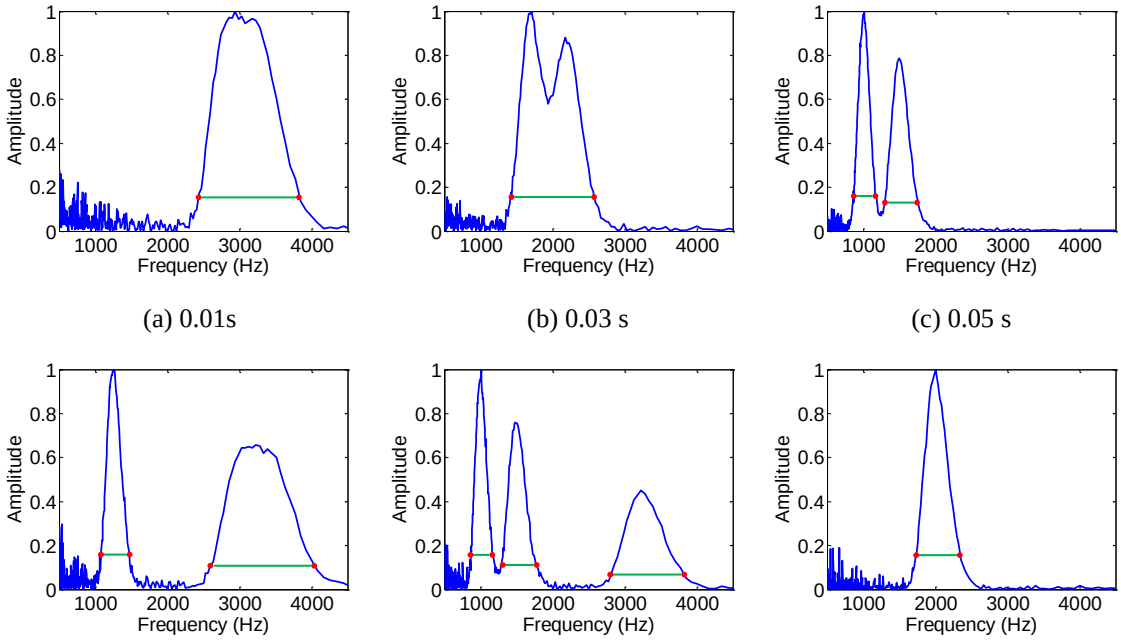

(a) 0.01s (b) 0.03 s (c) 0.05 s

(d) 0.15 s (e) 0.25 s (f) 0.35 s

Figure 2.18. Instantaneous frequency spectra at various time instants

The two peaks appear at 0.02 s as shown in Figure 2.18(b) and are completely separated at 0.05 s as shown in Figure 2.18(c). In the latter case, the low frequency component spans from 865 Hz to 1,180 Hz (centered at 1,022 Hz) and the high component is from 1,290 Hz to 1,770 Hz (centered at 1,530 Hz). They correspond to the required ridgeline thicknesses of $F_1/(\sqrt{2}F_c)$ =1022/2$\sqrt{2}$=361 Hz (>315 Hz=1180-865 Hz) and $F_2/(\sqrt{2}F_c)$= 1530/2$\sqrt{2}$=541 Hz (>480 Hz=1770-1290 Hz), respectively. Therefore, time

resolution can be improved at 0.05 s by using an updated center frequency of $F(0.05) = (F_2 + F_1)/(F_2 - F_1)/2\sqrt{2} = (1530 + 1022)/(1530 - 1022)/2\sqrt{2} = 1.8$ Hz. The trend in spectral change between 0.05 s and 0.1 s is generally a mirror image of that between 0.05 s and 0 s.

At 0.15 s, two peaks are also observed as shown in Figure 2.18(d). The low frequency peak corresponds to a single frequency component while the high frequency peak actually contains two frequency components. The latter peak controls the updated center frequency as $F(0.1 - 0.2)$=$3320/(1470\sqrt{2} - 3320/2) = 8.0$ Hz. At 0.25 s and 0.35 s, each peak represents one frequency component. At 0.25 s, the center frequency is updated to $F(0.2 - 0.3) = 1.8$ Hz similar to Figure 2.18(c) with multiple components. At 0.35 s, the center frequency remains unchanged since there is one peak only. The automatically optimized center frequency and its corresponding window length over time are presented in Figure 2.19.

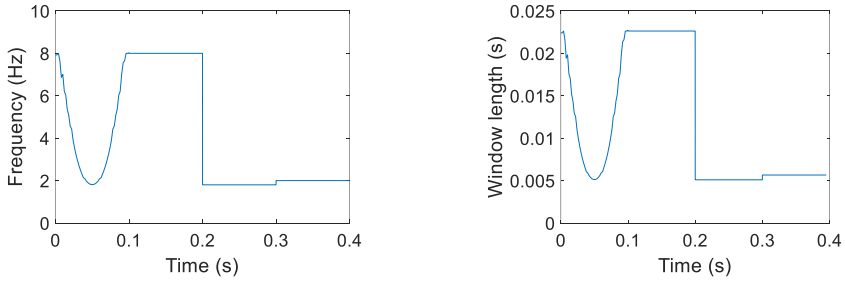

(a) Center frequency (b) Window length

Figure 2.19. Optimized time-varying STCWT parameters

The resulted SSAWT in Figure 2.17(b) are compared with the AWT and SSWT (with three center frequencies) of the signal as shown in Figure 2.20. The synchro-squeezing in SSAWT significantly reduces the ridgeline dispersion in AWT as observed

in Figure 2.20(a). Although the AWT results in a better time-frequency representation than the CWT, a sudden change in resolution occurs between 0.2 s and 0.3 s due to the time lag induced by a time-varying window function of STCWT.

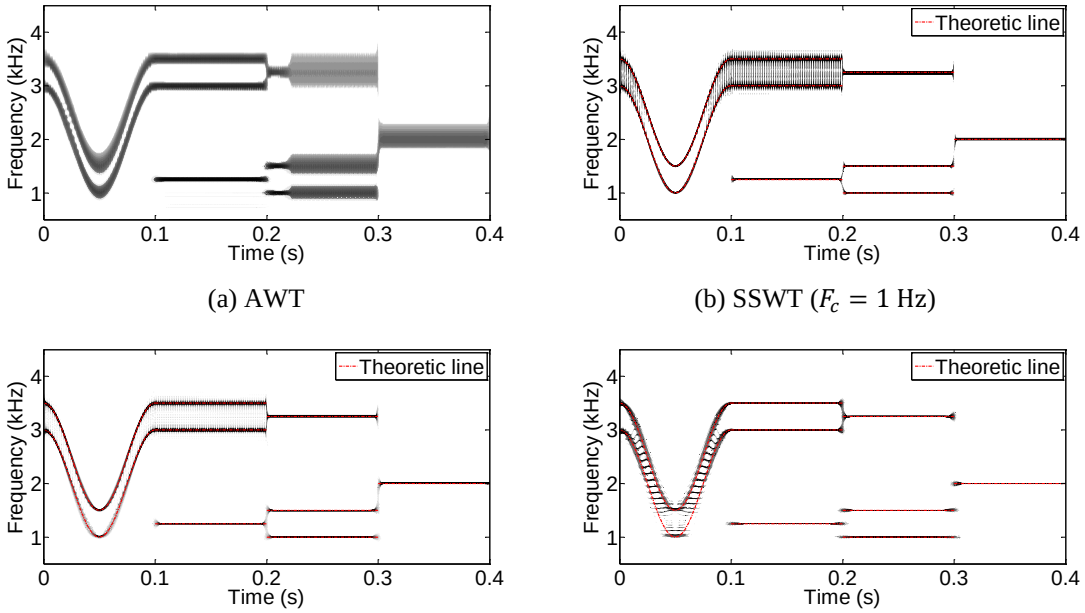

(a) AWT (b) SSWT ($F_c = 1$ Hz)

(c) SSWT ($F_c = 3$ Hz) (d) SSWT ($F_c = 6$ Hz)

Figure 2.20. AWT and SSWT with various center frequencies

To compare with the proposed SSAWT in Figure 2.17(b), the SSWT is taken with three different center frequencies as shown in Figure 2.20(b-d). For $F_c = 1$ Hz, two high frequency components significantly fluctuate from 0.08 s to 0.2 s and cannot be separated completely. As the center frequency increases from 1 Hz to 6 Hz, the low frequency components are truncated partially due to poor time resolution as shown in Figure 2.20(d). When the low and high frequency components are balanced with $F_c = 3$ Hz in SSWT as shown in Figure 2.20(c), the two extreme ends are still not well represented in the time-frequency domain. In general, the drawback of SSWT is similar to CWT, which a fixed variation of resolution is present for every time instant.

To quantify the accuracy in identifying the ridgelines in scalogram, the overall error between the identified ridgelines, $S(f,t)$, and the theoretic values, $S_T(f,t)$, in the time (t) - frequency (f) domain of interest is determined by:

$$Error = \sqrt{\frac{\iint [S^2(f,t) - S_T^2(f,t)]dfdt}{\iint S_T^2(f,t)dfdt}} \times 100\% \quad (15)$$

The calculated error of SSAWT is 1.1%, which is mainly caused by the transition region between adjacent time segments. The errors of SSWT with a center frequency of 1 Hz, 3 Hz and 6 Hz are 8.3%, 5.7% and 6.2%, respectively. Thus, the proposed SSAWT is at least 5 times more accurate than the SSWT in this example.

2.6. SUMMARY

In this section, an adaptive wavelet transform with optimized time-varying resolution in a time-frequency domain of interest has been defined for a desirable time-frequency representation of signals. A robust flowchart of two optimization algorithms for time and frequency resolution updating has been developed to identify center frequencies, scaling factors, and window lengths over time. Synchro-squeezing technique is then introduced to formulate the SSAWT, which has been proposed for an accurate time-frequency representation of signals.

For the example signal with two closely-spaced sinusoidal functions, the instantaneous spectra (wavelet coefficients) over frequency from AWT have a dispersion range of 309 Hz to 322 Hz by the proposed wavelet transform, which is only 4.3% of its lowest deviation, in contrast to a range of 305 Hz to 406 Hz or 33.1% of the lowest deviation of conventional wavelet transform. The discernibility for frequency features over time has been improved for approximately 7.7 times.

SSAWT resulted in 1.1% error in time-frequency representation of an illustrative signal with four time segments covering various frequency distributions, which is at least 5 times more accurate than the conventional SSWT. The synchro-squeezing process made the recently developed AWT capable of distinguishing ridgelines in scalogram and thus detecting defects in engineering applications more accurately.

3. EARLY DETECTION OF WIRE FRACTURE IN 7-WIRE STRANDS THROUGH ADAPTIVE WAVELET TRANSFORM OF ACOUSTIC SIGNALS

3.1. TEST SETUP OF SEVEN-WIRE STRANDS

Ronald Wilson Reagan Memorial Bridge was open to traffic on February 9, 2014. As part of the four-lane I-70 highway improvement project, the bridge spanning across the Mississippi River connects St. Louis, MO, to East St. Louis, IL. It is a two-tower cable-stayed structure with a total length of 2,803 ft (854 m), including a main span of 1,500 ft (457 m). The bridge is a critical infrastructure near downtown, St. Louis, MO. Therefore, developing a non-destructive evaluation technique for the early detection of potential wire fracture in steel strands is critically important to ensure safety of the public.

The stay cables of the I-70 Mississippi River Bridge consist of a number of steel strands, each with seven twisted high strength wires. In this study, two 21-foot-long (6.4 m) strands that were from the bridge construction were tested under axial loading with one outer wire notched at center and near support, respectively, to simulate a damage-induced reduction of cross section area. Their properties and manufacture specifications are included in Table 3.1. Each twist completes over a distance of 7.5 in (19.05 cm), which is referred to as the cable lay length in engineering practice.

Table 3.1. Specifications and properties of a high strength steel strand (270 ksi)

Strand Parameter	Value
Nominal diameter	0.6 in. (1.52 cm)
Minimum breaking strength	58,600 lbf (260.7 kN)
Nominal modulus of elasticity	28.5×106 psi (196.5×103 MPa)
Nominal cross sectional area	0.217 in2 (1.4 cm^2)
Nominal weight	740 lbs/1,000 ft (110 kg/100 m)

Figure 3.1(a) shows the overall test setup of a strand of seven twisted wires under axial loading. At each end of the strand, a composite beam (red) of two back-to-back channels with a gap in between was side laid down next to two anchorage holes on the strong floor. Additional two double-channel beams (black) were spanned in right angle over the two ends of the red beam, and anchored to the strong floor with four Dywidag rods. To prevent the red beam from moving and rotating during tests, each Dywidag rod was post-tensioned to 60 kips (266.9 kN), which is significantly less than the 100 kips (444.8 kN) load capacity that each hole on the strong floor can take. Once the anchorage support is in place, as shown in Figure 3.1(b), a strand was passed through the gap between two channels of the red beam, a load-distribution steel platen, a hydraulic jack, another steel platen, and a three-piece anchor wedge. At the other end of the strand, as shown in Figure 3.1(c), the anchorage support is identical to Figure 3.1(b) except that the hydraulic jack was replaced by a load cell. The test setup was completed by covering the strand with a longitudinally slotted, transparent, plastic tube, as shown in Figure 3.1(a), to address a safety concern of the potential sudden release of a broken steel wire during tests. Other than the load cell as shown in Figure 3.1(b), two linear variable differential tranformers (LVDTs) as shown in Figure 3.1(b, c) were installed at two ends of the test strand to measure axial displacements. In addition, one narrowband AE sensor (Model R1.5I) with a resonant frequency of 14 kHz and another wideband AE sensor (Model F15I-AST) with a nearly constant frequency response between 100 kHz and 400 kHz were deployed at each end of the test strand for comparison. As shown in Figure 3.1(c), the two AE sensors were attached in orthognal directions with silicon compound on the surface of the three-piece anchor wedge.

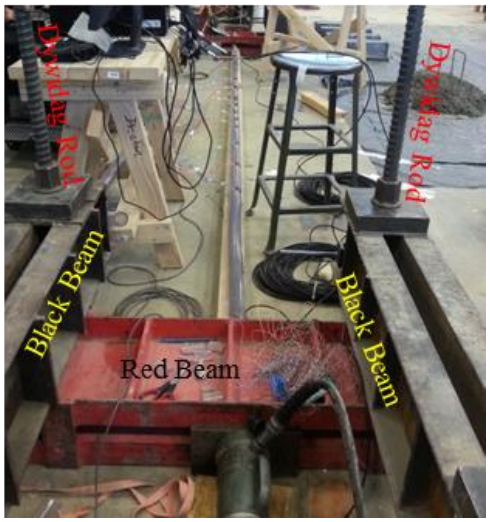

(a) Strand placement

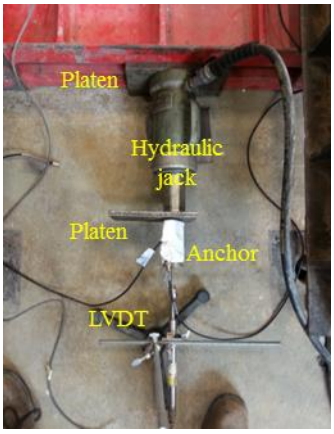

(b) Anchorage detail (hydraulic jack)

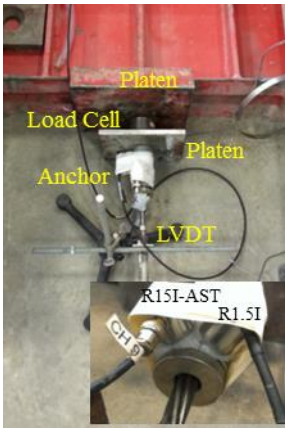

(c) Anchorage detail (load cell)

Figure 3.1. Test setup of a seven-wire strand

AE signals were recorded from a 32-channel Micro-II system while the load and displacement data were recorded through a 128-channel acquisition system at a sample rate of 500 kHz. The time window length was set to 8 ms to ensure that the dominant features of pre-fracture, fracture, and fracture-induced echo signals can be captured properly. Each intact strand of seven wires was first loaded and unloaded for three times up to a tension force of 20 kips (89.0 kN), corresponding to 34% of the minimum breaking strength of the strand. Then, one outer wire was cut off by 10% of the cross section area, and the strand was loaded to 20 kips (89.0 kN) and unloaded. Next, the cross section of the cut wire was

further reduced by 10%, and the strand was loaded to 20 kips and unloaded again. This test process repeated up to 80% of the area reduction with 10% increment, as shown in Figure 3.2. Finally, with 90% of the cross section area reduced, the strand was tested to failure. The cut locations of the two strands (600 cm clear span length) are 300 cm and 550 cm from their left supports, respectively.

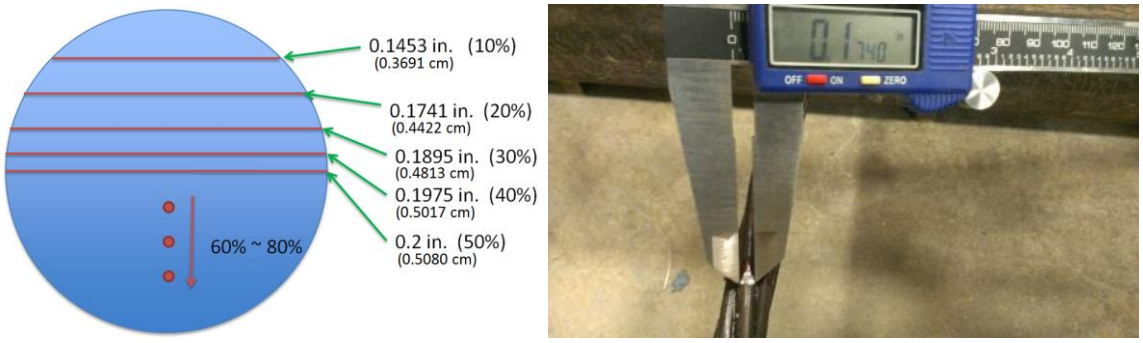

Figure 3.2. Cross section reduction of the partially cut wire

Axial loads were applied up to 20 kips (89.0 kN) in about 3 min. and manually controlled by monitoring the force reading from the load cell installed at one end of the test strand. In addition to external loading, four types of artificial noises were generated by dropping four different types of foreign objects on the test strand at the height of 1 ft (0.3 m). The four objects were a steel bar, a marker, a steel washer, and a penny as shown in Figure 3.3.

Figure 3.3. Four objects tapped on the test strand to create different acoustic noises

3.2. DETECTION AND LOCALIZATION OF WIRE FRACTURE

The data taken from the LVDTs indicated that there was no sudden change in displacement at each end of the test strand and no slip at the two anchorage supports throughout the tests except the moment of fracturing. When the outer wire fractured, the bearing and frictional forces among wires were suddenly changed. Therefore, the reaction force by the strong floor was changed, resulting in a sudden alternation of displacement.

3.2.1. AE Parameter Change during Wire Fracture. An acoustic event is the occurrence of a phenomenon when elastic energy is released into a material and propagates through it in the form of elastic wave. As presented in Figure 3.4, a representative acoustic signal can be characterized by hit, energy, and count.

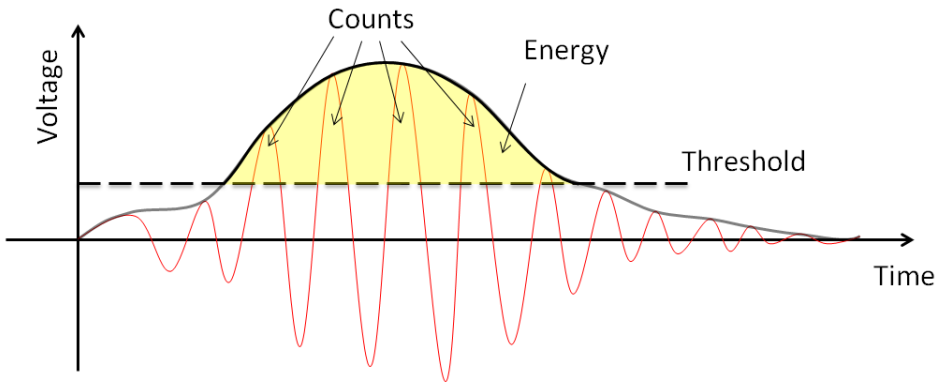

Figure 3.4. Parameters of a typical AE signal from a single hit

A hit is used to describe a single waveform recorded by one sensor (e.g., Figure 3.4), so that multiple hits can be acquired by a suite of distributed AE sensors during a single event. The energy is defined as the area between envelope of the waveform and a threshold value (shaded area in Figure 3.4). Each upcrossing of the waveform at the threshold represents one count. Unless noted otherwise, the threshold value in this study

was set to 30 dB based on two tests. First, the pencil-lead test yielded 38 dB, which are close to 40 dB identified by other researchers [9, 12, 13]. Second, 30 dB was sufficient to filter out environmental noises during the loading process of an intact strand. However, as indicated later, further test results indicate that a threshold of 60 dB can be used without losing any captured acoustic events. A series of pencil-lead tests at multiple locations 1 m apart also determined a wave velocity of 197,000 in/s (5010 m/s) in the first cable specimen.

When the reduced cross section area of the cut wire was up to 80%, the recorded AE signals changed little, indicating no acoustic event. When the cross section area of the cut wire was reduced by 90%, acoustic events were detected until the cut wire was broken at a load of approximately 16.5 kips (73.4 kN). Figures 3.5 and 3.6 present the AE parameters accumulated over time at the stage of 90% reduced cross section area, which were recorded from the first strand with the left F15I-AST and R1.5I sensors, respectively. The hits, energy and counts of AE signals suddenly increase, indicating fracture of the cut wire at 163.2 s. Thus, based on the test results, it can be seen that both types of AE sensor pairs are effective in fracture detection for the continuous tension test, in terms of different cumulative parameters..

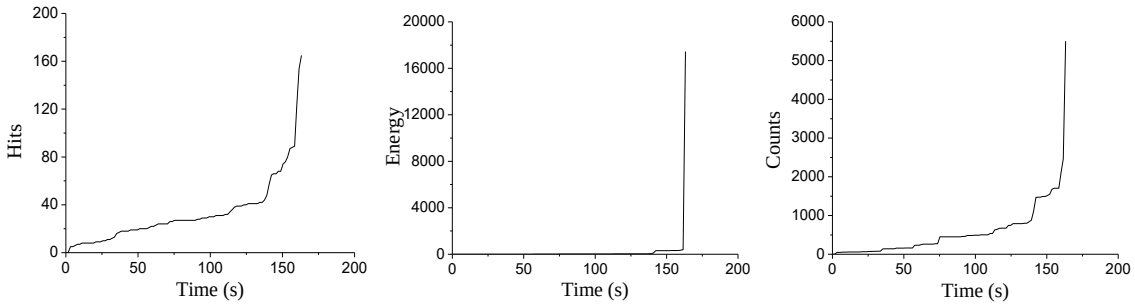

(a) Cumulative hits of AE events (b) Cumulative energy of AE event (c) Cumulative counts of AE events

Figure 3.5. Accumulated AE parameters from the left F15I-AST sensor of the 1st strand

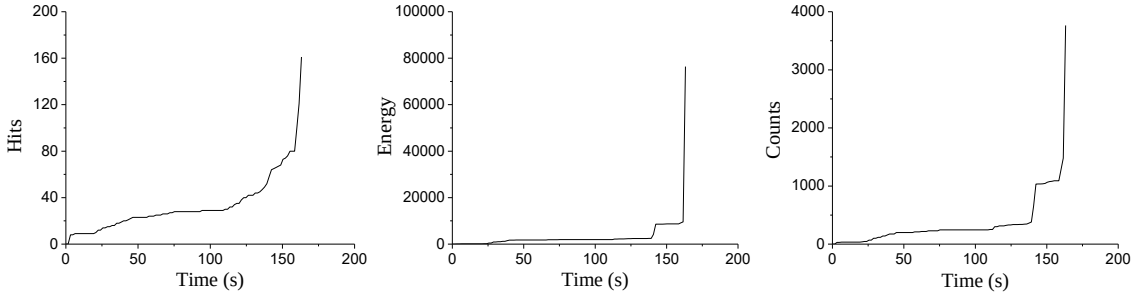

(a) Cumulative hits of AE events (b) Cumulative energy of AE event (c) Cumulative counts of AE events

Figure 3.6. Accumulated AE parameters from the left R1.5I sensor of the 1st strand

Although fracture is detectable from AE signals from one AE sensor, the source of a fracture event must be determined from occurrence time instants of the signals recorded by at least two AE sensors. Figures 3.7 and 3.8 present the number of events from various locations based on the measurements of two AE sensors (Model F15I-AST or R1.5I) on the first and second strands tested, respectively.

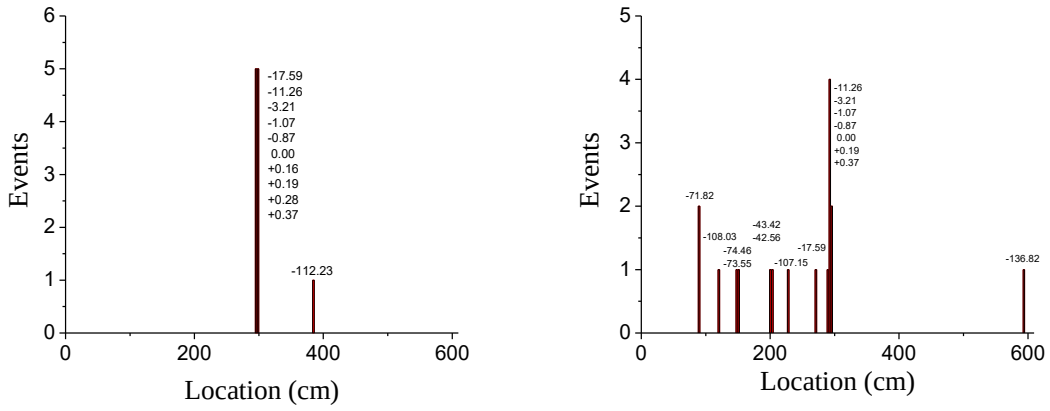

(a) A pair of F15I-AST sensors (b) A pair of R1.5I sensors

Figure 3.7. Number of events from various locations of the 1st strand (30 dB threshold)

All occurrence time instants of the captured acoustic events are marked in Figures 3.7 and 3.8, and further explained in Tables 3.2 and 3.3. The low frequency R1.5I sensors

recorded more events than the high frequency F15I-AST sensors. Note that the occurrence time instants for each event are given in Figures 3.7 and 3.8 with reference to the moment of fracture. Since fracture represents a dramatic event and suddenly generates significant energy, it is readily separable from pre- and post-fracture events such as inter-wire slippage, fracture initiation and fracture-induced echo by raising the threshold level of AE sensors. For example, with an increasing threshold of 80 dB, each fracture event can be singled out of other events as indicated in Figures 3.9 and 3.10.

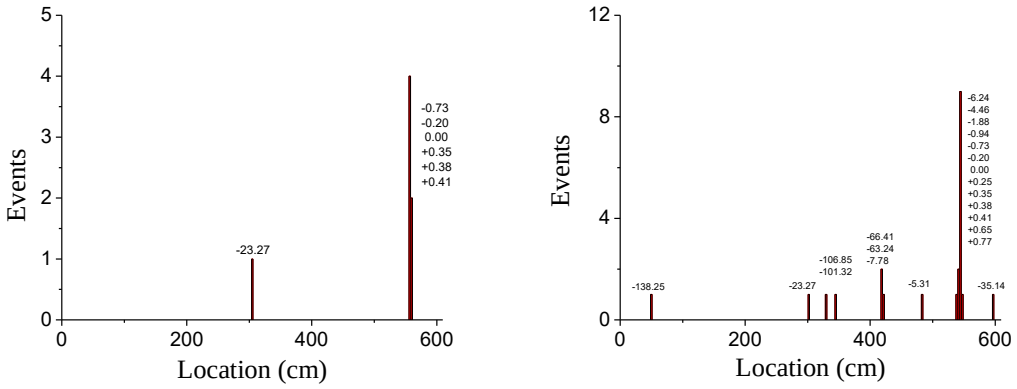

(a) A pair of F15I-AST sensors (b) A pair of R1.5I sensors

Figure 3.8. Number of events from various locations of the 2nd strand (30 dB threshold)

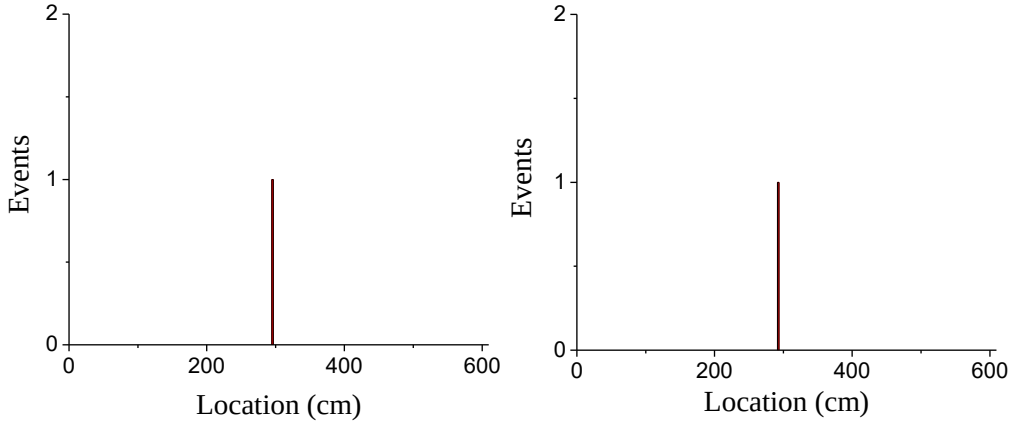

(a) A pair of F15I-AST sensors (b) A pair of R1.5I sensors

Figure 3.9. Fracture location in the 1st strand (80 dB threshold)

To quantify the accuracy of location detection from both types of the sensors, the identified sources of fracture events are compared with their ground truth data. For the first strand, the notch was physically located at 118.1 in. (300 cm) from the left support while the highest AE events from both pairs of sensors occurred from 117.7 in. (299 cm). The difference in the measured and predicted locations is about 0.4%. Similarly, the actual fracture location of the second strand was 216.5 in. (550 cm) from the left end, and the identified locations are 547 and 556, respectively, from the two types of AE sensors. The errors in location prediction are approximately 0.5% and 1.1%, which are both small and demonstrate the feasibility of fracture localization using the AE. Overall, both types of AE sensors can record signals that lead to the successful localization of fracture points with good accuracy as indicated by the highest number of events in Figures 3.7-3.10.

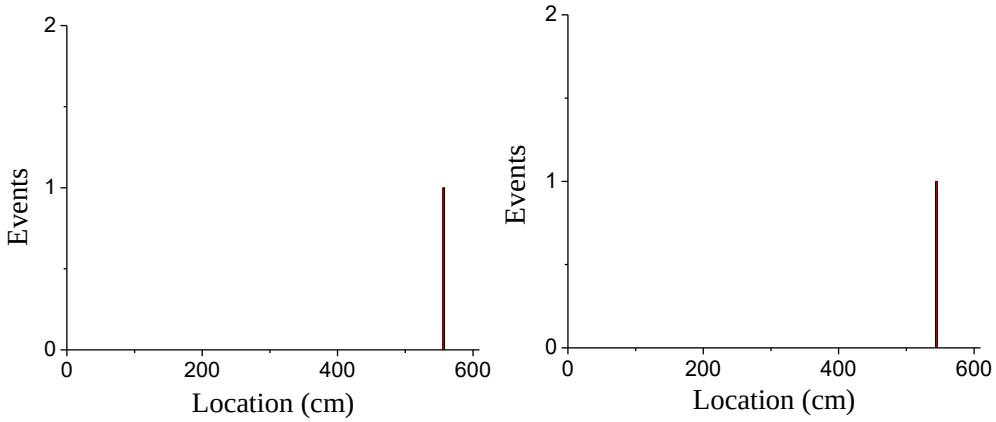

(a) A pair of F15I-AST sensors (b) A pair of R1.5I sensors

Figure 3.10. Fracture location in the 2nd strand (80 dB threshold)

The accumulated energy and counts of the AE signals as shown in Figure 3.5(b, c) or Figure 3.6(b, c) both indicate the onset of fracture at 145.61 s. The accumulated hits as shown in Figure 3.5(a) and Figure 3.6(a) indicate that slippage likely occurs between the

wires in contact at the early stage of tests setup. The significant hits, energy and counts at 50.97 s and their rapid increase at 145.61 s appear good indicators of the fracture event, which are likely associated with the effects of inter-wire slippage and fracture initiation.

To understand the sequence of various events, the occurrence time instants of acoustic events captured by a pair of F15I-AST sensors as shown in Figures 3.7(a) and 3.8(a) are presented in Tables 3.2 and 3.3 for the first and second strands, respectively. Tables 3.2 and 3.3 also include the relative occurrence time with respect to the fracture event, which are the same as those included in Figures 3.7(a) and 3.8(a). For the first strand as indicated in Table 3.2, the first event corresponded to an inter-wire slippage away from the mid-span, which occurred at 112.23 s prior to the fracture. The next five events represented the fracture initiation activities starting at 17.59 s prior to the fracture. Finally, four fracture-induced echo responses were observed up to 0.37 s after the fracture event. For the second strand as indicated in Table 3.3, the earliest single event represented the effect of an inter-wire slippage in the middle of the strand. Two fracture-initiation events were then captured at the fracture location before a fracture event actually took place. Next, three closely-spaced echoes at the fracture location were detected immediately.

Tables 3.2 and 3.3 indicate that the inter-wire slippage and the fracture initiation respectively occurred 112.23 s and 17.59 s before the cut wire of the first strand completely fractured, and 23.27 s and 0.73 s before the cut wire in the second strand was broken. The short alerting time for the fracture event is because of continuous loading in this study. For example, the first strand was subjected to additional 2 kips between the fracture initiation at 17.59 s and the fracture event. In practical applications, after wires experience the initiation of fracture likely at the location of the highest stress under maximum loading, the

stress is likely relieved immediately after the application of the maximum loading due to moving vehicles, thus making the time between the fracture initiation and the actual fracture substantially longer than over 20 s.

Table 3.2. Occurrence of various events on the 1st strand recorded from the F15I-AST sensor pair

Event Category	Occurrence Time (s)	Relative Time (s)
Inter-wire Slippage	50.97	-112.23
Fracture Initiation	145.61	-17.59
Fracture Initiation	151.94	-11.26
Fracture Initiation	159.99	-3.21
Fracture Initiation	162.13	-1.07
Fracture Initiation	162.33	-0.87
Fracture	163.20	0.00
Fracture-induced Echo	163.36	+0.16
Fracture-induced Echo	163.39	+0.19
Fracture-induced Echo	163.48	+0.28
Fracture-induced Echo	163.57	+0.37

Table 3.3. Occurrence of various events on the 2nd strand recorded from the F15I-AST sensor pair

Event Category	Occurance Time (s)	Relative Time (s)
Inter-wire Slippage	129.82	-23.27
Fracture Initiation	152.36	-0.73
Fracture Initiation	152.89	-0.20
Fracture	153.09	0.00
Fractue-induced Echo	153.44	+0.35
Fracture-induced Echo	153.44	+0.35
Fracture-induced Echo	153.50	+0.41

3.2.2. Simplified AWT Analysis of AE Signals. For wire fracture prediction, the fracture signal as indicated by the strongest AE event is not available. Therefore, the pre-

fracture signals, such as inter-wire slippage and fracture initiation, must thus be uniquely identified over time as precursors of the wire fracture. Due to low amplitude of the pre-fracture signals, noises are characterized in order to remove their effect in the early detection of wire fracture. In addition, the echo effect of surrounding objects and strand boundary conditions, associated with wire fracture, is comparable in amplitude with the pre-fracture signals and thus characterized to prevent a false positive identification of the following fracture event.

Since the pre- and post-fracture signals are as strong as noises of the foreign objects, raising the signal threshold would not allow a separation of them and advanced signal process is required to understand the different characteristics of various signals in order to separate the signals from noises. Due to its computational efficiency and effectiveness both in frequency and time identification, the simplified AWT is applied into the inter-wire slippage, fracture initiation, fracture, fracture-induced echo, and four types of artificial tapping noises. As shown later, the inter-wire slippage and fracture initiation signals stop within 0.002 s while others tend to last much longer. Therefore, high frequency resolution is selected for the first 0.002 s signal and high time resolution is used beyond 0.002 s to preserve time information. As such, a time-dependent center frequency ω_c is selected to be $2\pi(11 - 5000t)$ rad/s for $t < 0.002$ s and 2π rad/s for $t > 0.002$ s.

Following is a presentation of the multiband wavelet analysis of various acoustic signals in chronic order in terms of relative time with respect to the fracture moment (inter-wire slippage, fracture initiation, fracture, and fracture-induced echo) and four types of noises. All signals were captured by the AE sensors without any artificial manipulation, each representing an individual waveform from an acoustic event instead of the

accumulated time function from the very beginning of the test. The hit definition time (HDT) was set to 600 μs, which triggered a sudden termination of the two types of pre-fracture signals as shown in Figures 3.11-3.14. Moreover, because of high sampling rate of the AE signal, the edge effect of wavelet transform is negligible. Figure 3.11 shows the inter-wire slippage signals and their time-frequency scalograms of the first strand recorded from a pair of R15I-AST sensors at -112.23 s and a pair of R1.5I sensors at -74.45 s. Similarly, figure 3.12 shows the inter-wire slippage signals and their scalograms of the second strand from a pair of R15I-AST sensors at -23.27 s and a pair of R1.5I sensors at -35.14 s. These events occurred much earlier than the fracture event at different locations as sparsely distributed in Figures 3.7 and 3.8. These short events are rich in low frequency components. The inter-wire slippage from the two types of AE sensors are consistent since their dominant frequency is lower than the characteristic frequency of the AE sensors.

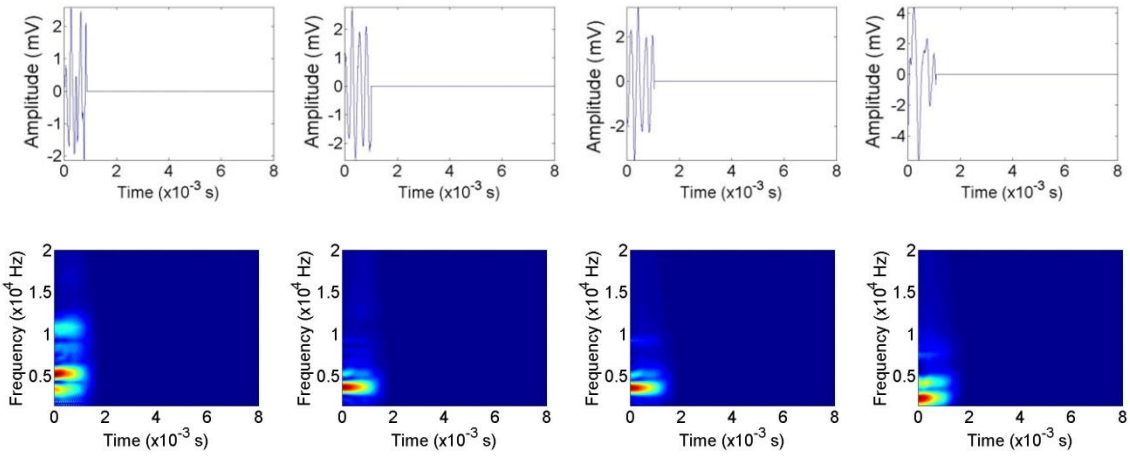

(a) F15I-AST (Left) (b) F15I-AST (Right) (c) R1.5I (Left) (d) R1.5I (Right)

Figure 3.11. Inter-wire slippage signals from the 1st strand

Without loss of any generality, two pairs of fracture initiation signals were randomly selected from a large number of data sets recorded from each strand. Figures

3.13 and 3.14 show the fracture initiation signals and their time-frequency scalograms of the first and second strands, respectively. These signals are short in time. Their energy is distributed over a wide range of frequency. All the recorded signals are consistent and repeatable in application. For the first strand, the two pairs of signals respectively occurred at -1.07 s (from the F15I-AST sensors) and -0.87 s (from the R1.5I sensors). For the second strand, the two pairs of signals occurred at -0.73 s and -0.94 s correspondingly.

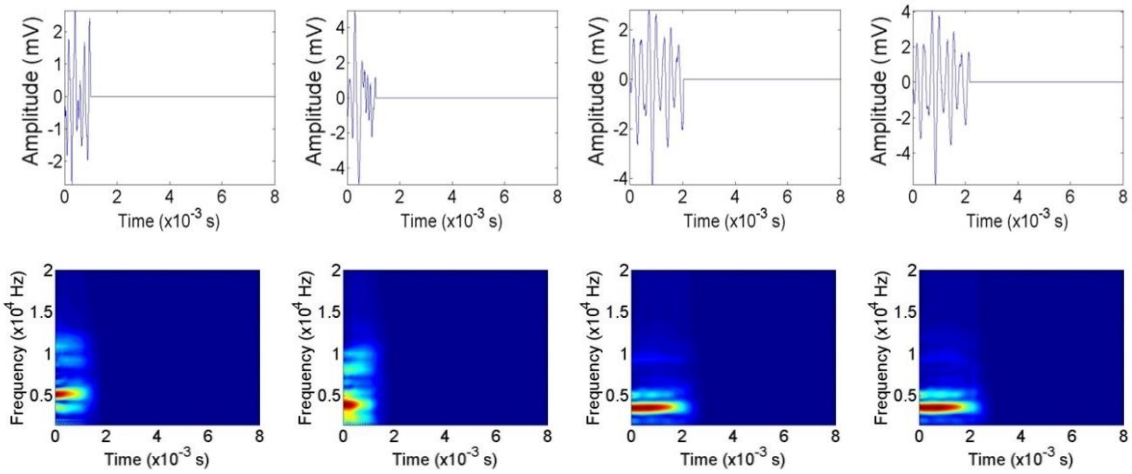

(a) F15I-AST (Left) (b) F15I-AST (Right) (c) R1.5I (Left) (d) R1.5I (Right)

Figure 3.12. Inter-wire slippage signals from the 2nd strand

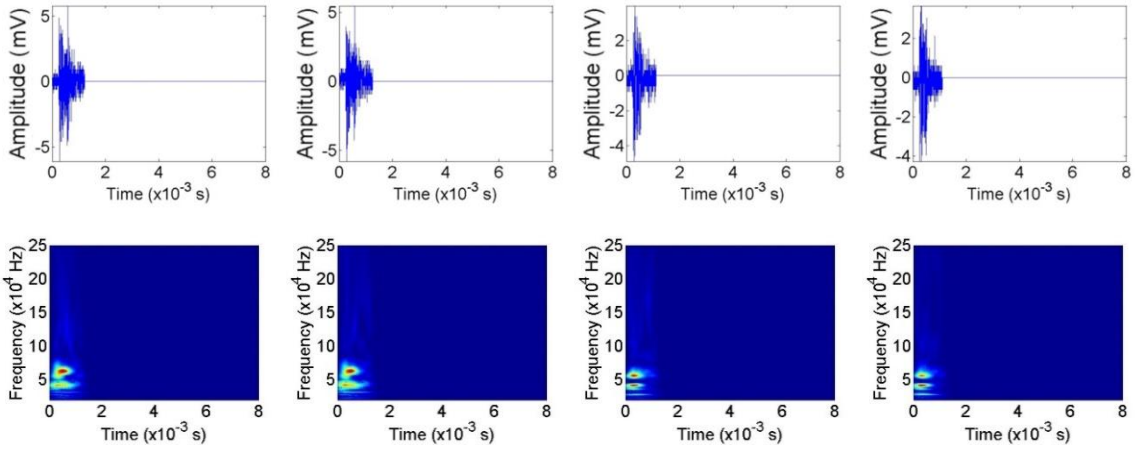

(a) F15I-AST (Left) (b) F15I-AST (Right) (c) R1.5I (Left) (d) R1.5I (Right)

Figure 3.13. Fracture initiation signals from the 1st strand

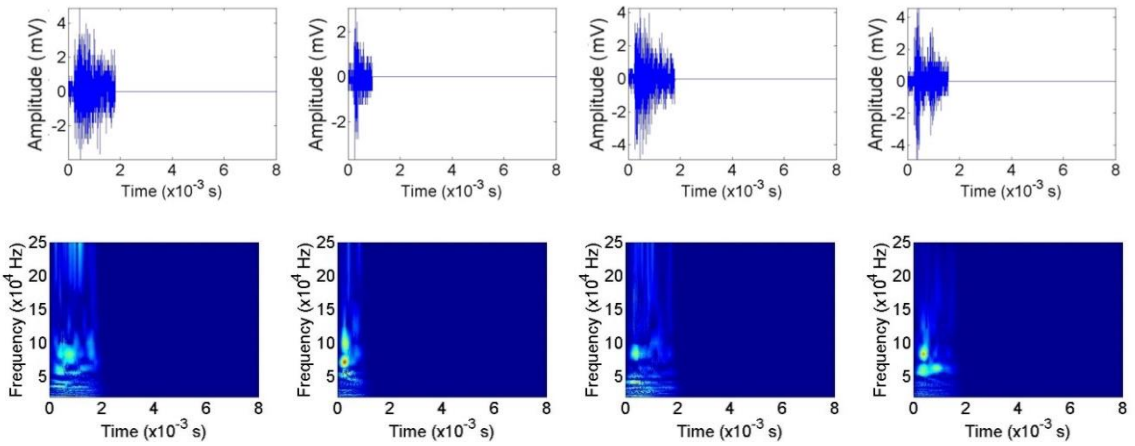

(a) F15I-AST (Left) (b) F15I-AST (Right) (c) R1.5I (Left) (d) R1.5I (Right)

Figure 3.14. Fracture initiation signals from the 2nd strand

Unlike the multiple inter-wire slippage and fracture initiation signals, only a single event recorded from two pairs of sensors was associated with the wire fracture as shown in Figures 3.15 and 3.16 for the first and second strands, respectively. Its time-frequency scalograms are also included in Figures 3.15 and 3.16. Due to an excessive amount of energy released from the fracture, all the time functions last long over time. Such energy release may also reach beyond the measurement range of the sensors (9.5 V), causing signal saturation in time domain (Figures 3.15 and 3.16) or approximation in the time-frequency scalograms. This leads to a clear separation of fracture event from others by solely considering the signal amplitude in time domain. This distinction is not changed by the signal saturation. The signals captured by the F15I-AST sensors have a wider frequency band than those by the R1.5I sensors, corresponding to the frequency characteristics of the two types of AE sensors.

Two pairs of fracture-induced echoes captured by the AE sensors were randomly selected from several data sets from each strand. Figures 3.17 and 3.18 show the echo responses and their time-frequency scalograms at +0.16 s (F15I-AST sensors) and +0.19 s

(R1.5I sensors) taken from the first strand and those at +0.35 s and +0.25 s from the second strand. All the acoustic signals attenuate over time likely because the echo responses result from multiple wave reflections at surrounding objects and strand boundaries.

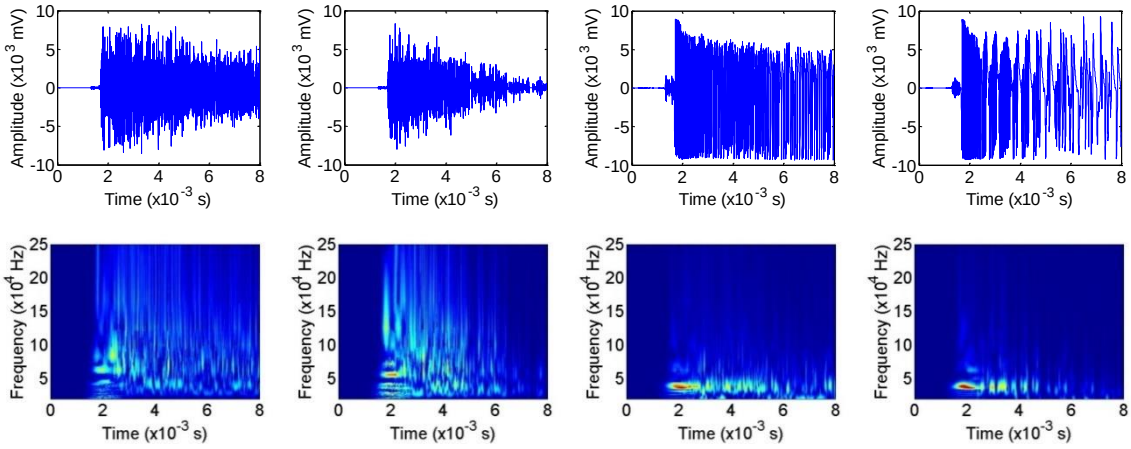

(a) F15I-AST (Left) (b) F15I-AST (Right) (c) R1.5I (Left) (d) R1.5I (Right)

Figure 3.15. Fracture signals from the 1st strand

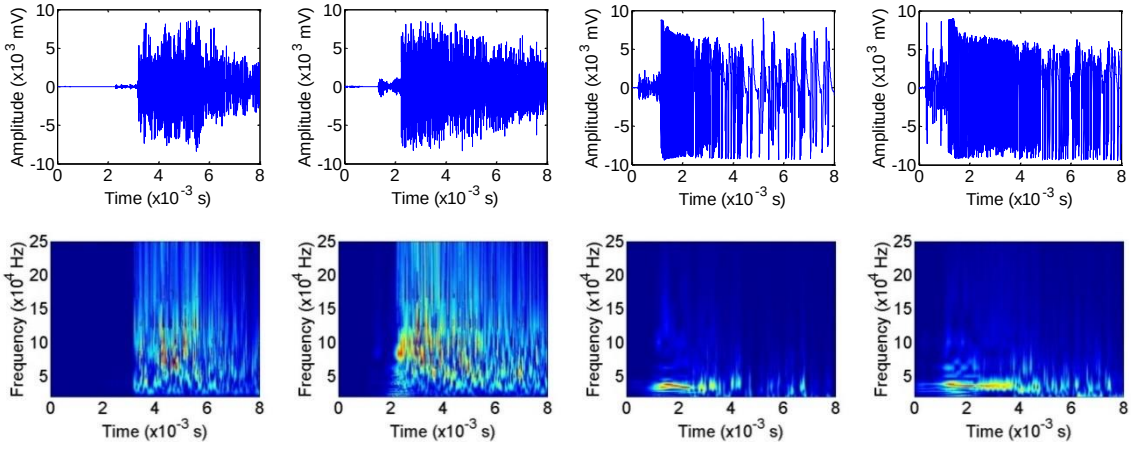

(a) F15I-AST (Left) (b) F15I-AST (Right) (c) R1.5I (Left) (d) R1.5I (Right)

Figure 3.16. Fracture signals from the 2nd strand

Traffic alarms, rain drops, and accidental impact by foreign objects such as sand particles and small gravels can potentially affect the identification results of wire fracture from AE signals. Traffic-induced noises may be filtered out with guard sensors as they are

generated from outside the sensing range. However, the rain drops on steel cables and the accidental impact of foreign objects can be difficult to remove. Artificial tapping noises as indicated in Figure 3.3 were thus generated during the tension test.

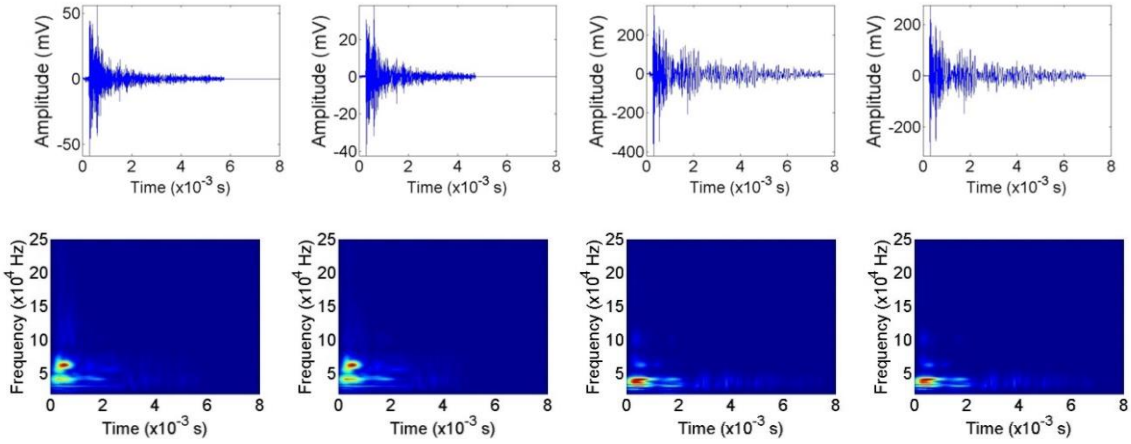

(a) F15I-AST (Left) (b) F15I-AST (Right) (c) R1.5I (Left) (d) R1.5I (Right)

Figure 3.17. Fracture-induced echo signals from the 1st strand

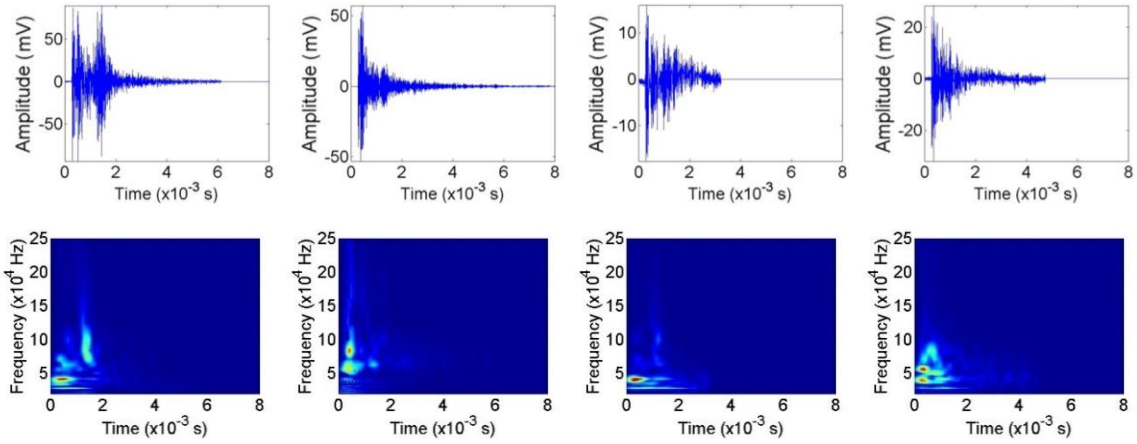

(a) F15I-AST (Left) (b) F15I-AST (Right) (c) R1.5I (Left) (d) R1.5I (Right)

Figure 3.18. Fracture-induced echo signals from the 2nd strand

Figure 3.19 presents the AE signals of artificial tappings with four types of objects (steel bar, plastic marker, steel washer, and penny) when the first strand was subjected to a load of 20 kips (~89 kN). As the characteristics of the tapping signals recorded by two

types of AE sensors are similar, only one signal from the left F15I-AST sensor of an intact strand is presented for each type of tapping noise. The noises decay rapidly over time since tapping represents an impact loading. The noise induced by the steel bar includes more high frequency components than the noise by the plastic marker. The noises induced by the steel washer and the penny are similar in frequency characteristics, in terms of amplitude and overall frequency trend.

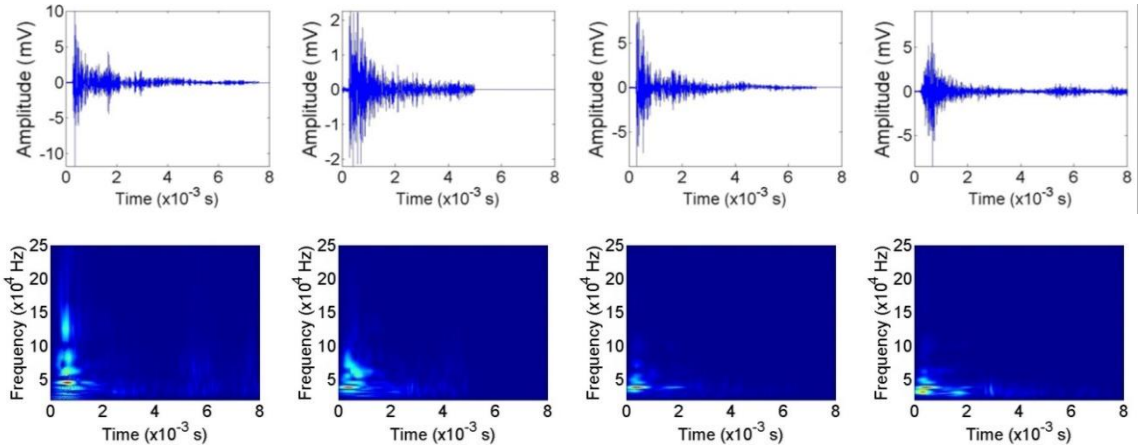

(a) Steel bar (b) Marker (c) Steel washer (d) Penny

Figure 3.19. Artificial tapping noises

3.2.3. Characteristics and Comparisons of Various Acoustic Signals. Figures 3.11-3.19 indicate that the amplitudes of the recorded AE signals are up to 10 mV due to inter-wire slippage, fracture initiation and artificial tapping, up to 50 mV due to fracture-induced echo, and up to 10 V due to wire fracture. Thus, distinguishing the inter-wire slippage and fracture initiation signals from the tapping noises is critically important for the early detection of wire fracture in steel strands and cables. The inter-wire slippage and fracture initiation signals are short in time. The fracture-induced echo responses and noises attenuate significantly over time.

For comparison purposes in time and frequency domains, the average time and the average frequency of each MBWT scalogram in Figures 3.11-3.19 were calculated. The average time ranges from 0.0006 to 0.0010 s for the inter-wire slippage signals, 0.0005 to 0.0009 s for the fracture initiation signals, 0.0037 to 0.0054 s for the fracture signals, 0.0012 to 0.0020 s for the fracture-induced echo responses, and 0.0017 to 0.0022 s for the noises. The average time ranges of the inter-wire slippage and fracture initiation signals or the fracture-induced echo responses and noises are overlapped significantly. The average time is the shortest for the inter-wire and fracture initiation signals, moderate for the fracture-induced echo responses and noises, and the longest for the fracture signals. The average frequency ranges from 2,777 to 3,905 Hz for the inter-wire slippage signals, 38,720 to 45,820 Hz for the fracture initiation signals, 50,520 to 65,420 Hz for the fracture signals, 31,290 to 41,720 Hz for the fracture-induced echo responses, and 33,370 to 39,040 Hz for the noises. The average frequency of the inter-wire slippage signals is the lowest while that of the fracture signals is the highest. The average frequencies of the fracture-induced echo responses and noises are completely overlapped. The average frequency of the fracture-initiation signals is partially overlapped with those of the fracture-induced echoes and noises.

To quantify the characteristic features of various signals, the average (Avg.) and the coefficient of variation (C.O.V.) of all the average time instants for the inter-wire slippage signals, fracture initiation signals, fracture signals, fracture-induced echo responses or noises are evaluated and summarized in Table 3.4. Similarly, the average and the C.O.V. of the average frequencies for each type of signals are calculated and included in Table 3.4. It is clearly seen from Table 3.4 that the C.O.V. values in time and frequency

are all small (< 0.23), indicating consistent measurements of each type of signals using two AE sensors from two strands. Overall, the average times or the average frequencies are well separated among the five types of signals listed in Table 3.4. In particular, they are the largest for the fracture signals. While the average frequency of the inter-wire slippage signals is the lowest, the average time instants of the slippage and fracture initiation signals are close. Both the average time and the average frequency are relatively high, which differentiate such case from others.

Table 3.4. Summary and comparison of features extracted from various types of AE signals

Signal Type	Avg. Time ($\times 10^{-3}$ s)	C.O.V in Time	Avg. Frequency (Hz)	C.O.V. in Frequency
Slippage	0.74	0.22	3,472	0.10
Initiation	0.67	0.21	41,400	0.07
Fracture	4.39	0.11	59,500	0.11
Echo	1.48	0.19	39,130	0.11
Noise	2.00	0.09	36,680	0.06

Based on the distinct features of various signals, the following four-step procedure is proposed to predict any incipient wire fracture in steel strands and cables associated with steel corrosion: (1) Distinguish the fracture initiation signal from noises in time domain. In comparison with the fracture initiation signal, noises are long in duration with significant amplitude decay over time. (2) Distinguish the fracture initiation signal from fracture-induced echo responses in time domain. In comparison with the fracture initiation signal, fracture-induced echo responses are at least three times larger in amplitude. In addition, the echo responses must immediately follow a fracture event that is identifiable in time domain from a sudden energy release. (3) Distinguish the fracture initiation signal from inter-wire

slippage signals in frequency domain. In comparison with the fracture initiation signal, inter-wire slippage signals have lower frequency components. (4) Conduct a statistical analysis on the prediction results from multiple sets of acoustic signals.

By using the above procedure, the fracture initiation events can be identified from all acoustic events recorded from the two strands as displayed in Figures 3.7 and 3.8. Figures 3.20 and 3.21 summarize the identified fracture initiation events for the first and second strands, respectively. For the first strand, both pairs of sensors detect the fracture initiation events at virtually the same area. For the second strand, however, two events were detected away from the fracture location, which is likely due to the contamination from other signals. The false positive identification for the fracture initiation events occurs only from the R1.5I sensors. This is likely because the fracture initiation and inter-wire slippage signals are similar in many aspects and, more importantly, their frequencies fall into two sides of the resonant frequency (14 kHz) of R1.5I sensors so that the MBWT can be amplified locally around the resonant frequency. On the other hand, the characteristic frequencies of F15I-AST sensors are much higher than that of the fracture initiation signal, which is in turn higher than that of the inter-wire slippage signal.

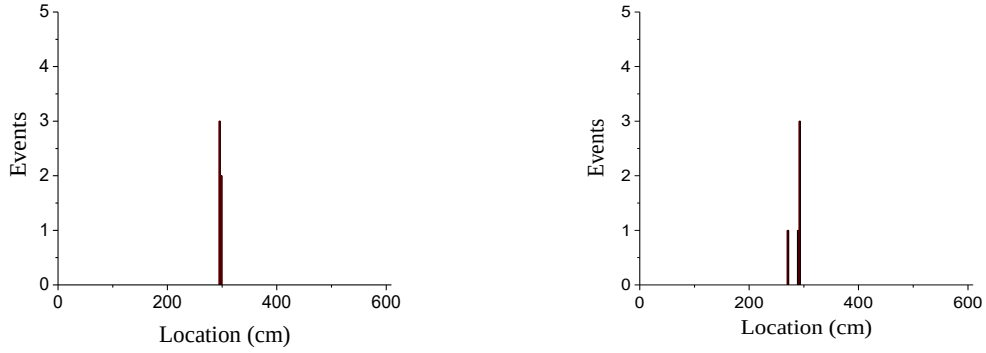

(a) A pair of F15I-AST sensors (b) A pair of R1.5I sensors

Figure 3.20. Number of fracture-initiation events from the 1st strand

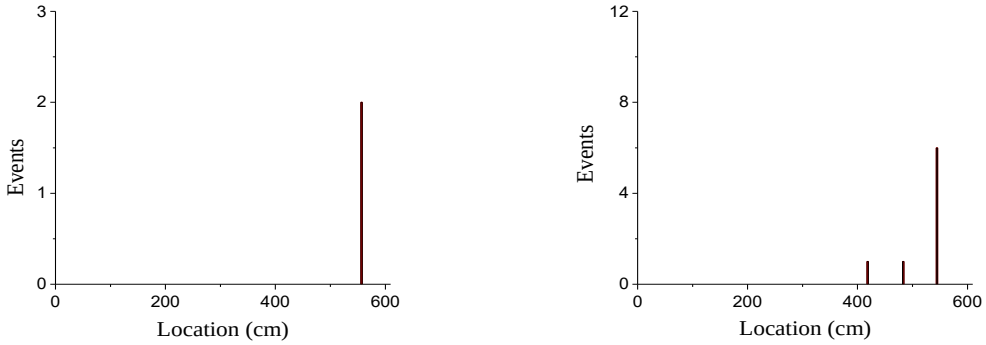

(a) A pair of F15I-AST sensors (b) A pair of R1.5I sensors

Figure 3.21. Number of fracture-initiation events from the 2nd strand

3.3. SUMMARY

In this section, AE features to predict and detect wire fracture in seven-wire strands were characterized with multiband wavelet analysis, a simplified version of AWT. Two steel strands were tested up to 20 kips (89 kN) with each instrumented with a pair of AE sensors at two ends. The cross section of one wire was locally reduced up to 90% in 10% increment at center and support of the two strands, respectively. For both strands, the AE parameters (hits, energy, and counts) changed little up to 80% reduction in cross section of the partially cut wire, and suddenly jumped at the fracture (under 16.4 kips or 73 kN) of the notched wire with 90% reduction in cross section.

Prior to wire fracture, acoustic events of inter-wire slippage and fracture initiation were observed from a steel strand of seven wires. In comparison with the fracture initiation signals, the inter-wire slippage signals have substantially lower frequency components and similar time duration. Wire fracture can be detected with any of hit, energy, and count parameters calculated from a recorded acoustic emission signal. It can be located from a distribution of events over the length of a test strand, which are registered by at least two acoustic emission sensors. The frequency bandwidth of wire fracture signals is much wider

than that of fracture-induced echo responses or artificial tapping noises. Both the fracture signals and the noises are long in time duration. Acoustic signals of fracture initiation possess unique time-frequency characteristics such as wide frequency bandwidth and short time duration. These characteristics can be used as fracture warning in application. For wire fracture prediction, the high frequency acoustic sensors result in less number of false positive identifications.

4. TIME-FREQUENCY FEATURE EXTRACTION OF IMPACT ECHO SIGNALS FOR DELAMINATION DETECTION

4.1. CONCRETE SLAB SPECIMEN AND IMPACT ECHO TESTS

Impact Echo (IE) technique has been demonstrated to be an effective tool for delamination detection in thin concrete structures [62]. In this study, a 60"×36"×7.25" concrete slab with pre-embedded defects is used as an application example of the proposed AWT. Figure 4.1(a) shows the overall dimensions, steel reinforcement, and six artificial defects of the slab specimen. The defects made of foams and cardboards, as detailed in Table 4.1, are used to simulate three conditions: shallow, deep, and no delamination. Shallow delamination is associated either with long-duration flexural vibration of plate-like structures or long-duration surface wave reflection from the boundaries of finite-dimension structures under impact loads. Deep and no delamination are associated with the direct reflection of impact-induced wave at the delamination depth and at the bottom of the slab, respectively. As shown in Figure 4.1(b), a Portable Seismic Property Analyzer (PSPA) was used to generate and record IE signals from the concrete slab while in formwork [79]. A total of 40 measurements were taken as detailed in Figure 4.1(c).

Deep and no delamination are associated with the body wave reflection at delamination or at the bottom edge of the slab. The corresponding resonant frequency can be related to the delamination depth or slab thickness, d, in Equation (16):

$$f = \frac{\beta_1 V}{2d} \tag{16}$$

where $\beta_1 = 0.96$ for plate-like structures, and V=126,000 in./s is the P-wave velocity in concrete. For no delamination of the 7.25-in thick slab, the resonant frequency is approximately 8,340 Hz. Thus, frequency components that are higher than 8,340 Hz are

expected of the deep delamination, corresponding to a certain delamination depth. This allows the differentiation of frequency components of all three cases.

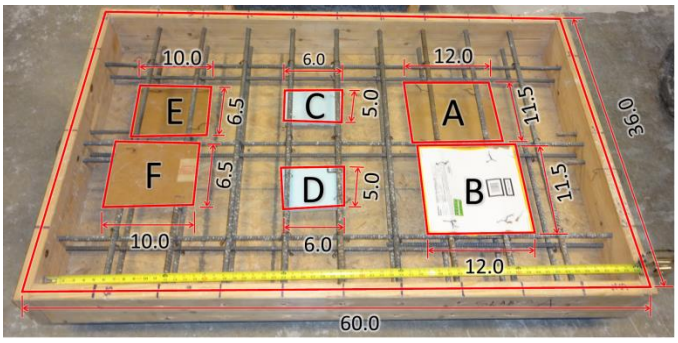

(a) Simulated delamination with foams and cardboards

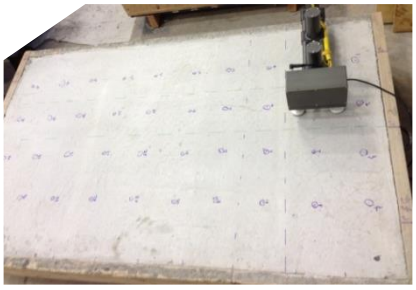

(b) IE intrumentation

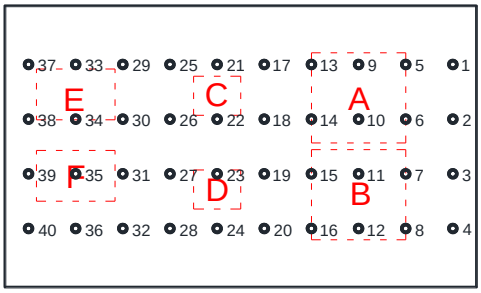

(c) Distribution of 40 measurement points

Figure 4.1. IE test setup

During IE tests, data were recorded at a sampling rate of 390 kHz. The natural frequencies of the flexural mode of vibration are often lower than the resonant frequency associated with wave reflection at the delamination depth but likely close to the resonant frequency associated with wave reflection at the bottom face of the slab. As a result, the

ranges of resonant frequencies related to various delamination conditions are generally overlapped and time-frequency analysis is necessary in discriminating their conditions.

The fundamental frequency of the flexural mode vibration can be related to the depth and width of delamination, d and c, by the semi-analytical equation developed for rectangular defects [81]:

$$f = \varepsilon\beta_1 \frac{V}{d}\left(\frac{d}{c}\right)^2 \tag{17}$$

in which $\beta_1 = \pi\sqrt{1-2\nu}/\sqrt{12(1-\nu)^2}$ is a function of the Poisson's ratio of concrete, ν $(= 0.3)$, and $\varepsilon = 1.64e^{0.0014c/d} - 1.812e^{-0.22c/d}$ is a correction factor of Equation (17). The theoretical frequencies associated with the embedded defects are calculated from Equations (16) and (17), as given in Table 4.1.

Table 4.1. Artificial defect properties

Defect	Plan Dimension (in. × in.)	Thickness (in.)	Embedment Depth (in.)	Material	Frequency (Hz)	
					Eq. (16)	Eq. (17)
A	12.0×11.5	--	6.250	Cardboard		
B	12.0×11.5	--	1.875	Cardboard	--	9677
C	6.0×5.0	1.000	5.250	Foam	1732	--
D	6.0×5.0	1.000	2.500	Foam	--	11520
E	10.0×6.5	--	6.250	Cardboard	4928	--
F	10.0×6.5	--	1.875	Cardboard	--	9677
					3676	--

4.2. APPLICATION OF AWT TO IMPACT ECHO SIGNALS

Figure 4.2 shows three representative IE signals and their corresponding CWTs ($\omega_c = 2\pi$ rad/s) at three measurement points (#9, #28, and #11) with deep delamination (> 4 in), no delamination, and shallow delamination (< 4 in), respectively. The frequency bandwidth of the CWT scalogram at Point #9 with deep delamination was higher than that at Point

#28 with no delamination since the impact-induced stress (sound) waves travelled inside the concrete slab were reflected from the embedded object and the bottom surface, respectively. At Point #28 with no delamination, the CWT scalogram resulted in a concentration of time (< 0.0015 s) and frequency (< 8,340 Hz). At Point #11 with shallow delamination, the CWT scalogram appeared quite different from those at Points #9 and #28 because the IE response at Point #11 was dominated by the propagation of surface stress waves with the frequency information related to the shallow delamination depth less or not detectable. Specifically, the CWT scalogram at Point #11 is long in time duration (>0.0015 s) and narrow in frequency bandwidth (<8,340 Hz).

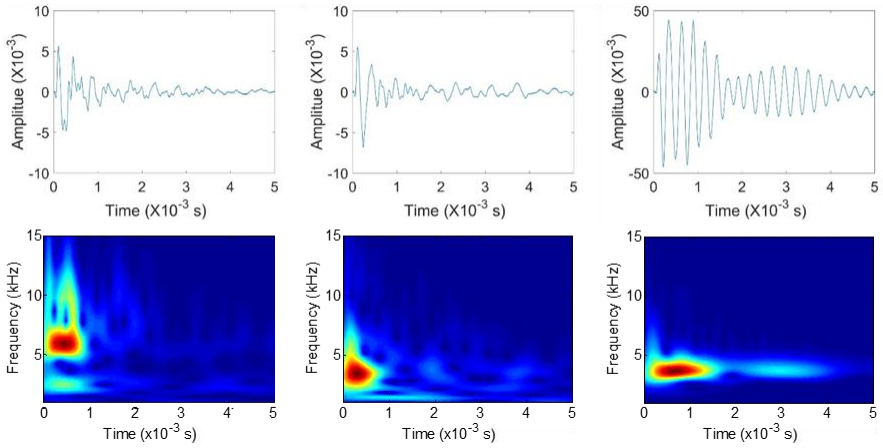

(a) Point #9 (b) Point #28 (c) Point #11

Figure 4.2. IE signals and their CWT scalograms at three points ($\omega_c = 2\pi$ rad/s)

Even if the center frequency is increased to $\omega_c = 10\pi$ rad/s, the CWT with fixed wavelet parameters cannot provide satisfactory time and frequency resolution for the accurate identification of resonant frequencies. Figure 4.3 presents the new CWT scalograms of the IE signals at Points #28 and #11. Although the frequency components at Point #28 are relatively easier to discern in comparison with Figure 4.2(b), distinction

between no delamination in Figure 4.3(a) and shallow delamination in Figure 4.3(b) remains a challenge particularly when their time resolution becomes comparable.

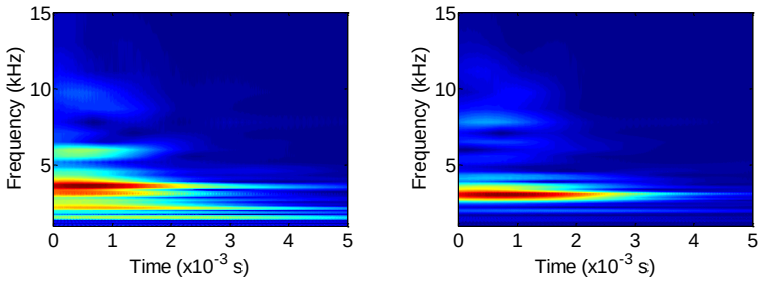

(a) Point #28 (b) Point #11

Figure 4.3. CWT scalograms of the IE responses ($\omega_c = 10\pi$ rad/s)

For deep delamination at Point #9, the IE signal as indicated in Figure 4.2(a) is concentrated before 0.001 s. Take the instantaneous spectrum at 0.00035 s as an example. As shown in Figure 4.4, one of the two peaks is centered at 12,750 Hz and ranges from 6,980 Hz to 18,510 Hz. It has a frequency bandwidth or ridgeline thickness of 11,530 Hz, which exceeds the calculated ridgeline thickness of 8,150 Hz corresponding to the current frequency resolution. Therefore, the local frequency resolution needs to be refined by increasing the center frequency to 16 Hz, following the AWT algorithm. The signal after 0.001 s attenuates dramatically and becomes less important. The center frequency is thus kept as 1 Hz afterwards, as indicated in Figure 4.5 for the overall center frequency as a function of time determined from the optimization algorithm at each time. The corresponding scalogram from the AWT is shown in Figure 4.6 with a clear separation of all frequency components for delamination depth identification. It is also observed from Figure 4.6 that the identified frequencies are nearly unchanged over time, at least prior to 0.001 s. The highest frequency component (9,750 Hz) corresponds to a delamination depth

of 6.2 in. ($= \beta V/2/f = 0.96 \times 126000/2/9750$). Though only the highest frequency component is needed, other components are explained here for completeness. The second highest frequency component represents the wave reflection from the bottom of the slab. The lowest two frequencies come from the surface wave reflections at the short and long edges of the slab. The other components in between defects likely result from the wave reflection from the adjacent defects. The improvement in frequency identification is critically important since deep delamination often occurs near the bottom face of bridge decks with prestressed tendons.

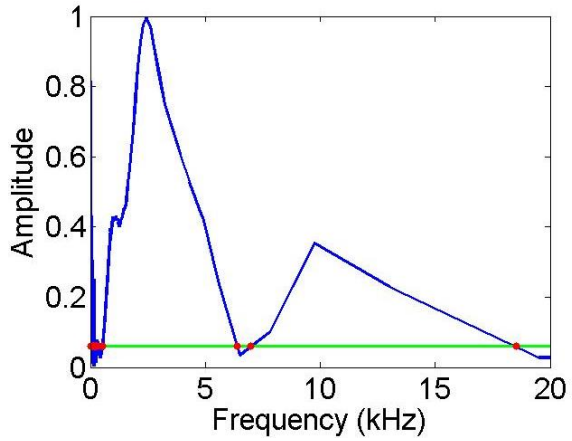

Figure 4.4. Instantaneous spectrum at 0.00035 s

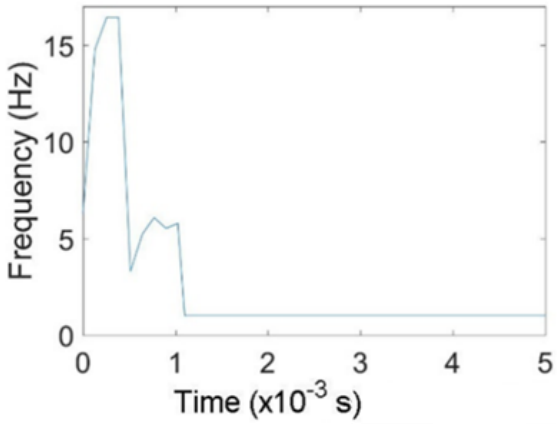

Figure 4.5. Time-varying center frequency

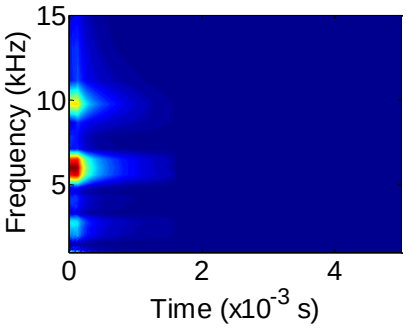

Figure 4.6. AWT of the IE signal for deep delamination at location #6

To demonstrate the robustness of the proposed AWT, additional three points (#10, #22, and #34) with deep delamination are considered. Whenever an instantaneous CWT spectrum with $\omega_c = 2\pi$ rad/s, similar to Figure 4.2, has one or more peaks at a frequency of above 8,340 Hz, the same AWT procedure is followed. Figures 4.7 and 4.8 compare the CWT and AWT scalograms at Points #10, #22 and #34. The comparison clearly indicates that the frequency components are significantly easier to identify with the proposed AWT. Together with Figure 4.6, the highest resonant frequencies identified with the AWT are 9,750 Hz, 9,750 Hz, 11,850 Hz and 9,700 Hz at Points #9, #10, #22, and #34, respectively. With Equation (16), the resonant frequencies are converted to a delamination depth of 6.20 in, 6.20 in, 5.10 in and 6.24 in, which are in excellent agreement with the actual delamination depths (6.25 in, 6.25 in, 5.25 in, and 6.25 in) as given in Table 4.2.

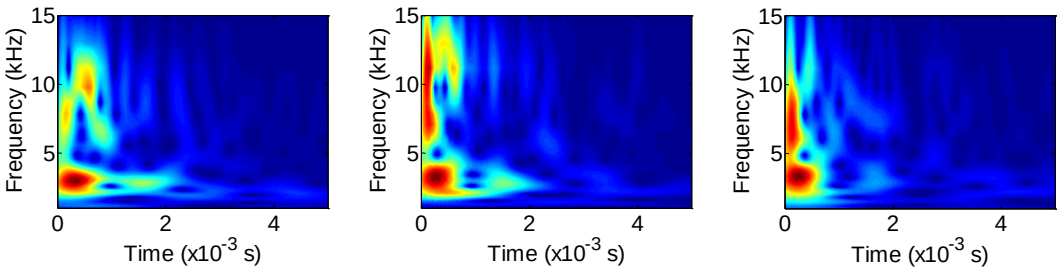

(a) Point #10 (b) Point #22 (c) Point #34

Figure 4.7. CWT scalograms at locations with deep delamination ($\omega_c = 2\pi$ rad/s)

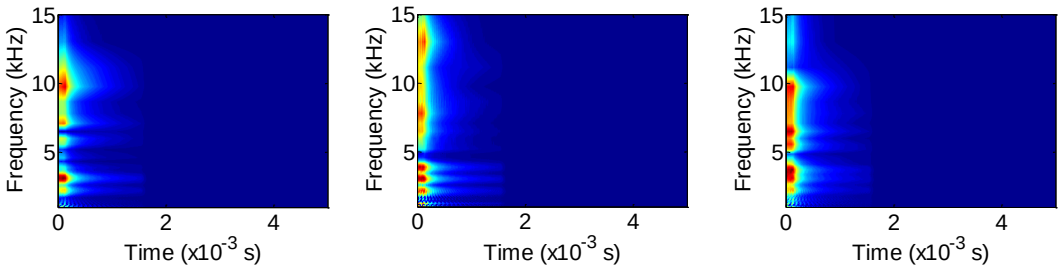

(a) Point #10 (b) Point #22 (c) Point #34

Figure 4.8. AWT scalograms at locations with deep delamination

In the case of no delamination, the frequency components higher than 8,340 Hz are negligible. Therefore, after going through the optimization algorithm of AWT, the center frequency is still kept at 1 Hz. Thus, the AWT gives the same results as the CWT in this case. Figure 4.9 shows the AWT scalograms at additional three locations with no delamination (Points #1, #30 and #40). The scalograms in Figures 4.2(b) and 4.9 share the same time-frequency characteristics, all corresponding to the thickness of the tested concrete slab.

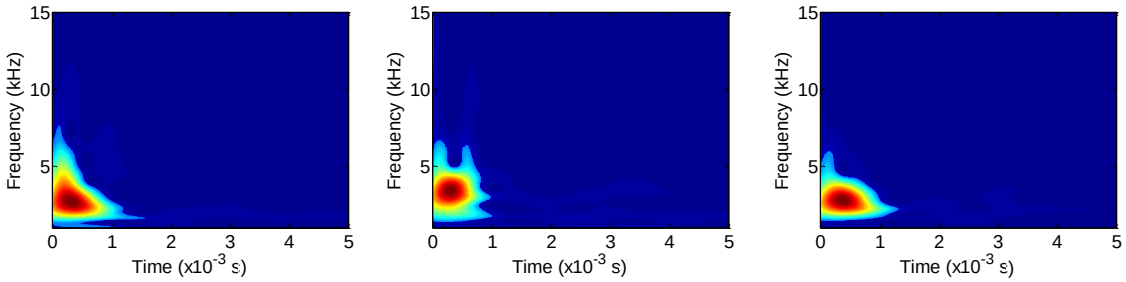

(a) Point #1 (b) Point #30 (d) Point #40

Figure 4.9. AWT scalograms at locations with no delamination

When shallow delamination is concerned, the signal is dominated by the flexural modes with much longer time duration for the concrete slab with finite dimensions, and frequency components higher than 8,340 Hz are not present. As shown in Figure 4.10 for

the instantaneous spectrum at 0.003 s, the ridgeline thickness of the surface wave is 2,580 Hz from the wavelet transform with a center frequency of 1 Hz. However, the single peak is centered at 3,710 Hz and the calculated ridgeline thickness corresponding to the current frequency resolution is 2,630 Hz. Thus, shallow delamination can be treated in the same way as no delamination as far as the AWT analysis is concerned. The AWT scalograms at additional three points (#12, #23, and #35) with shallow delamination are presented in Figure 4.11. It can be seen from Figures 4.2(c) and 11 that all the scalograms retain the time duration of larger than 0.002 s.

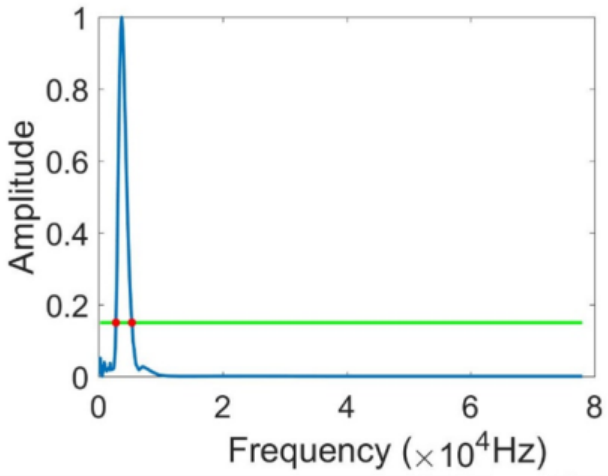

Figure 4.10. Instantaneous spectrum of the IE signal at 0.003 s with shallow delamination at Point #35

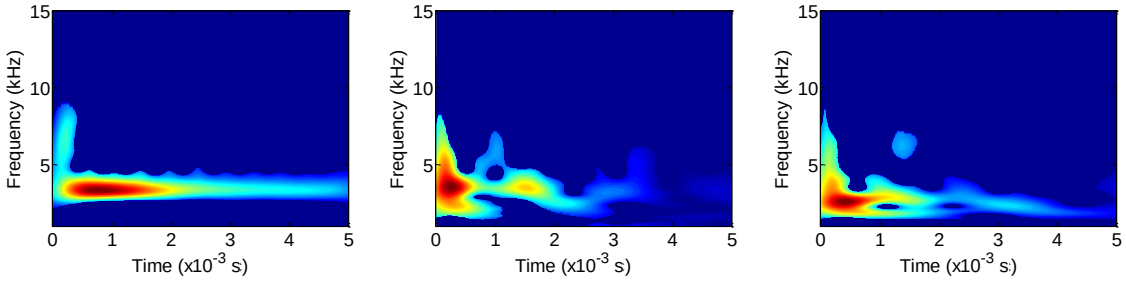

(a) Point #12 (b) Point #23 (c) Point #35

Figure 4.11. AWT scalograms at locations with shallow delamination

The identified results of delamination with the AWT at 40 points are summarized in Table 4.2. Deep delamination (D), no delamination (N), and shallow delamination (S) were correctly detected at all but 2 points, which indicates the effectiveness of the proposed AWT in practical application. The depths of deep delamination are all determined with high accuracy (< 3% in error). The two exceptions at Points #7 and #13 give false negative detections. These two points are located near the top corners of Defects A and B with flexible cardboards. The corners of such cardboards could be easily bent at the time of concrete casting, thus creating a no-delamination condition that coincides with the identified result. In addition, a small deviation of the two PSPA deployments towards nearby no-delamination zones is quite possible.

In contrast, the dominant frequencies corresponding to deep delamination cannot be identified from the CWT scalograms when $\omega_c = 2\pi$ rad/s, thus giving no delamination depth. If $\omega_c = 10\pi$ rad/s is used for resonant frequency identification, shallow delamination cannot be differentiated from no delamination with the CWT.

Table 4.2. Identified delamination results at all 40 locations with the proposed AWT

Location	Type	Location	Type	Location	Type	Location	Type
1	N	11	S	21	N	31	N
2	N	12	S	22	D (5.10 in)	32	N
3	N	13	*N (false)*	23	S	33	N
4	N	14	D (6.24 in)	24	N	34	D (6.24 in)
5	D (6.17 in)	15	S	25	N	35	S
6	D (6.24 in)	16	S	26	N	36	N
7	*N (false)*	17	N	27	N	37	N
8	S	18	N	28	N	38	N
9	D (6.20 in)	19	N	29	N	39	N
10	D (6.20 in)	20	N	30	N	40	N

Note: the delamination depth is given in parenthesis in the case of deep delamination.

4.3. APPLICATION OF SSAWT TO IMPACT ECHO SIGNALS

The proposed SSAWT is also applied to the impact echo (IE) signals of the same concrete slab as summarized in Table 4.1. The defects are introduced to simulate conditions of shallow and deep delamination. Based on the previous studies on the same or similar structures [79, 80], shallow delamination is associated with the long time duration flexural vibration of plate-like structures (either the entire concrete slab or the small segment right above the shallow delamination) or long-duration surface wave reflection from the boundaries of finite-dimension structures under impact loads. In total, there are three cases: no, shallow, and deep delamination.

Figure 4.12 shows two representative IE signals and their corresponding CWTs (ω_c = 2π rad/s and 10π rad/s) at measurement points #18 and #12 with no delamination and shallow delamination, respectively. It can be clearly seen from Figure 4.12 that the time-frequency representations from the CWT are limited by the Heisenberg uncertainty principle. With the lower center frequency, time resolution is higher but the characteristic frequencies cannot be identified. As a result, it remains a challenge to distinguish no delamination from shallow delamination. With the higher center frequency, frequency resolution is much higher but the time duration becomes skewed. Similarly, the CWTs of signals with $\omega_c = 2\pi$ rad/s are ineffective in identifying deep delamination as illustrated in Figure 4.13 at four measurement points (#9, #10, #22 and #34). Therefore, the flow diagram in Figure 2.15 was applied to determine the optimum center frequencies over time as presented in Figure 4.14. With the time-varying center frequencies in AWT, frequency components in the signals can be well separated with short time duration, as shown in Figure 4.15.

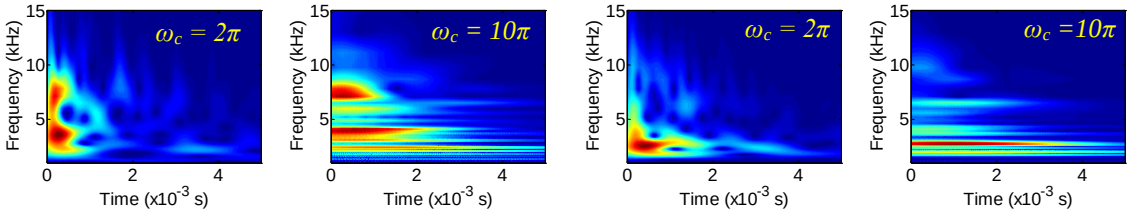

(a) Point #18 (b) Point #12

Figure 4.12. CWT scalograms of IE signals at two locations: no delamination versus shallow delamination

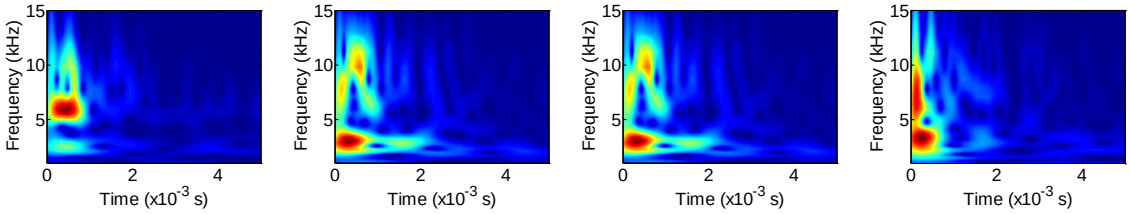

(a) Point #9 (b) Point #10 (c) Point #22 (d) Point #34

Figure 4.13. CWT scalograms of deep delamination signals ($\omega_c = 2\pi$ rad/s)

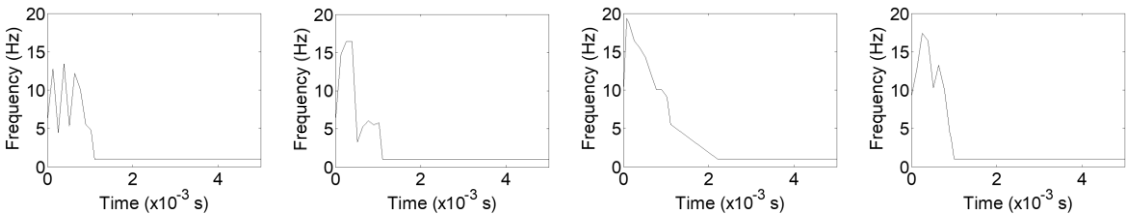

(a) Point #9 (b) Point #10 (c) Point #22 (d) Point #34

Figure 4.14. Optimum center frequencies over time

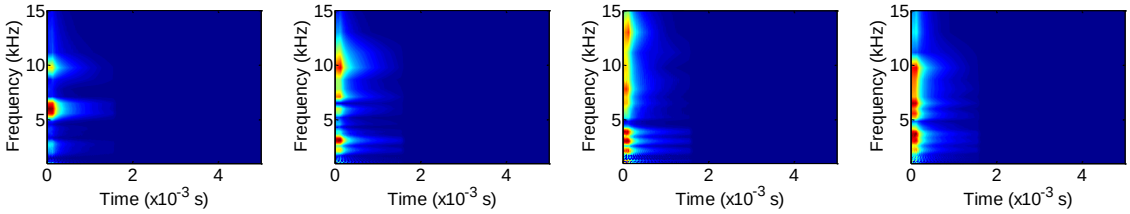

(a) Point #9 (b) Point #10 (c) Point #22 (d) Point #34

Figure 4.15. AWT scalograms of deep delamination signals

AWTs with the optimum center frequencies in Figure 4.16 were further synchro-squeezed to accurately identify the deep delamination from the measured signals at points

#9, #10, #22 and #34. As shown in Figure 4.17, the time-frequency representations with the proposed SSAWT have clearly separable frequency components. Considering the nearly consistent frequency components in a short time period as shown in Figure 4.16, the instantaneous frequency spectra from the SSAWT were accumulated over time, leading to the so-called enhanced frequency spectrum as detailed in Figure 4.17. Since the enhanced frequency spectrum includes many low peaks, the largest peak above 7,500 Hz corresponding to a slab thickness of 8 in., which exceeds the actual slab depth, is selected to identify the characteristic frequency at the delamination/slab depth. These resonant frequencies are 9,600 Hz, 9,700 Hz, 11,600 Hz and 9,700 Hz, and converted through Equation (16) to delamination depths of 6.30 in., 6.24 in., 5.21 in. and 6.24 in. for points #9, #10, #22 and #34, respectively. The identified deep delamination depths are within a maximum error of 1.5% in comparison with their theoretical values. Compared with the FT results as shown in Figure 4.18, which are commonly used in current practices, the enhanced frequency spectra in SSAWT are sharper with well-separated frequency components.

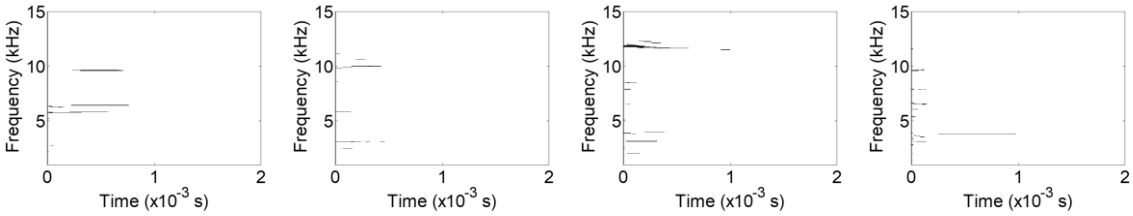

(a) Point #9 (b) Point #10 (c) Point #22 (d) Point #34

Figure 4.16. SSAWT scalograms of IE signals with deep delamination

Note that several low-frequency significant peaks (generally below 5 kHz) are observed in Figure 4.17. In particular, the peaks observed at Points #10, #22, and #34 are

mainly associated with the flexural vibration modes of their adjacent shallow defects (B, D, F). As given in Table 4.1, the theoretical fundamental flexural modes of the shallow defects range from 1.5 to 5 kHz. Since the shallow defects are embedded in close distance with the deep defects, their flexural mode responses may be generated and captured by the PSPA at the measurement points close to the deep defects. The presence of even higher frequency components (5-8 kHz) could result from the flexural modes higher than the fundamental modes [80-83]. Although a finite concrete slab could generate reflected surface waves from its side edges, the reflection effect in this study is likely negligible. The frequency of side-reflected surface waves mainly ranges from 100,000 (in./s)/[2×60 (in.)]/1000 = 0.83 kHz to 100,000 (in./s)/[2×36 (in.)]/1000 = 1.39 kHz, corresponding to the long and short side dimension, when a surface wave velocity of 100,000 in./s is used [84]. This reflection frequency is below the lower bound of the PSPA bandwidth (2 kHz).

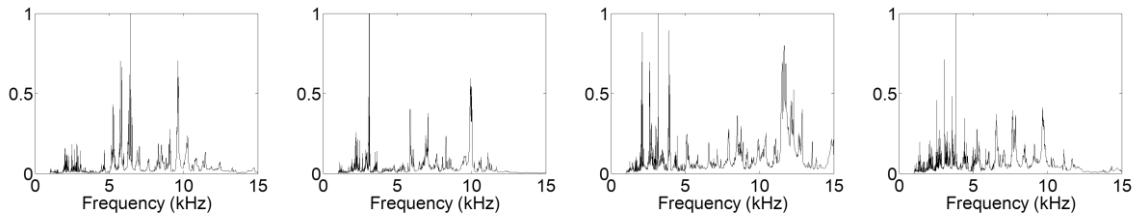

(a) Point #9 (b) Point #10 (c) Point #22 (d) Point #34

Figure 4.17. Enhanced frequency spectrum of deep delamination signals

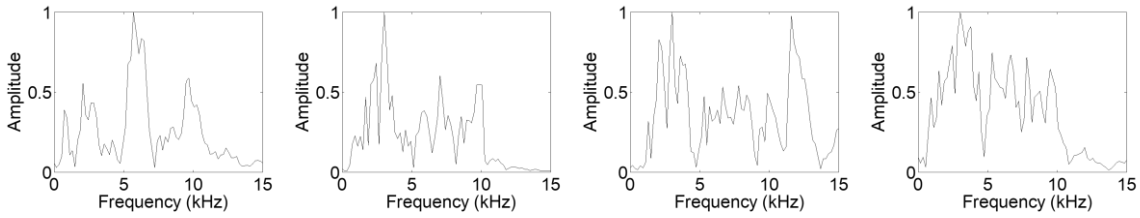

(a) Point #9 (b) Point #10 (c) Point #22 (d) Point #34

Figure 4.18. FTs of deep delamination signals

The SSAWTs at four locations (#2, #18, #20 and #27) with no delamination are presented in Figure 4.19. Since the duration of signals at these locations is short, the instantaneous frequency spectra in each scalogram are accumulated into an enhanced frequency spectrum as presented in Figure 4.20. The frequencies identified in these cases are lower than those for deep delamination. They are 8,400 Hz, 8,000 Hz, 8,500 Hz and 8,400 Hz, corresponding to a slab thickness of 7.20 in., 7.28 in., 7.56 in. and 7.20 in. at the four locations, respectively. The error of the identified slab thickness is less than 5%.

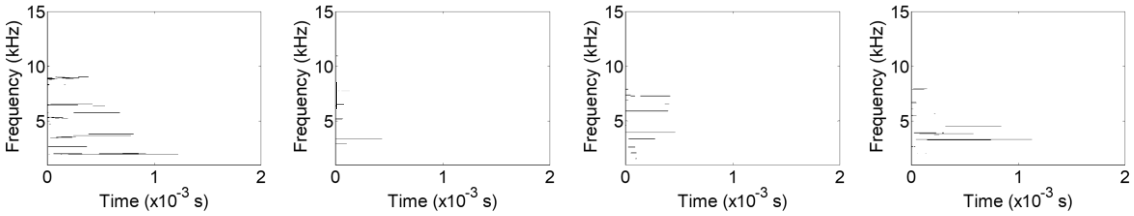

(a) Point #2 (b) Point #18 (c) Point #20 (d) Point #27

Figure 4.19. SSAWT scalograms of IE signals with no delamination

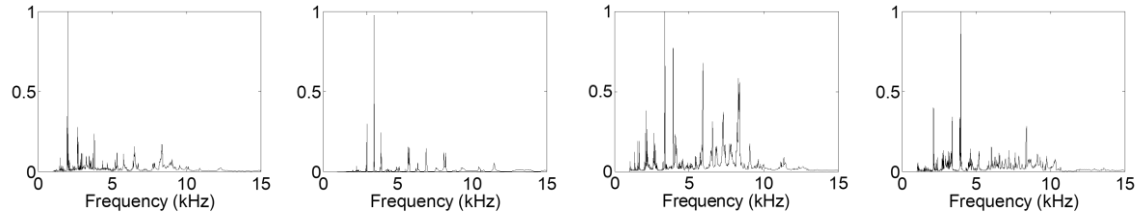

(a) Point #2 (b) Point #18 (c) Point #20 (d) Point #27

Figure 4.20. Enhanced frequency spectrum of no delamination signals

Similarly, the AWT and SSAWT of signals at four locations (#11, #12, #23 and #35) with shallow delamination are presented in Figures 4.21 and 4.22, respectively. Although Equation (16) is not applicable to the shallow delaminated area [81, 82], the low-frequency dominant, long-duration PSPA signal makes the shallow delamination differentiable from other delamination cases. The flexural mode responses are vibratory

over relatively long time with concentrated low frequency components [83]. The so-called enhanced frequency spectra are thus not evaluated as the long time duration is a character to preserve in order to differentiate shallow delamination from others. A single low frequency component dominates each scalogram in the time-frequency plane, representing the fundamental flexural mode of the slab. Frequency components that are approximately twice the dominant frequency are present in some cases as the higher frequency mode frequencies are approximately proportional to the number of mode. There are also weak indications of slab bottom reflections in the signals of Points #23 and #35 as defects D and F are smaller in dimension, which may cause energy leaks of the body waves.

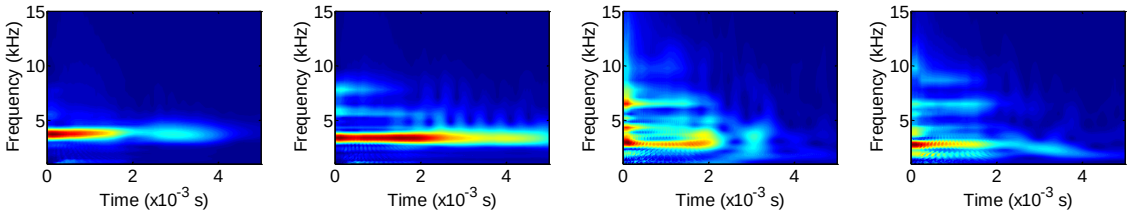

(a) Point #11 (b) Point #12 (c) Point #23 (d) Point #35

Figure 4.21. AWT scalograms of IE signals with shallow delamination

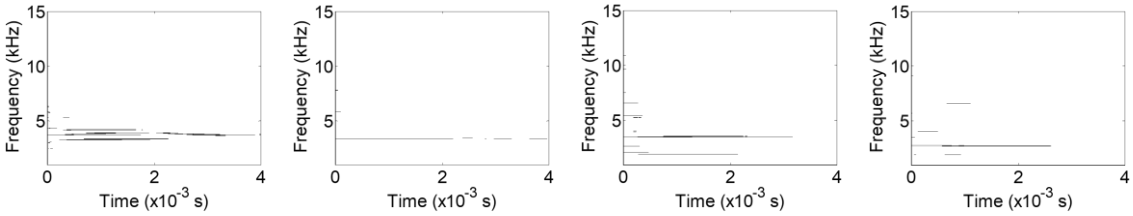

a) Point #11 (b) Point #12 (c) Point #23 (d) Point #35

Figure 4.22. SSAWT scalograms of IE signals with shallow delamination

The identified delamination conditions with the proposed SSAWT at all 40 points are summarized in Table 4.3. Deep delamination (D), no delamination (N), and shallow delamination (S) are successfully detected at all but two points. As such, the proposed

SSAWT proved robust in applications. The two exceptions at Points #7 and #13 give false negative detections. These two points are located near the edge of cardboards, which could be moved during the pouring process of mortar. Moreover, the depths of both deep and no delamination are all determined with high accuracy (<1.5% and <5% in error, respectively). The average of all detected slab thicknesses is 7.21 in. (0.55% in error) with a standard deviation of 0.15 in.

Table 4.3. Identified delamination results at all 40 locations with the proposed SSAWT

Location	**Type**	**Location**	**Type**	**Location**	**Type**	**Location**	**Type**
1	N (7.29 in)	11	S	21	N (7.47 in)	31	N (7.17 in)
2	N (7.20 in)	12	S	22	D (5.21 in)	32	N (7.20 in)
3	N (7.24 in)	13	*N (false)*	23	S	33	N (7.29 in)
4	N (7.12 in)	14	D (6.24 in)	24	N (7.20 in)	34	D (6.34 in)
5	D (6.17 in)	15	S	25	N (7.51 in)	35	S
6	D (6.24 in)	16	S	26	N (7.24 in)	36	N (7.07 in)
7	*N (false)*	17	N (7.03 in)	27	N (7.16 in)	37	N (6.99 in)
8	S	18	N (7.56 in)	28	N (6.95 in)	38	N (7.20 in)
9	D (6.30 in)	19	N (7.20 in)	29	N (7.03 in)	39	N (7.24 in)
10	D (6.24 in)	20	N (7.33 in)	30	N (7.29 in)	40	N (7.07 in)

Note: the delamination depth and slab thickness are given in parenthesis in the case of deep and no delamination.

In comparison with Table 4.2, the proposed SSAWT shown in Table 4.3 enables the determination of slab thickness and the increased accuracy in identification of the deep delamination. This is because the SSAWT gives no-dispersion ridgelines in a time-frequency scalogram so that the key features can be extracted more accurately from the scalogram.

4.4. SUMMARY

In this section, both the proposed AWT and SSAWT are applied to the impact echo responses experimentally recorded from a 60"×36"×7.25" concrete slab. Improvement in time and frequency resolution leads to more successful detections of deep or shallow delamination out of 40 sets of analyzed test data. The selection process of time-varying central frequencies, scaling factors, and window lengths proves robust.

The proposed AWT are robust in the detection of defects (delamination) embedded in a concrete slab from impact echo responses. It can clearly distinguish the unique time and frequency features associated with no delamination, shallow delamination, and deep delamination. Due to mixed frequency characteristics of the three delamination conditions, high time resolution is needed to exclude shallow delamination from the other two, while high frequency resolution is necessary for resonant frequency identification (deep versus no delamination). Out of 40 measurement IE responses, 7 more responses can be used to accurately detect the embedded defects in comparison with conventional wavelet transform. The determined/predicted depth of deep delamination can be determined with an error of less than 3%.

SSAWT showed required robustness and accuracy in the detection of defects (delamination) embedded in a concrete slab from IE responses. For deep and no delamination cases with short time duration, instantaneous frequency spectra were accumulated over time to further improve the identification accuracy. Only two out of 40 measured IE responses led to falsely identified delamination conditions. The two exception locations were on the edge of pre-embedded defects. The detection error was less than 1.5% in deep delamination depth and 5% in slab thickness.

5. MULTIPLE ANALYTICAL MODE DECOMPOSITION

5.1. THE PROPOSED M-AMD ALGORITHM

Consider a weakly nonlinear structural system represented by a SDOF oscillator. Let the mass-normalized time-varying damping coefficient, stiffness coefficient and external force be $2h(t)$, $\omega^2(t)$ and $p(t)$, respectively. The equation of motion for the forced vibration of the nonlinear system can be expressed into:

$$\ddot{x}(t) + 2h(t)\dot{x}(t) + \omega^2(t)x(t) = p(t), \tag{18}$$

in which $x(t)$, $\dot{x}(t)$ and $\ddot{x}(t)$ represent the displacement, velocity, and acceleration of the nonlinear system. Let $2h(t) = 2h_s(t) + 2h_f(t)$ and $\omega^2(t) = \omega_s^2(t) + \omega_f^2(t)$, where the subscripts s and f indicate slow- and fast-varying components of the normalized damping (or stiffness) coefficient with its frequency lower and higher than the narrow frequency band of velocity (or displacement). Equation (18) can then be rewritten as:

$$\ddot{x}(t) + 2h_s(t)\dot{x}(t) + 2h_f(t)\dot{x}(t) + \omega_s^2(t)x(t) + \omega_f^2(t)x(t) = p(t). \tag{19}$$

By applying the Bedrosian theorem [85], the Hilbert transform of Equation (19) gives:

$$H[\ddot{x}(t)] + 2h_s(t)H[\dot{x}(t)] + H\big[2h_f(t)\big]\dot{x}(t) + \omega_s^2(t)H[x(t)] + H[\omega_f^2(t)]x(t) = H[p(t)], \tag{20}$$

where $H[\cdot]$ stands for the Hilbert transform of a function inside the bracket. If the fast-varying components, $2h_f(t)$ and $\omega_f^2(t)$, are neglected [18], Equations (18) and (19) become a pair of simplified equations with new parameters $2h_0$ and ω_0^2 as follows:

$$\begin{cases} \ddot{x} + 2h_0\dot{x} + \omega_0^2 x = p \\ H[\ddot{x}] + 2h_0 H[\dot{x}] + \omega_0^2 H[x] = H[p] \end{cases}. \tag{21}$$

Note that Equation (21) represents an abbreviated form of time functions without explicitly showing the time variable. When displacement, velocity, and acceleration

responses are all or partially known, the solution of Equation (21) for $2h_0$ and ω_0^2 can be expressed into:

$$\begin{cases} \omega_0^2 = \frac{pH[\dot{x}]-H[p]\dot{x}}{xH[\dot{x}]-H[x]\dot{x}} - \frac{\ddot{x}H[\dot{x}]-H[\ddot{x}]\dot{x}}{xH[\dot{x}]-H[x]\dot{x}} = \omega_{0p}^2 + \omega_{0x}^2 \\ 2h_0 = \frac{pH[x]-H[p]x}{H[x]\dot{x}-xH[\dot{x}]} - \frac{\ddot{x}H[x]-H[\ddot{x}]x}{H[x]\dot{x}-xH[\dot{x}]} = 2h_{0p} + 2h_{0x} \end{cases}. \tag{22}$$

They are referred to as the initial instantaneous stiffness and damping coefficients, respectively. The subscript p indicates the stiffness/damping coefficient part that is directly associated with the load function, while the subscript x indicates the coefficient from the system responses only.

5.1.1. Slow-varying Components. When $\omega_f^2 = 0$ and $h_f = 0$, $\omega_s^2 = \omega_0^2$ and $h_s = h_0$ are true. Otherwise, ω_s^2 and h_s are associated with ω_f^2 and h_f based on Equations (19) and (20):

$$\begin{aligned} \omega_s^2 &= \frac{pH[\dot{x}]-H[p]\dot{x}}{xH[\dot{x}]-H[x]\dot{x}} - \frac{\ddot{x}H[\dot{x}]-H[\ddot{x}]\dot{x}}{xH[\dot{x}]-H[x]\dot{x}} - \frac{(2h_fH[\dot{x}]-H[2h_f]\dot{x})\dot{x}}{xH[\dot{x}]-H[x]\dot{x}} - \frac{\left(\omega_f^2H[\dot{x}]-H\left[\omega_f^2\right]\dot{x}\right)x}{xH[\dot{x}]-H[x]\dot{x}} \\ &= \omega_0^2 - f_1(h_f) - f_2(\omega_f^2), \end{aligned} \tag{23}$$

$$\begin{aligned} 2h_s &= \frac{pH[x]-H[p]x}{H[x]\dot{x}-xH[\dot{x}]} - \frac{\ddot{x}H[x]-H[\ddot{x}]x}{H[x]\dot{x}-xH[\dot{x}]} - \frac{(2h_fH[x]-H[2h_f]x)\dot{x}}{H[x]\dot{x}-xH[\dot{x}]} - \frac{\left(\omega_f^2H[x]-H\left[\omega_f^2\right]x\right)x}{H[x]\dot{x}-xH[\dot{x}]} \\ &= 2h_0 - f_3(h_f) - f_4(\omega_f^2). \end{aligned} \tag{24}$$

Equations (23) and (24) can be rewritten as $\omega_0^2 = \omega_s^2 + f_1(h_f) + f_2(\omega_f^2)$ and $2h_0 = 2h_s + f_3(h_f) + f_4(\omega_f^2)$. These relationships indicate that the fast-varying damping and stiffness coefficients both affect ω_0^2 or $2h_0$, and both of them are essentially distorted with mixed from part of the fast-varying components. Therefore, the initial instantaneous parameters in Equation (22) are distorted from a mechanical/physical point of view, and AMDs have to be implemented. The effect of ω_{0p}^2 and $2h_{0p}$ can be lumped into the slow-varying stiffness and damping coefficients as follows:

$$\begin{cases}\omega_{0x}^2 = \omega_0^2 - \omega_{0p}^2 = \omega_{s'}^2 - \omega_{0p}^2 + f_1(h_f) + f_2(\omega_f^2) = \omega_{s'}^2 + f_1(h_f) + f_2(\omega_f^2) \\ 2h_{0x} = 2h_0 - 2h_{0p} = 2h_{s'} - 2h_{0p} + f_3(h_f) + f_4(\omega_f^2) = 2h_{s'} + f_3(h_f) + f_4(\omega_f^2)\end{cases}. \quad (25)$$

Let the remaining low-frequency and the removed high-frequency components of a general signal $s(t)$ with a time-varying bisecting frequency of $\omega_b(t)$ be $AMD_{\omega_b(t)}\{s(t)\}$ and $\overline{AMD}_{\omega_b(t)}\{s(t)\}$, respectively [2]. The bisecting frequencies between the slow- and fast-varying stiffness components can be determined by the wavelet analysis of ω_{0x}^2 as denoted by $\omega_{x1}(t)$ between $\omega_{s'}^2$ and $f_1(h_f)$ and $\omega_{x2}(t)$ between $\omega_{s'}^2$ and $f_2(\omega_f^2)$, respectively. Similarly, the bisecting frequencies $\omega_{\dot{x}1}(t)$ between $2h_{s'}$ and $f_3(h_f)$ and $\omega_{\dot{x}2}(t)$ between $2h_{s'}$ and $f_4(\omega_f^2)$ are determined from the wavelet analysis of $2h_{0x}$. Therefore, AMDs are applied for the first time to determine the modified slow-varying components of stiffness and damping coefficients:

$$\omega_{s'}^2 = AMD_{\min[\omega_{x1}(t),\omega_{x2}(t)]}\{\omega_{0x}^2(t)\}, \quad (26)$$

$$2h_{s'} = AMD_{\min[\omega_{\dot{x}1}(t),\omega_{\dot{x}2}(t)]}\{2h_{0x}(t)\}. \quad (27)$$

The actual slow-varying components can thus be obtained as $\omega_s^2 = \omega_{s'}^2 + \omega_{0p}^2$ and $2h_s = 2h_{s'} + 2h_{0p}$.

5.1.2. Fast-varying Components. When the dominant frequency band of the fast-varying component of damping coefficient is lower than that of stiffness coefficient and they are separated by a bisecting frequency, $\omega_b'(t)$, the fast-varying damping coefficient can be identified first. In this case, AMDs can be applied for the second time to determine:

$$2h_f = AMD_{\omega_b'(t)}\{2\tilde{h}_f\}, \quad (28)$$

in which $\tilde{h}_f$ is obtained from:

$$2\tilde{h}_f = \begin{cases}\frac{p-(\ddot{x}+2h_s\dot{x}+\omega^2 x)}{\dot{x}}, & \text{when } \dot{x} \neq 0 \\ \frac{\dot{p}-(\dddot{x}+2h_s\ddot{x}+\dot{\omega}^2 x)}{\ddot{x}}, & \text{when } \dot{x} = 0\end{cases}. \quad (29)$$

Then, the total damping coefficient is $2h = 2h_s + 2h_f$, and the fast-varying component of stiffness coefficient can be determined by:

$$\omega_f^2 = \begin{cases} \frac{p-(\ddot{x}+2h\dot{x}+\omega_s^2 x)}{x}, & \text{when } x \neq 0 \\ \frac{\dot{p}-(\dddot{x}+2h\ddot{x}+2\dot{h}\dot{x}+\omega_s^2\dot{x})}{\dot{x}}, & \text{when } x = 0 \end{cases}. \tag{30}$$

In Equation (29), $\tilde{h}_f$ is directly derived from Equation (18) when $\dot{x} \neq 0$, and derived from the differentiation of both sides of Equation (18) when $\dot{x} = 0$. Since $2\tilde{h}_f$ is associated with ω_f^2 in Equation (29), AMD is applied in Equation (28).

When the dominant frequency band of the fast-varying component of stiffness coefficient is lower than that of damping coefficient, and they are separated by a bisecting frequency, $\omega_b'(t)$, the fast-varying stiffness coefficient can be identified first from:

$$\omega_f^2 = AMD_{\omega_b'(t)}\{\widetilde{\omega}_f^2\}, \tag{31}$$

in which $\widetilde{\omega}_f^2$ is determined by:

$$\widetilde{\omega}_f^2 = \begin{cases} \frac{p-(\ddot{x}+2h\dot{x}+\omega_s^2 x)}{x}, & \text{when } x \neq 0 \\ \frac{\dot{p}-(\dddot{x}+2h\ddot{x}+2\dot{h}\dot{x}+\omega_s^2\dot{x})}{\dot{x}}, & \text{when } x = 0 \end{cases}. \tag{32}$$

With a total stiffness coefficient of $\omega^2 = \omega_s^2 + \omega_f^2$, the fast-varying damping coefficient can be determined by:

$$2h_f = \begin{cases} \frac{p-(\ddot{x}+2h_s\dot{x}+\omega^2 x)}{\dot{x}}, & \text{when } \dot{x} \neq 0 \\ \frac{\dot{p}-(\dddot{x}+2h_s\ddot{x}+\dot{\omega}^2 x)}{\ddot{x}}, & \text{when } \dot{x} = 0 \end{cases}. \tag{33}$$

As a special case, most nonlinear systems in engineering applications include either fast-varying stiffness or damping coefficient only. In this case, $2h(t) = 2h_s(t) + 2h_f(t)$ when the fast-varying damping coefficient is present, and $\omega^2(t) = \omega_s^2(t) + \omega_f^2(t)$ when the fast-varying stiffness coefficient is present. The fast-varying components, $\omega_f^2(t)$ and $2h_f(t)$, are obtained from Equations (30) and (33), respectively.

5.2. PARAMETRIC IDENTIFICATION BASED ON FREE VIBRATION

In order to demonstrate the effectiveness of the proposed M-AMD algorithm, three numerical examples based on free vibration are presented in this section.

5.2.1. Duffing Oscillator. To illustrate how significant the fast-varying component of stiffness coefficient can be in dynamic characteristics, the free vibration of a classical Duffing oscillator with a unit mass was analyzed. The equation of motion was expressed into: $\ddot{x}(t) + 2h\dot{x}(t) + x(t) + \alpha x^3(t) = 0$. Let $2h = 0.05\ \mathrm{s}^{-1}$ and $\alpha = 0.02\ \mathrm{mm}^{-2}\mathrm{s}^{-2}$. Under an initial displacement $x(0) = 10$ mm and an initial velocity $\dot{x}(0) = 0$ mm/s, the displacement response sampled at 5 Hz is presented in Figure 5.1(a). The theoretic time-varying stiffness coefficient can be written as $\omega^2(t) = (1 + 0.02x^2)$ as shown in Figure 5.1(b).

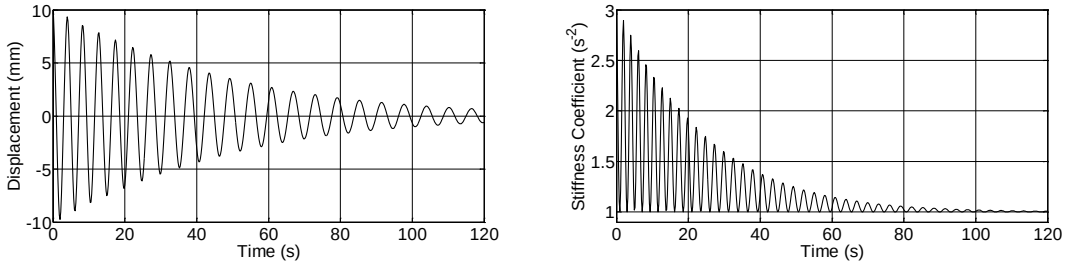

(a) Displacement time history (b) Theoretic stiffness coefficient

Figure 5.1. Responses of a Duffing oscillator

In this example, the damping coefficient is constant or the fast-varying damping component is equal to zero. To estimate the bisecting frequency $\omega_{x2}(t)$, the wavelet scalograms of $\omega_0^2(t)$ and $x(t)$ are presented in Figure 5.2. The wavelet scalogram of $x(t)$ is in general agreement with the instantaneous frequency directly extracted by Hilbert transform but unable to identify the fast-varying details over time. The identified stiffness

using Equation (22), $\omega_0^2(t)$, has slow- and fast-varying components. The frequency of the slow-varying component or constant stiffness in this example is not shown in Figure 5.2 for clarity. The frequency of the fast-varying component is higher than the instantaneous frequency extracted from the Hilbert spectrum. In this case, the bisecting frequency $\omega_{x2}(t)$ can be determined along the centerline of the instantaneous frequency of $x(t)$ in order to identify $\omega_s^2(t)$ and $\omega_f^2(t)$.

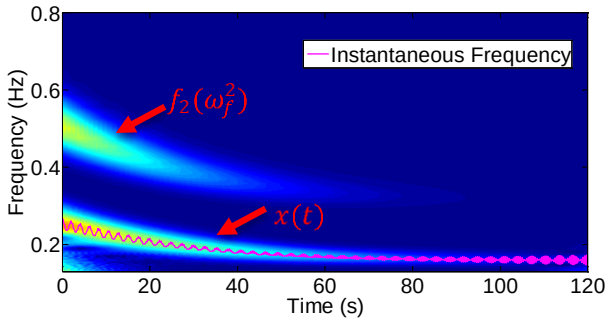

Figure 5.2. Wavelet scalogram of the fast-varying component of $\omega_0^2(t)$ and $x(t)$

With the AMD of ω_0^2(t) using the bisecting frequency $\omega_{x2}(t)$, the slow-varying stiffness of the oscillator is presented in green dashed line as shown in Figure 5.3, representing the filtered $\omega_0^2(t)$. As clearly indicated in Figure 5.3, the slow-varying stiffness is quite different from its theoretic value. Therefore, the fast-varying stiffness component must be taken into account in the identification of stiffness.

The stiffness coefficient determined from Equations (25) and (29) is presented in red dot-dashed line in Figure 5.4(a) and compared with the theoretic stiffness coefficient. The proposed solution has accurately incorporated the high frequency components of stiffness coefficient, resulting in an excellent agreement with the theoretic value. Note that the high fluctuation of the identified stiffness is closely related to the displacement

amplitude as shown in Figure 5.1(a). The smaller the response amplitude is, the less the stiffness fluctuates, since the oscillator behaves more like a linear system with a constant stiffness coefficient.

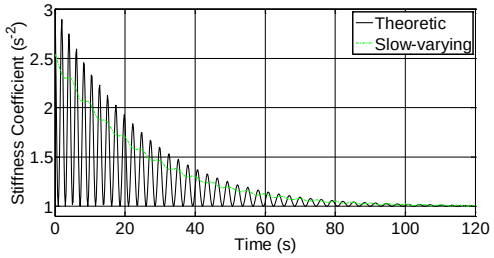

Figure 5.3. Filtered $\omega_0^2(t)$ for the slow-varying component of stiffness coefficient

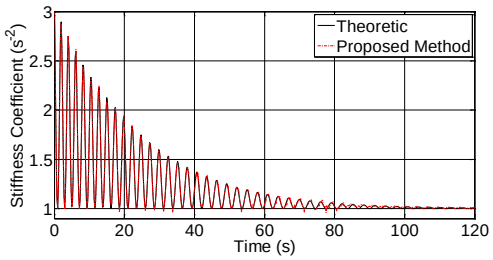

(a) Theoretic vs. proposed method

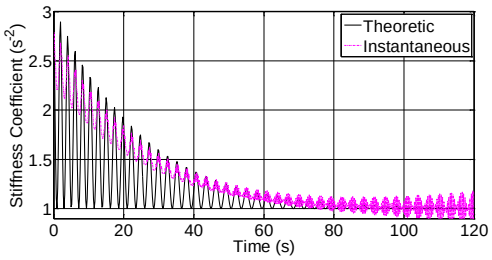

(b) Theoretic vs. instantaneous stiffness coefficient

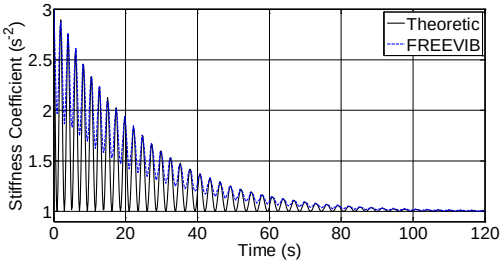

(c) Theoretic vs. FREEVIB stiffness coefficient

Figure 5.4. Time-varying stiffness coefficients

To demonstrate the advantage of the proposed method over other methods, the instantaneous stiffness coefficient of displacement response, $x(t)$, was determined from its Hilbert spectrum and compared with the theoretic stiffness coefficient as shown in Figure 5.4(b). It can be clearly seen from Figure 5.4(b) that the extracted peak instantaneous

stiffness was underestimated prior to 60 s and overestimated after 60 s. Due to numerical instability, the instantaneous stiffness diverged from the asymptotic stiffness of the corresponding linear system at low response amplitudes (< 2.5 mm) after 60 s. The stiffness of the oscillator was also identified using the FREEVIB method as presented in Figure 5.4(c). Although improving over the Hilbert spectral analysis by taking part of the fast-varying component into account, the FREEVIB method gave results that remained quite different from the theoretic stiffness. In comparison with the instantaneous stiffness and the FREEVIB solution, the proposed solution can accurately identify the stiffness of the Duffing system.

To quantify the advantage of the proposed method over the Hilbert spectral analysis and the FREEVIB method, the overall error between the identified value (ID) and its corresponding theoretic value (TH) over a time duration [0, T] is defined by:

$$Error = \frac{\sqrt{\int_0^T (ID-TH)^2 dt}}{\sqrt{\int_0^T (TH)^2 dt}} \times 100\%. \tag{34}$$

In this example, the error in Equation (34) is calculated for the estimation of stiffness coefficient. Figures 5.5(a)-5.5(c) present and compare the errors of three methods as a function of α when the initial displacement is set to 10 mm, 7.5 mm, and 5.0 mm, respectively. Since the changes of the errors with α in Figures 5.5(a)-5.5(c) are similar, Figure 5.5(a) is taken as an example for analysis. When $\alpha = 0.02\ \mathrm{mm^{-2}s^{-2}}$ as discussed in Figure 5.4, the overall error in estimation of the stiffness coefficient within the 120 s is 20.0% with the Hilbert spectral analysis, 16.4% with the FREEVIB method, and 1.2% with the proposed M-AMD method. As α increases, the proposed method continues to give significantly more accurate results than the other two methods and approaches to a

consistent accuracy at low displacement responses. When $\alpha > 2.5\ \mathrm{mm^{-2}s^{-2}}$, the errors of the Hilbert spectral analysis and the FREEVIB method change with α and is thus less predictable in applications.

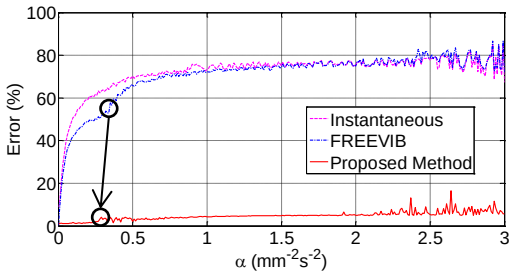

(a) 10 mm initial displacement

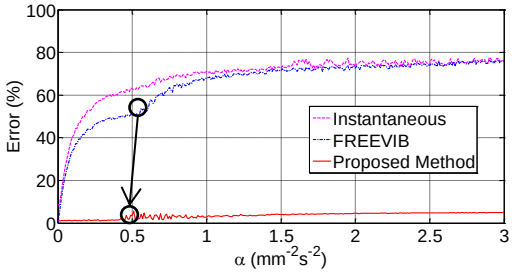

(b) 7.5 mm initial displacement

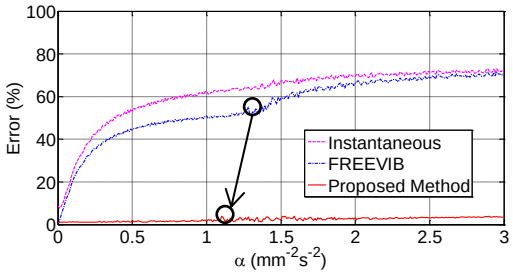

(c) 5 mm initial displacement

Figure 5.5. Overall errors as a function of system nonlinearity

Figures 5.5(a)-5.5(c) clearly indicate a characteristic α value where the error of the FREEVIB method suddenly increases for all three initial conditions. Correspondingly, the error of the proposed method increases at $\alpha = 0.26, 0.44, \text{and } 1.08\ \mathrm{mm^{-2}s^{-2}}$ when $x(0) = 10, 7.5, \text{and } 5.0\ \mathrm{mm}$, respectively. The three sets of characteristic parameters

correspond to $\lambda = \alpha x^2(0)/1.0 = 26, 25, \text{and } 27,$ respectively. Note that the $1.0\ \text{s}^{-2}$ represents the coefficient of $x(t)$ term in the equation of motion. Here, λ represents the ratio between the nonlinear and linear terms of the restoring force in the Duffing oscillator, which is referred to as the degree of nonlinearity. Therefore, the error of the proposed method is below 2% when the degree of nonlinear is less than approximately 25.

5.2.2. Bouc-Wen Hysteretic Model. The Bouc-Wen model has been widely used in civil engineering to model the response and behavior of various structural components. The free vibration of a SDOF Bouc-Wen model can be determined from Equation (35):

$$m\ddot{u}(t) + c\dot{u}(t) + \alpha k_0 u(t) + (1-\alpha)k_0 z(t) = 0 \tag{35}$$

where m and c denote the mass and damping coefficient of the model; $u(t)$, $\dot{u}(t)$, and $\ddot{u}(t)$ are the displacement, velocity, and acceleration of the model; k_0 represents the pre-yield stiffness; $\alpha = k_y/k_0$ represents the ratio of post-yield to pre-yield stiffness; and $z(t)$ is a non-observable hysteretic displacement with an initial condition of $z(0) = 0$. The hysteretic displacement satisfies the following relation:

$$\dot{z}(t) = \dot{u}\{A - [\beta sign(\dot{u}z) + \gamma]|z|^n\} \tag{36}$$

where A, β, γ, and n are dimensionless parameters controlling the behavior of the model, and $sign(\cdot)$ is a sign function. These parameters are functionally redundant. To remove the redundancy, A and $\beta + \gamma$ are best fixed to unity for lead-rubber bearings [86, 87].

To facilitate the identification process of model parameters with the proposed method, a derivative is taken of Equation (35), $\dot{u}(t)$ is replaced with $x_1(t)$, and Equation (36) is introduced so that Equation (35) becomes:

$$m\ddot{x}_1(t) + c\dot{x}_1(t) + \alpha k_0 x_1(t) + (1-\alpha)k_0\{A - [\beta sign(x_1 z) + \gamma]|z|^n\}x_1(t) = 0. \tag{37}$$

When $A = 1$ [86], Equation (37) can be normalized by mass and further simplified into:

$$\ddot{x}_1(t) + 2h\dot{x}_1(t) + \omega^2(t)x_1(t) = 0. \quad (38)$$

Equation (38) is very similar to the Duffing oscillator studied above. The proposed method can now be applied into parametric identification of the new system in terms of $x_1(t)$. Here, $2h = c/m$ and $\omega_s^2 = k_0/m$ are constant while $\omega^2(t) = \omega_s^2\{1 - (1 - \alpha)[\beta sign(x_1 z) + \gamma]|z|^n\}$ changes with time. In this case, the fast-varying component of stiffness comes from the time-varying term $(1 - \alpha)[\beta sign(x_1 z) + \gamma]|z|^n$. After $2h_0$ and ω_0^2 have been determined using Equation (22), AMD is utilized to filter out the fast-varying component of ω_0^2 so that the remaining slow-varying component is identified to be ω_s^2.

When $2h = 2h_0 = c/m$ and ω_s^2 are known, the restoring force can be obtained as $F(t) = m[\alpha\omega_s^2 u(t) + (1 - \alpha)\omega_s^2 z(t)] = m[-\dot{x}_1(t) - 2hx_1(t)]$ from which (hysteresis loop) α can be identified and calculated as the ratio of post-yield and pre-yield stiffness. Then, $\dot{z}(t)$ can be determined from $x_1(t)$ and its derivatives by:

$$\dot{z}(t) = \frac{\ddot{x}_1(t) + 2h\dot{x}_1(t) + \alpha\omega_s^2 x_1(t)}{(1-\alpha)\omega_s^2}. \quad (39)$$

With the initial condition of $z(0) = 0$, $z(t)$ can be obtained from integration. With known $z(t)$ and $\dot{z}(t)$, the parameters β and n can be determined as follows. When $x_1 z$ is positive, Equation (36) is simplified into $\dot{z}(t) = x_1(1 - |z|^n)$ from which n can be determined at each segment corresponding to $sign(x_1 z) = 1$. The final n value can be obtained by averaging the identified values at all the segments. When $x_1 z$ is negative, $\dot{z}(t) = x_1[1 - (1 - 2\beta)|z|^n]$ from which β can be solved with all other known parameters in the same way as for the identification of n.

To illustrate the above parameter identification process, an example Bouc-Wen model of lead-rubber bearing is considered with its theoretic parameters chosen as: $m =$ 7,000 kg, $c = 3.5$ kN·s/m, $k_0 = 210$ kN/m, $\alpha = 0.1$, $\beta = 0.5$, $\gamma = 1 - \beta = 0.5$, $n = 2$,

and a yielding displacement (u_y) of 50 mm. The theoretic hysteresis is shown in Figure 5.6 with the initial conditions of $u(0) = -0.5$ m and $\dot{u}(0) = 2$ m/s. The displacement time history $u(t)$ is considered to be given. Its first derivative $x_1(t)$ and high-order derivatives are calculated numerically.

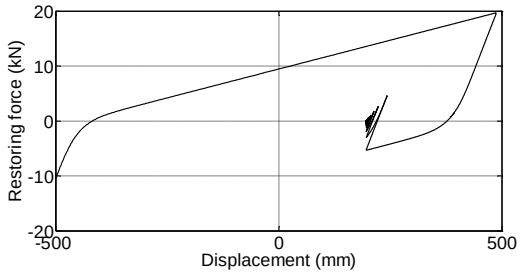

Figure 5.6. Theoretic hysteresis loop of the Bouc-Wen system

By applying the proposed method, the damping coefficient $2h = c/m = 0.496 - 0.522$ s^{-1} with an average of 0.505 s^{-1} and the stiffness coefficient $\omega_s^2 = k_0/m = 29.8 - 30.1$ s^{-2} with an average of 30.0 s^{-2} were obtained as shown in Figure 5.7 after the fast-varying component of ω_0^2 had been filtered out with AMD. Their corresponding errors were evaluated from Equation (34) to be 0.18% and 0.29%, respectively. It can be clearly seen from Figure 5.7 that the proposed method resulted in two accurate identifications over time, while the FREEVIB method led to erroneous results and was thus no longer considered in the following analysis, which is caused by the accumulated error from the previous step. At this stage, M-AMD is still able to continue the analysis, and the advantage has already been demonstrated over FREEVIB.

Let $2h = 0.50\ s^{-1}$. The hysteresis loop can be evaluated from $F(t) = -m[\dot{x}_1(t) + 0.50x_1(t)]$ in which k_0 and k_y were identified to be 210 kN/m and 21 kN/m as illustrated from the red tangential lines in Figure 5.8. Therefore, $\alpha = k_y/k_0 = 0.1$,

which agrees well with its theoretic value. At this stage, the hysteretic behavior of the Bouc-Wen system is identified with good accuracy, and the following procedure is able to proceed with enough confidence.

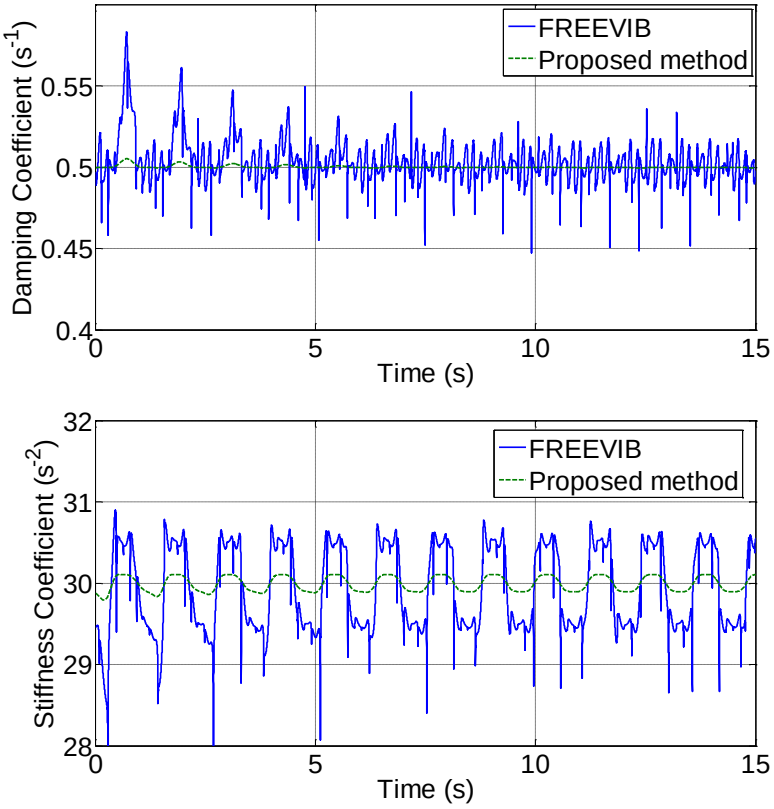

Figure 5.7. Identified $2h$ and ω_s^2 with the proposed and FREEVIB methods

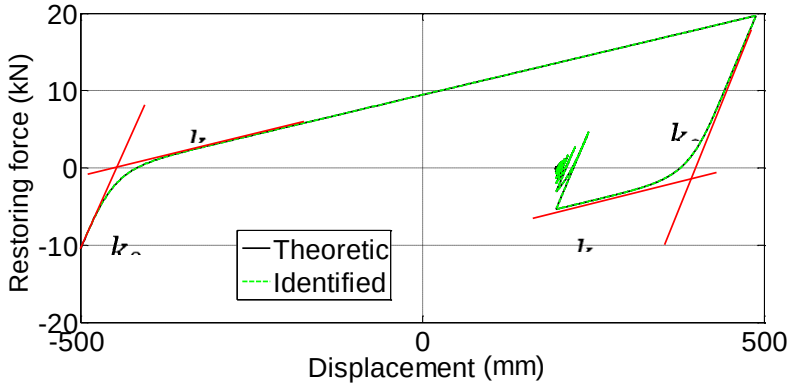

Figure 5.8. Identification of parameter α

Prior to the determination of last three parameters, Equation (39) was used to obtain $\dot{z}(t)$, which was further integrated over time to obtain $z(t)$ with an initial condition of $z(0) = 0$. The calculated $\dot{z}(t)$ and $z(t)$ are plotted in Figure 5.9 as a function of time, which are in excellent agreement with their theoretic values.

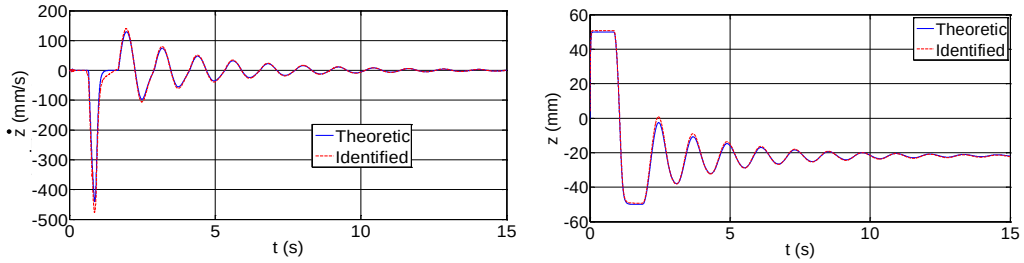

Figure 5.9. Calculated $\dot{z}(t)$ and $z(t)$

The parameter $n = 1.95 - 2.01$ as shown in Figure 5.10(a) was calculated at each time instant when the product of $x_1 z$ was positive. The average of all the n values over time was $n = 1.99$. Similarly, $\beta = 0.48 - 0.52$ with an average of 0.50 was obtained from the time when $x_1 z$ was negative as shown in Figure 5.10(b). Finally, $\gamma = 1 - \beta = 0.5$.

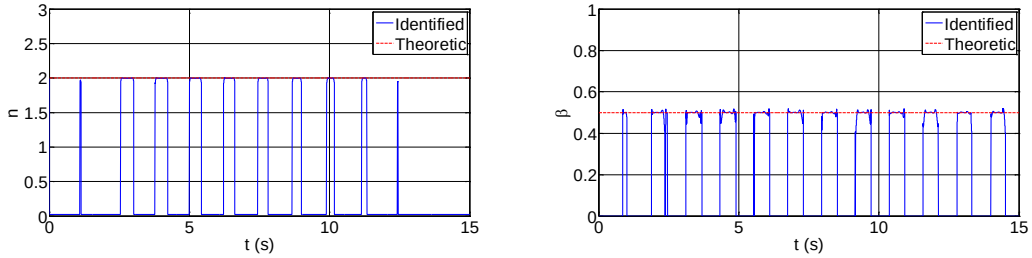

(a) n estimation (b) β estimation

Figure 5.10**.** Identification of parameters n and β

5.2.3. Spherical Bearing. When a block slides along a spherical bearing surface, the equation of motion can be expressed into:

$$m\ddot{x}(t) + c\dot{x}(t) + k_1 x(t) + k_2 sgn[\dot{x}(t)] = 0 \quad (40)$$

where stiffness $k_1 = mg/R$ represents the ratio between the weight (mg) and the radius (R) of bearing, $k_2 = \mu mg$ is the friction force that is the product of the coefficient of friction (μ) and the weight, and g is the gravitational acceleration. When $\dot{x}(t) \neq 0$, Equation (40) can be rewritten as:

$$\ddot{x}(t) + \left[\frac{c}{m} + \frac{\mu g}{|\dot{x}(t)|}\right]\dot{x}(t) + \frac{g}{R}x(t) = 0. \quad (41)$$

In this case, there exists a fast-varying component $|\dot{x}(t)|$ that includes frequencies higher than those of the velocity due to the imposed operation of modulus. Therefore, Equation (21) alone does not lead to accurate (correct) identification of all the parameters of spherical bearing. The proposed method must be used to determine the parameters of the bearing with high accuracy.

Consider a block system with spherical bearing: $g = 10$ m/s^2, $R = 0.5$ m, $\mu = 0.01$, $c = 15$ kg/s, and $m = 100$ kg. The system was subjected to initial conditions: $\dot{x}(0) = 0.3$ m/s and $x(0) = -0.2$ m. Following the proposed method, the slow-varying stiffness coefficient is directly related to R. The slow- and fast-varying damping coefficients are related to c/m and μ, respectively. Figure 5.11(a) shows the slow-varying stiffness coefficient from which $g/R = 19.96 - 20.08$ s^{-2} with an average of 20.01 s^{-2} was identified with high accuracy. The average R value over the time duration was $R = 0.5$ m. Similarly, $c/m = 0.142 - 0.159$ s^{-1} with an average of 0.150 s^{-1} was identified as shown in Figure 5.11(b). The system parameters were also identified from the FREEVIB method as shown in Figure 5.10. The FREEVIB method introduced a substantially higher error than the proposed method, and therefore the proposed M-AMD is again proved to be advantageous.

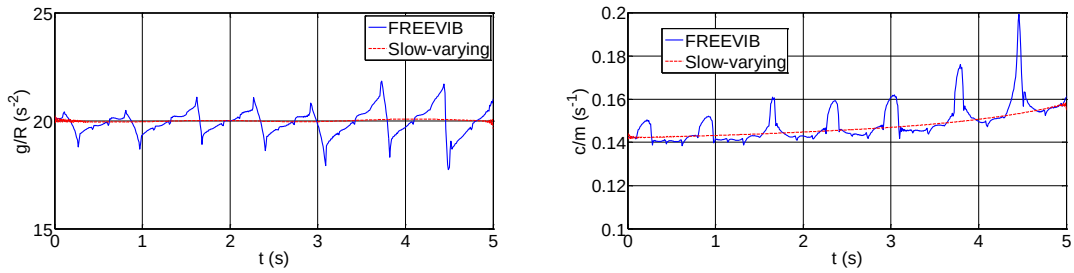

(a) g/R (b) c/m

Figure 5.11. Identified slow-varying parameters

Equation (33) was utilized to obtain the last unknown parameter μ. As shown in Figure 5.12(a), the identified value of $g\mu$ is 0.095-0.102 $\mathrm{m/s^2}$ with an average of 0.099 $\mathrm{m/s^2}$, which differs from its theoretic value (0.1 $\mathrm{m/s^2}$) by 0.2%. The error of identified $g\mu$ was evaluated and presented in Figure 5.12(b) when $\dot{x}(0) = 0.3$ and 0.6 $\mathrm{m/s}$. The errors with both initial conditions are below 10% over a practical range of μ. The errors are less than 1.2% when $\mu < 0.017$. In this case, the FREEVIB method fails to identify μ because it involves the fast-varying component of damping coefficient. The errors of g/R and c/m were also obtained for the proposed method. They are 1.2% and 2.3%.

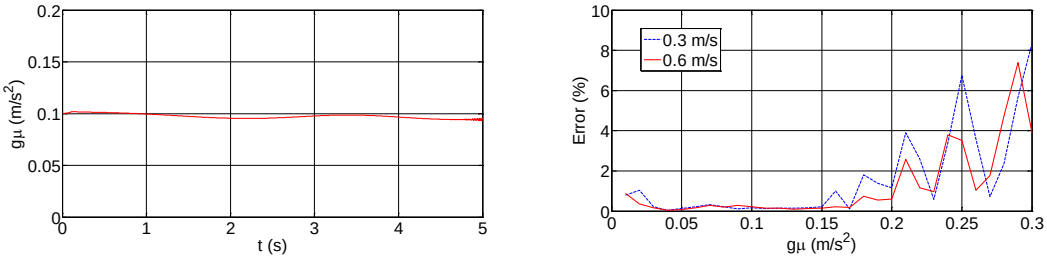

(a) Identified $g\mu$ given in the example (b) Error develop with different μ

Figure 5.12. Identified parameter of $g\mu$ from the proposed method

5.2.4. Robustness of the Proposed Method to Deal with Noise. With the introduction of multiple adaptive low-pass filters (AMDs), the proposed method inherently

contains a noise-reduction ability with noise components above the bisecting frequency filtered out clearly. Without any loss of generality, the effect of noises on the effectiveness and accuracy of the proposed method is demonstrated without and with filtering of the raw displacement data.

Consider the Duffing oscillator with $2h = 0.05\ \mathrm{s}^{-1}$ and $\alpha = 0.02\ (\mathrm{mm}^{-2}\mathrm{s}^{-2})$ at rest under an initial displacement of $x_0 = 10$ mm. The displacement response as presented in Figure 5.1(a) was contaminated with a Gaussian white noise with a root-mean-squared (RMS) displacement of 0.01 mm. Figure 5.13(a, b) compares the two stiffness coefficients obtained from the FREEVIB and the proposed method. It can be seen from Figure 5.13(a, b) that the accuracy of stiffness coefficients identified from both methods is reduced as the displacement decreases. However, the error associated with the proposed method is significantly smaller than that with the FREEVIB at all times. The improved accuracy in parameter identification with the proposed method is mainly due to the noise-reduction filtering ability in AMDs. Furthermore, the identified stiffness coefficient from the proposed method is actually very accurate within 45 s. If AMD is also employed to cleanse the raw displacement data prior to the application of the proposed method, the identification results expect to be more accurate due to less accumulative noise effects [2]. Equation (34) was used again to evaluate the errors of the FREEVIB method and the proposed method without the pre-filtering of AMD. As shown in Figure 5.13(c), the proposed method is still much more accurate than the FREEVIB method as the noise level increases although the low signal-to-noise ratio introduced a significant distortion to the identified results at low displacement amplitudes as demonstrated in Figure 5.13(b) in the case of RMS=0.01 mm.

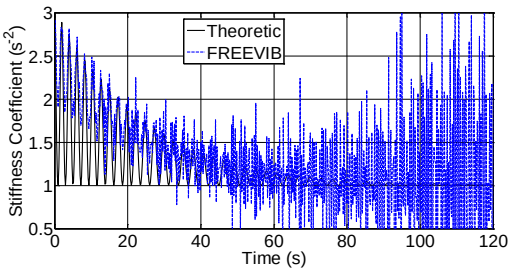

(a) FREEVIB method (RMS=0.01 mm)

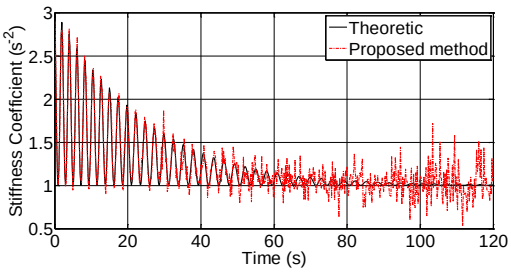

(b) The proposed method (RMS=0.01 mm)

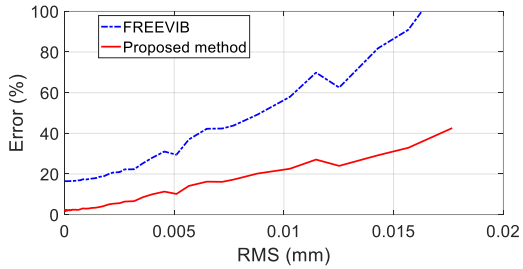

(c) Error development with RMS

Figure 5.13. Effect of noise on the identified stiffness coefficient

Figure 5.14 shows the identified c/m and k_0/m of the Bouc-Wen model when the Gaussian white noise is added into the displacement data. Due to the adaptive filtering ability of AMD, the noise had little effect on the identified parameters. For example, c/m remains in the range of 0.44-0.55 s^{-1} averaged at 0.51 s^{-1}. and k_0/m is between 29.4 and 31.6 s^{-2} with an average value of 30.5 s^{-2}. The calculated errors of the two identified parameters are 4.8% and 6.1%, respectively. In fact, the solutions with the proposed method were stable and accurate in comparison with their theoretic values. However, the solutions with the FREEVIB identification were distorted as expected and became unstable over time as the displacement decreased. In general, the implementation of AMD has overcome such drawback to certain extent.

However, the noise contaminated data makes the identification of α uncertain and nearly impossible since no filter has been utilized up to this point and the noise contaminated displacement data are involved in calculation of the hysteresis loop as

illustrated in Figure 5.15(a). In this case, AMD is required to cleanse the response data, as shown in Figure 5.15(b), from which the cleansed hysteresis loop agrees well with the theoretic loop and α = 0.091 is calculated with 9% in error.

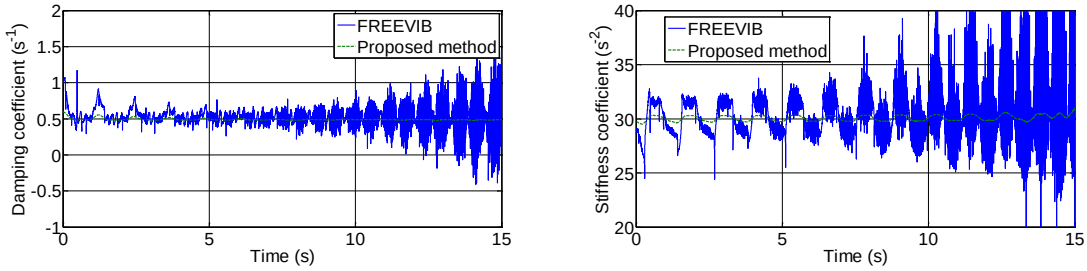

Figure 5.14. Identification of c/m and k_0/m (RMS=0.005 m)

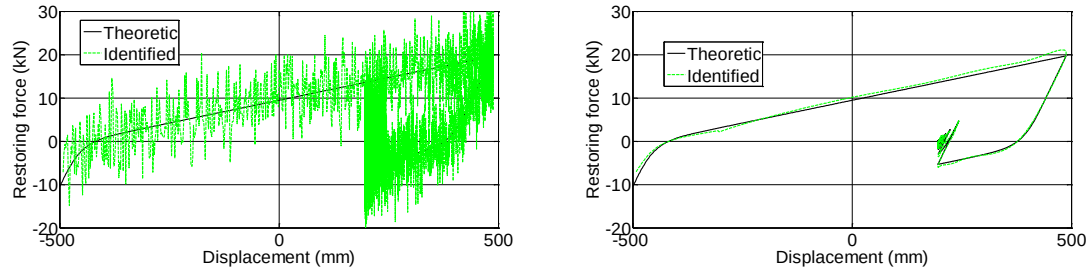

(a) Identification without AMD (b) Identification with AMD

Figure 5.15. Hysteresis loop of Bouc-Wen model (RMS=0.005 m)

The parameters g/R and c/m of the spherical bearing model can also be identified with the proposed method from noise contaminated data. As shown in Figure 5.16, $g/R = 18.8 - 21.8\ \mathrm{s}^{-2}$ with an average of 20.2 s^{-2} was obtained over the entire time duration. The R value was $0.46 - 0.53$ m with an average over time of 0.495 m, which differs from its theoretic value by 7.9% according to Equation (34). Similarly, c/m was identified to be 0.146-0.155 s^{-1} with an average value of 0.149 s^{-1}, which differs from its theoretic value by 4.7% over the time duration. The difference is with 10%, which indicates that the identified results is in good agreement

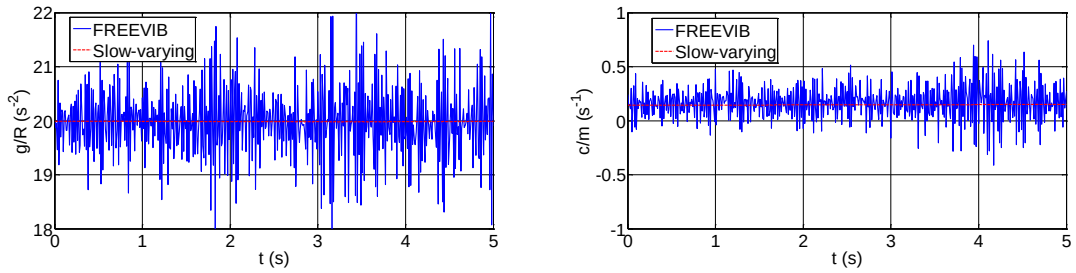

(a) g/R (b) c/m

Figure 5.16. Identification of R and c/m in the spherical bearing model

However, the presence of noise significantly reduces the ability to identify μ in the spherical bearing model, as indicated in Figure 5.17. In this case, AMD can be utilized to filter out the noise before the proposed method is applied. With the introduction of the AMD, $g\mu$ was identified to be 0.092-0.109 s^2 with an overall error of 8.7% over the time duration.

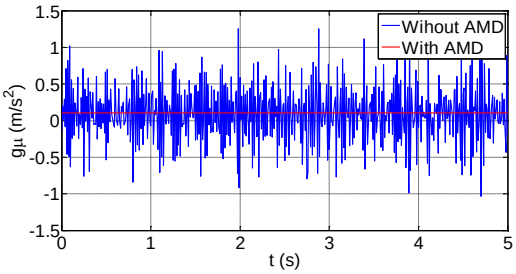

Figure 5.17. Comparison of identified $g\mu$ with and without AMD (RMS=0.0001 m)

5.3. PARAMETRIC IDENTIFICATION UNDER FORCED VIBRATION

In this section, parametric identification of a numerical duffing oscillator model and 1/4-scale building model is performed under forced vibration, in order to complete the M-AMD algorithm.

5.3.1. Duffing Oscillator. The forced vibration of a Duffing oscillator with a unit mass is presented to demonstrate the nonlinear system response with a fast-varying component of stiffness coefficient under a harmonic load. The equation of motion is

expressed into: $\ddot{x}(t) + 2h\dot{x}(t) + \alpha x(t) + \beta x^3(t) = p(t)$, with $2h = 1\ \mathrm{s}^{-1}$, $\alpha = \pi^2\ \mathrm{s}^{-2}$and $\beta = 1000\ \mathrm{mm}^{-2}\mathrm{s}^{-2}$. From the initial displacement and velocity of $x_0 = 0$mm and $\dot{x}_0 = 0$ mm/s, the displacement response under an excitation of $3cos(\pi t)$ mm/s^2 is sampled at 10 Hz as shown in Figure 5.18.

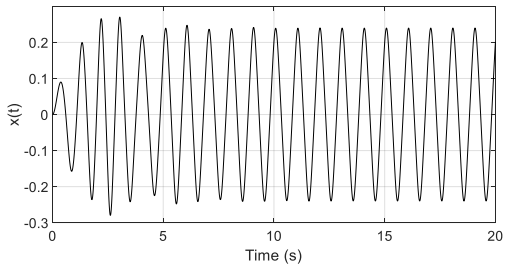

Figure 5.18. Displacement responses of a Duffing oscillator

The initial stiffness coefficient $\omega_0^2(\mathrm{t})$ and the theoretic time-varying stiffness coefficient, $\omega^2(t) = (\pi^2 + 1000x^2)$, are compared in Figure 5.19. Due to the distribution of the fast-varying component of $\omega^2(t)$ into $\omega_0^2(\mathrm{t})$ and $2h_0$, $\omega_0^2(\mathrm{t})$ is distorted and significantly different from the theoretic value.

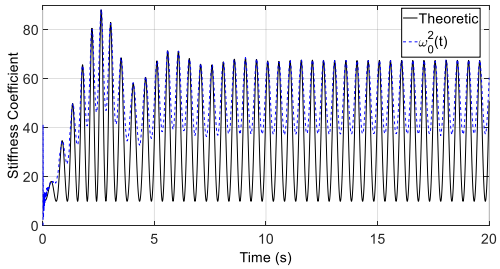

Figure 5.19. Comparison of $\omega_0^2(t)$ and the theoretic stiffness coefficient

After the AMD of $\omega_0^2(\mathrm{t})$ and $2h_0$ have been performed, the slow-varying features of the oscillator are presented in Figure 5.20. The filtered $\omega_0^2(\mathrm{t})$ gives the slow-varying

stiffness coefficient, which totally differs from the theoretic value as presented in Figure 5.19. The filtered $2h_0$ is in excellent agreement with the theoretic value of 1.0 except at the beginning of time history due to the effect of transient vibration. This is true even though the initial damping coefficient is oscillating around the theoretic value substantially. Since the theoretic value of $2h(t)$ is constant, $2h_s(t) = 1\ \mathrm{s}^{-1}$ is the actual value of $2h$ and there is no fast-varying component of damping coefficient.

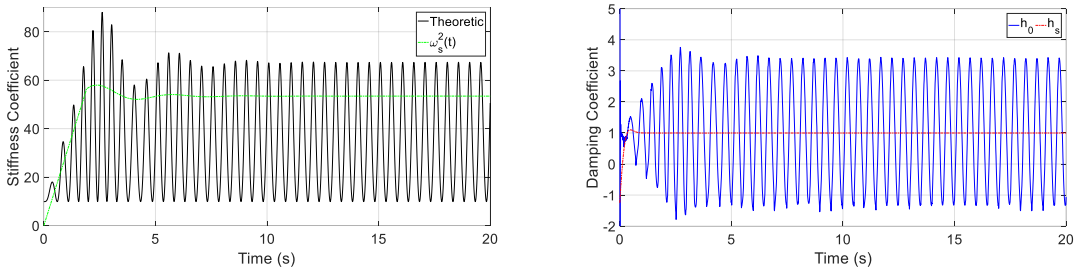

Figure 5.20. Initial $\omega_0^2(\mathrm{t})$ and $2h_0(\mathrm{t})$ versus slow-varying $\omega_s^2(t)$ and $2h_s(t)$ stiffness and damping coefficients

Since no fast-varying component of damping coefficient is present, Equation (30) was used to determine the fast-varying component of stiffness coefficient. The obtained fast-varying component and the slow-varying component were combined as shown in red dot-dashed line in Figure 5.21(a). It can be clearly observed from Figure 5.21(a) that the proposed solution has successfully incorporated the high frequency component and is in nearly perfect match with the theoretic value after 2 s with an error of 3%. To demonstrate the effectiveness of the proposed method over Hilbert spectral analysis, the instantaneous stiffness coefficient was also determined from the Hilbert spectrum of displacement response, $x(t)$ and compared with the theoretic stiffness coefficient as shown in Figure 5.21(b). It can be clearly seen from Figure 5.21(b) that the extracted instantaneous stiffness

from the Hilbert spectral analysis is quite different from the theoretic value, which is generally true for nonlinear systems [17, 18].

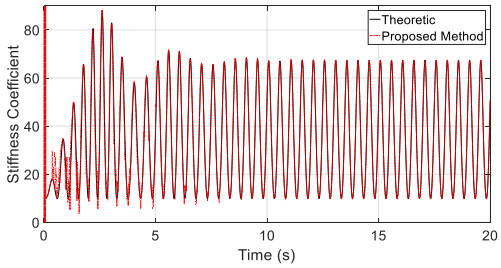

(a) Proposed vs. theoretic solution

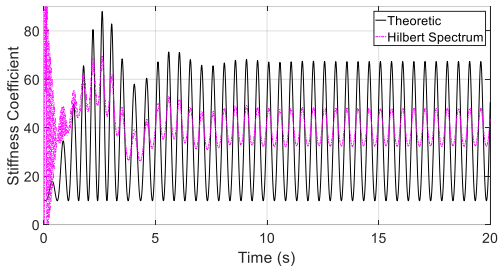

(b) Instantaneous vs. theoretic solution

Figure 5.21. The proposed, instantaneous, and theoretic stiffness coefficients

In damage detection, the alteration of a system in material and geometry is reflected in the change of system parameters. Such an alteration is relatively easy to identify when the system parameter such as α or $2h$ changes slowly. However, the fast-varying component is usually difficult to observe. To further demonstrate the effectiveness of the proposed method in damage detection, β/α is reduced from $1000/\pi^2$ to $600/\pi^2$ and the identified stiffness coefficients are compared in Figure 5.22. It can be seen from Figure 5.22(a) that the valleys in two cases are comparable when the smallest stiffness is achieved when the displacement of the oscillator is equal to zero. The difference in peak value as observed throughout the time duration indicates the change in β/α ratio or the occurrence of damage. These observations can be seen more clearly in Figure 5.22(b) as the steady-

state response and the identified stiffness coefficient become stabilized over time. As such, the minor differences can be successfully identified with M-AMD.

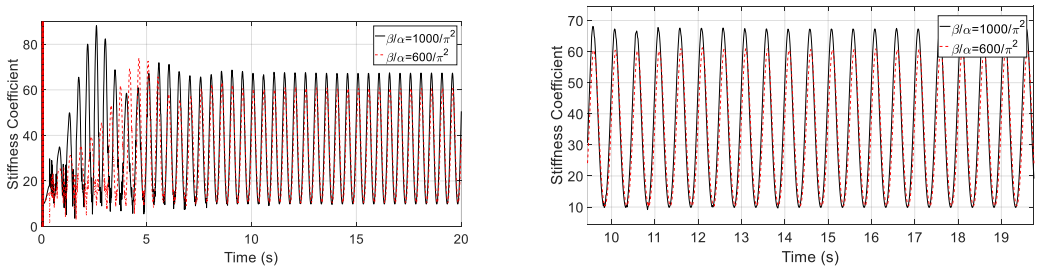

(a) Complete solution (b) Steady-state solution

Figure 5.22. Comparison of identified stiffness coefficients of the Duffing oscillator with different β values

5.3.2. ¼-scale Three-story Building Model under Earthquake Excitations. The structure used for this experimental study is a 1/4-scale, 3-story building model with one piezoelectric friction damper (PFD) installed in the 1st story. The building model is 1.22 m long, 0.61 m wide and 2.54 m tall, as shown in Figure 5.23. It is a moment-resisting steel frame structure in longitudinal (earthquake excitation) direction, and an X-braced structure in transverse direction. Each floor built with a grid of structural tees is considered to be rigid. Four accelerometers were attached on three floors and the shake table to measure the structural accelerations and the earthquake input. Three LVDTs were installed between the structure and a stand-alone rigid frame to measure the absolute displacements at each floor. The internal LVDT of the shake table was used to measure the shake table displacement. The clamping force of the friction damper was measured with four pancake load cells.

The steel plates added on the 1st, 2nd, and 3rd (top) floor weigh 480, 446 and 432 kg, respectively. Before the installation of the damper, the 1st, 2nd and 3rd natural frequencies were identified with several swept-sine tests as 2.66, 9.46 and 18.70 Hz, respectively [88].

Since the natural frequencies of the test structure are well spaced, the influence of non-resonant modes on the resonant response is negligible, provided that the structure is lightly damped. Therefore, the modal damping ratios of the structure can be determined from the transfer functions with the half-power method [89]. They are 0.56%, 0.39% and 0.32% for the 1st, 2nd, and 3rd modes, respectively. The mass, damping, and stiffness matrices of the building model can thus be expressed into:

$$\boldsymbol{M} = \begin{bmatrix} 1058 & 0 & 0 \\ 0 & 983 & 0 \\ 0 & 0 & 954 \end{bmatrix} \text{kg}, \quad \boldsymbol{C} = \begin{bmatrix} 238.1 & -87.5 & -12.7 \\ -87.5 & 240.0 & -82.9 \\ -12.7 & -82.9 & 159.9 \end{bmatrix} \text{N-s/m},$$

$$\boldsymbol{K} = \begin{bmatrix} 2.865 & -2.344 & 0.440 \\ -2.344 & 3.776 & -1.774 \\ 0.440 & -1.774 & 1.381 \end{bmatrix} \times 10^6 \text{ N/m}. \tag{42}$$

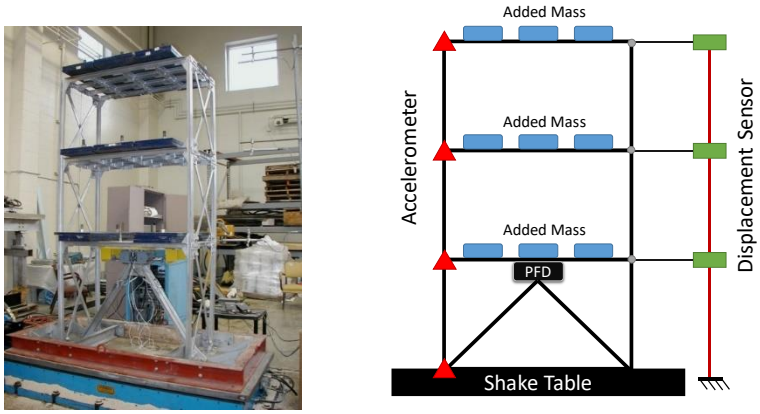

(a) Actual test setup (b) Schematic diagram

Figure 5.23. Shake table test of the 3-story building model

The friction damper used in this study was designed and fabricated by Garrett et al. [90]. The prototype and its schematic representation are shown in Figure 5.24. The damper has a dimension of 0.254 m × 0.152 m × 0.102 m. It includes four piezoelectric stack actuators to modulate its clamping force. The damper was characterized under harmonic loading and then installed between a bracing support fixed on the shake table and the 1st

floor of the 3-story frame structure, as shown in Figure 5.23. The frictional sliding plate within the damper was connected to the bottom side of the 1st floor with a rigid assembly to ensure proper transferring of the friction force from the damper to the test structure.

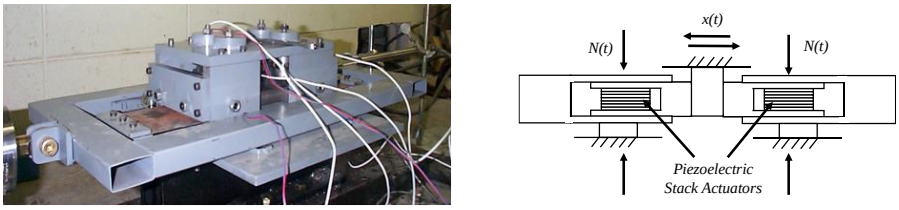

(a) Prototype with four piezoelectric actuators (b) Schematic diagram

Figure 5.24. Piezoelectric friction damper

The semi-active control strategy developed to drive the piezoelectric friction damper combined the Coulomb friction, viscous, and Reid's damper mechanisms [88, 91]. The goal of the semi-active control was to suppress the vibration of a structure when the structural deformation and its derivative exceeded a threshold value. The control strategy can be expressed into a mathematical relation among the clamping force, $N(t)$, the structural deformation (story drift of a building), $x(t)$, and the velocity, $\dot{x}(t)$:

$$N(t) = \begin{cases} N_{pre} & a|x(t)| + b|\dot{x}(t)| \le N_{pre} \\ a|x(t)| + b|\dot{x}(t)| & a|x(t)| + b|\dot{x}(t)| > N_{pre} \end{cases}, \quad (43)$$

in which a and b are two positive gain factors. The 1st part of Equation (43) represents the passive Coulomb damper, while the 2nd part is its active counterpart. The active control strategy is engaged only when the structural responses, $x(t)$ and $\dot{x}(t)$, are excessive. The preload of the friction damper is set to be N_{pre} =89 N per actuator, amounting to 356 N in four actuators. Since the fundamental frequency of the test structure is 2.66 Hz, the optimal gain ratio, *a/b*, is approximately estimated to be 1.69 1/s [92]. A value of b= 7.01 kN-s/m is used for all tests.

In order to evaluate the proposed control strategy, the N-S component of the 1995 Kobe earthquake was used to excite the building model. Since the shake table was limited to a maximum stroke of ±2.54 cm, the earthquake records were compressed in time scale to make their dominant frequencies approximately equal to the fundamental frequency of the structure tested so that sufficiently large responses of the structure can be generated. A time scale of 1/1.825 was applied for Kobe earthquake, and the time history was also modified in magnitude with 0.177 g. Shake table tests were then conducted for the uncontrolled and controlled structure with the semi-active control strategy and the prototype damper. Fourier spectra of the uncontrolled and controlled 1st floor accelerations of the building model under the same scaled earthquake excitation are presented in Figures 5.25(a) and 5.25(b), respectively. For the uncontrolled model, three frequency components are well separated with clearly identifiable peaks. For the controlled model, the implementation of the semi-active damper widens the frequency band around each peak, indicating the lumped effect of nonlinear damping into presence of fast-varying components around each main frequency component.

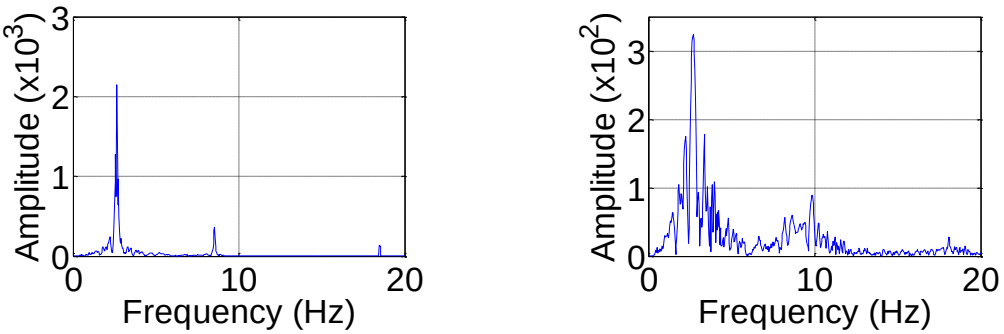

(a) Uncontrolled (b) Controlled

Figure 5.25. Fourier spectra of the 1st floor accelerations

The accelerations recorded from the installed accelerometers are integrated twice over time and compared in Figure 5.26 with the measured displacements captured by the displacement sensors. It can be seen from Figure 5.26 that the integrated and measured displacements are in good agreement at all three floors. The largest difference in top displacement is found to be less than 1%..

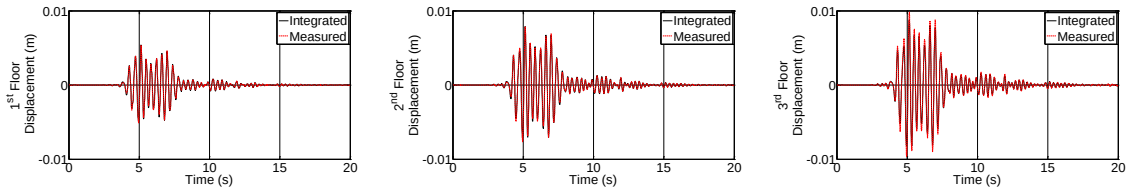

Figure 5.26. Comparison of integrated and measured displacement time histories

The equations of motion of the 3-story building model with one piezoelectric friction damper can be formulated as follows:

$$\begin{cases} m_1\ddot{x}_1 + c_{11}\dot{x}_1 + c_{12}\dot{x}_2 + c_{13}\dot{x}_3 + k_{11}x_1 + k_{12}x_2 + k_{13}x_3 = -m_1\ddot{u}_g - \mu N sgn(\dot{x}_1) \\ m_2\ddot{x}_2 + c_{21}\dot{x}_1 + c_{22}\dot{x}_2 + c_{23}\dot{x}_3 + k_{21}x_1 + k_{22}x_2 + k_{23}x_3 = -m_2\ddot{u}_g \\ m_3\ddot{x}_3 + c_{31}\dot{x}_1 + c_{32}\dot{x}_2 + c_{33}\dot{x}_3 + k_{31}x_1 + k_{32}x_2 + k_{33}x_3 = -m_3\ddot{u}_g \end{cases}, \quad (44)$$

where $sgn(\cdot)$ is the sign function and the damping and stiffness coefficients are referred to the damping and stiffness matrix. After the deployment of the friction damper in the 1st story, the ground motion, $\ddot{u}_g$, can be directly obtained from the 2nd or 3rd floor's responses, as demonstrated in Figure 5.27. The two ground motions obtained from the 2nd and 3rd equations in Equation (44) are compared very well in Figure 5.27.

After the ground motion is determined, the first part of Equation (44) will be analyzed to identify the characteristic damping coefficients of the friction damper. The equation of motion can be rewritten as:

$$m_1\ddot{x}_1 + [c_{11} + \mu N(t)/|\dot{x}|]\dot{x}_1 + k_{11}x_1 = f(t) \quad (45)$$

in which $f(t) = -\left(c_{12}\dot{x}_2 + c_{13}\dot{x}_3 + k_{12}x_2 + k_{13}x_3 + m_1\ddot{u}_g\right)$ is known. Equation (45) represents a SDOF nonlinear oscillator under an external excitation $f(t)$. Due to stick and sliding phase exchanges, $\mu N(t)/|\dot{x}|$ expects to include frequency contents higher than those of $\dot{x}_1$. Parameters c_{11} and k_{11} as slow-varying components can first be obtained from Equations (44) and (45) following the proposed forced M-AMD method. They are presented in Figure 5.28 and compared with the values (c_{11}/m_1 =0.225 $1/s$, k_{11}/m_1=2707.9 $1/s^2$) as shown in Equation (42), which were identified without the friction damper. The average values of the identified damping and stiffness coefficients over time are 0.222 $1/s$ and 2708.5 $1/s^2$, respectively. The identified results include 1.3% and 0.02% in error only, indicating high accuracy of the proposed method.

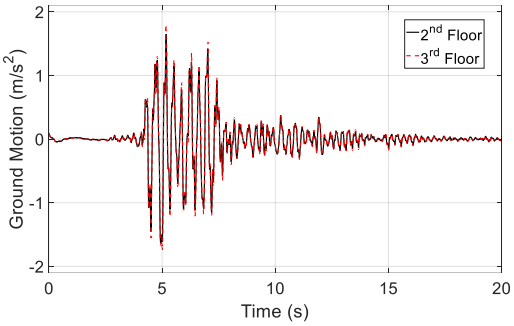

Figure 5.27. Comparison of the ground accelerations derived from the 2nd and 3rd floor responses

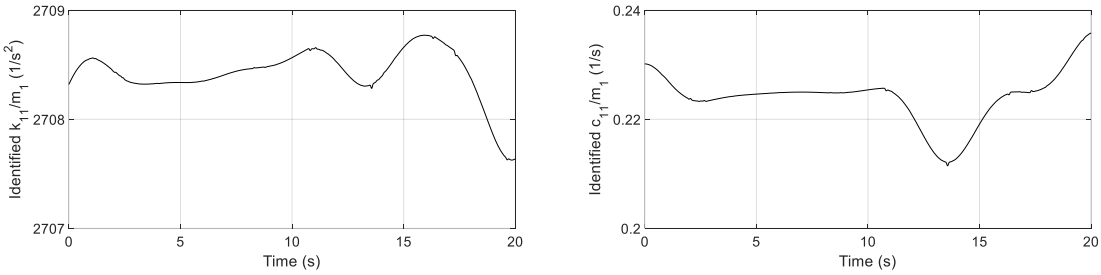

Figure 5.28. Identified slow-varying parameters of the 1st floor

After the two slow-varying components have been identified, Equations. (41) and (45) can be used to determine the fast-varying component, $2h_f = \mu N(t)/|\dot{x}|$:

$$2h_f = \frac{\mu N(t)}{|\dot{x}|} = \frac{f(t) - m_1\ddot{x}_1 - c_{11}\dot{x}_1 - k_{11}x_1}{\dot{x}}, \quad \dot{x} > 1\ mm/s. \tag{46}$$

A threshold value of 1 mm/s for $\dot{x}_1$ is set to remove the singularity and numerical instability associated with the sign function at zero velocity. Although the friction force can now be identified from Equation (46), the two gain factors during the active control process must be further investigated. To enable a direct comparison with the clamping force that remains positive over time, the absolute value of the friction force is determined from Equation (46). That is,

$$|\mu N(t)| = |f(t) - m_1\ddot{x}_1 - c_{11}\dot{x}_1 - k_{11}x_1|. \tag{47}$$

The friction force $|\mu N(t)|$ calculated from Equation (47) is compared in Figure 5.29(a) to the measured total clamping force. It can be observed from Figure 5.29(a) that the friction force is generally proportional to the measured clamping force with the stable low values taken outside the duration of earthquake excitations (<4 s and >15 s). Therefore, an average friction force of $\mu N_{pre} = 285$ N can be obtained from the stable values, which is basically the same as its exact value. The data in Figure 5.29(a) are reproduced in Figure 5.29(b) in terms of the coefficient of friction. The results in Figure 5.29(b) indicate that the coefficient of static friction (<4 s and >15 s) is approximately 0.8 as used in the PFD design. The coefficient of kinetic friction is less than 0.8 as expected. The larger-than-0.8 coefficient spikes at few instants correspond to the transition between sliding and stick phases of the PFD.

When the active control strategy is effective between 4 s and 15 s, the following equation holds:

$$\mu a|x(t)| + \mu b|\dot{x}(t)| = |\mu N(t)|. \quad (48)$$

Similar to the procedure of the M-AMD algorithm, the two unknown gain factors (μa, μb) in Equation (48) can be determined from Equation (48) and its Hilbert transform as written as:

$$\mu b = \frac{|\mu N(t)|H[|x|] - H[|\mu N(t)|]|x|}{|\dot{x}|H[|x|] - H[|\dot{x}|]|x|}, \quad (49)$$

$$\mu a = \frac{|\mu N(t)|H[|\dot{x}|] - H[|\mu N(t)|]|\dot{x}|}{|x|H[|\dot{x}|] - H[|x|]|\dot{x}|}. \quad (50)$$

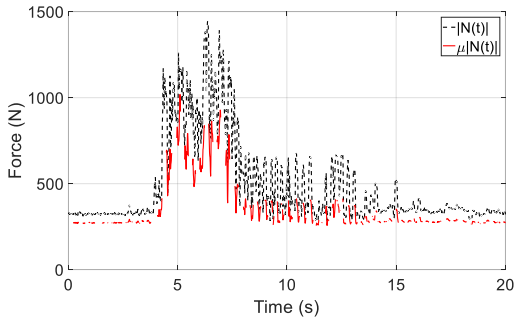

(a) Comparison of the identified friction to measured clamping force

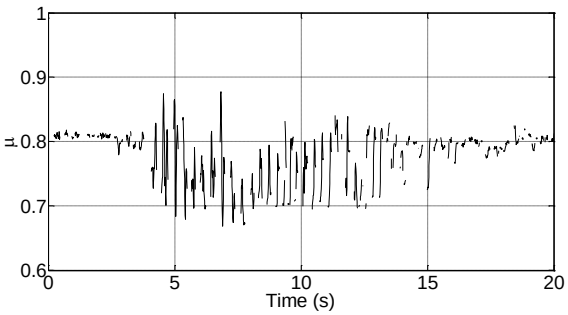

(b) Identified friction coefficient

Figure 5.29. The measured clamping force, identified friction, and identified friction coefficient

Figure 5.30 shows the identified results of μa and μb with a large variation between 4 s and 7.5 s when the building was subjected to strong excitations. After 7.5 s, the identified results vary slightly with their average values of 9.56 kN/m and 5.66 kN-s/m

and standard deviations of 0.196 kN/m and 0.326 kN-s/m, respectively. Considering a friction coefficient of 0.8 that was identified at the early stage of experiments [92], a and b are 11.95 kN/m and 7.08 kN-s/m, respectively. In comparison with their design values of 11.85 kN/m and 7.01 kN-s/m, the errors for the identified a and b are 0.8% and 1%.

The ratio of a to b is also calculated at various time instants as presented in Figure 5.31. The average and standard deviation of a/b are 1.710 s^{-1} and 0.847 s^{-1}, respectively. The average value of a/b has an error of 1% when compared with its theoretic value of 1.693 s^{-1}.

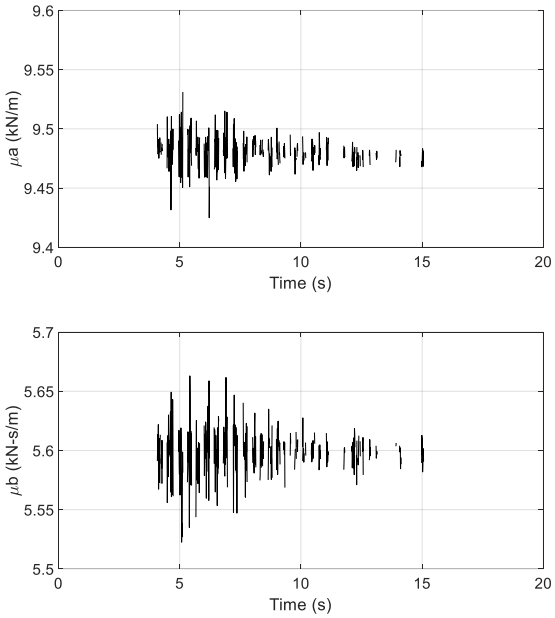

Figure 5.30. Identification of gain factors during active control

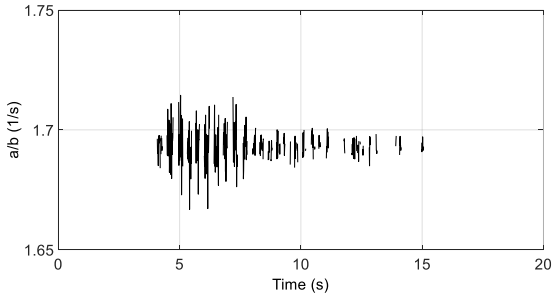

Figure 5.31. Identified a/b value over time

5.4. SUMMARY

The instantaneous parameter identified from the dynamic response of a nonlinear system significantly differs in magnitude and trend from the corresponding parameter of the system. They are not exchangeable as mistakenly used in some literatures. In this section, multiple analytical mode decompositions (M-AMD) are proposed to identify the parameters of nonlinear oscillators and structures from both free and forced vibrations to address the issue. The time-varying damping (stiffness) coefficient of an oscillator is divided into slow- and fast-varying components by a bisecting frequency in reference to velocity (displacement). The slow-varying damping and stiffness components are estimated from the oscillator's responses and their Hilbert transforms, and filtered with the adaptive low-pass filter AMD. Each fast-varying component is estimated from the oscillator's responses and the determined slow-varying components, and corrected with AMD using an approximate bisecting frequency of the two fast-varying components.

The computational efficiency and accuracy of the proposed M-AMD are first illustrated with three characteristic oscillators described by Duffing, Bouc-Wen, and spherical bearing models from free vibration. The M-AMD method is considerably more accurate and robust than the FREEVIB method in the identification of system parameters. The errors with the M-AMD method are less than 3% in all three representative nonlinear oscillators when the system responses are not contaminated by noises. In the case of Duffing oscillator, the M-AMD is more accurate than the FREEVIB method by at least one order of magnitude. The overall error of the proposed method is less than 1.2% unless the ratio between the nonlinear and linear terms of the restoring force exceeds approximately 26. Also, the instantaneous stiffness determined from Hilbert spectral analysis differs from

the system stiffness by an amount that rapidly increases with the degree of system nonlinearity. In the case of spherical bearing, the proposed method resulted in less than 8.4% errors in the entire practical range of friction coefficient. More specifically, the error of the proposed method is less than 1.2% when the coefficient of friction is less than 0.017. Noises in system responses have little effect on the evaluation of system parameters when AMD is involved in the process of system identification. Otherwise, AMD must be applied to the system responses. In both cases, the effect of noises on the identified parameters of all three oscillators is less than approximately 9% when the RMS displacement of noises is less than 0.05% of the peak displacement of oscillators. The proposed method is significantly more accurate than the FREEVIB method in terms of noise effect.

The effectiveness of the M-AMD is also demonstrated with a Duffing oscillator subjected to harmonic loading and a ¼-scale, 3-story building model installed with a semi-active PFD under earthquake excitations. The instantaneous parameters identified in the FORCEVIB from the dynamic responses of a nonlinear system significantly differ in magnitude and trend from their exact values. The identified results from Hilbert spectral analysis as widely used in literature are even worse in accuracy. Only the proposed M-AMD method yields results with high accuracy. In the case of Duffing oscillator, the overall error of the proposed method without end effects is less than 3%. The slow-varying damping coefficient can be successfully identified with high accuracy. Both the slow- and fast-varying components of stiffness coefficient have been accurately taken into account in the proposed M-AMD. In the case of 3-story building model, the passive control force related to Coulomb friction can be accurately determined from the identified friction force after the building ceases to vibrate at the end of earthquake excitations. Under the

scaled/strong Kobe earthquake excitations, the active control force can be extracted from the measured building responses. Based on the active control force, the two gain factors can be further identified with less than 1% in error.

6. SEISMIC TEST OF 1/20 SCALE BRIDGE MODEL

6.1. OPTIMIZED ANALYTICAL MODE DECOMPOSITION ALGORITHM

AMD as a powerful mode decomposition method [2] is introduced briefly in this Section. An optimization algorithm to take into account the digitization/discretization effect of analog signals is then proposed to overcome the shortcomings of AMD.

Figure 6.1 shows the essence and schematic diagram of the AMD. A general time signal, $x(t)$, consists of n significant frequency components ($\omega_1, \omega_2, \dots, \omega_n$). The decomposed time series, corresponding to each frequency component, are denoted by $x_{di}(t), i = 1, 2, \dots, n$. They are related to the original signal by

$$x(t) = \sum_{i=1}^{n} x_{di}(t) \tag{51}$$

Let ω_{bi} be the bisecting frequency between ω_i and ω_{i+1}, $i = 1, 2, \dots, n$. The decomposed time series can be determined from

$$x_{d1}(t) = s_1(t), x_{d2}(t) = s_2(t) - s_1(t), \dots,$$
$$x_{di}(t) = s_i(t) - s_{i-1}(t), x_{dn}(t) = x(t) - s_n(t) \tag{52}$$

Here, a low-frequency time series is defined by the signal decomposition theorem [2]:

$$s_i(t) = \sin(\omega_{bi}t)\, H[x(t)\cos(\omega_{bi}t)] - \cos(\omega_{bi}t) H[x(t)\sin(\omega_{bi}t)] \tag{53}$$

where $H[\cdot]$ denotes the Hilbert Transform.

For time-variant signals, it may not be feasible to extract the frequency characteristics using Fourier transform, as the frequency of each signal component changes over time, and two or more frequency components might have a common frequency range in certain circumstances. Thus, instead of the fixed values of each bisecting frequency, they are changed into the functions of time that could accommodate the time-variant feature of

the signal components. The bisecting frequency functions are based on the newly proposed AWA, which has a superior time-frequency representation of the original signal.

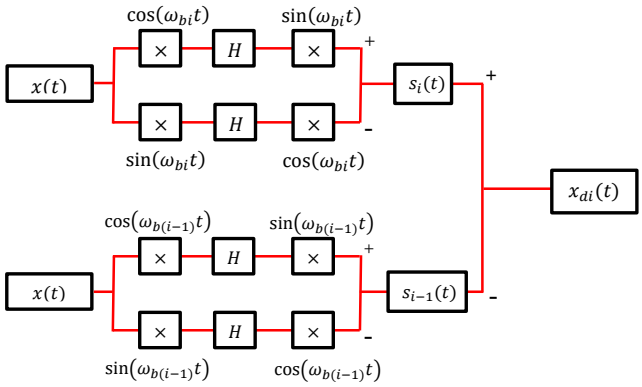

Figure 6.1. AMD algorithm

In this case, the frequencies of each decomposed signal are denoted as $\omega_1(t), \omega_2(t), \dots, \omega_n(t)$. Each decomposition of the original signal could be achieved if the bisecting frequency, $\omega_{bi}(t)$, satisfies $\omega_{i-1}(t) < \omega_{bi}(t) < \omega_i(t), i = 2, 3, \dots, n$. Two groups of time series, $s_i(t)$ and $x_{di}(t)$, are defined in the same way as time-invariant signals. Thus, the decomposed signals can be obtained in phase domain by:

$$s_i(t) = sin(\theta_{bi})\, H[x(f^{-1}(\theta_{bi}))\, cos(\theta_{bi})] - cos(\theta_{bi}) H[x(f^{-1}(\theta_{bi}))sin(\theta_{bi})]. \quad (54)$$

where $t = f^{-1}(\theta_{bi})$ and $\theta_{bi}(t) = f(t) = \int_0^t \omega_{bi}(\tau)d\tau$ are the phase angle of the bisecting frequency $\omega_{bi}(\tau)$.

In frequency domain, Equation (53) with a general bisecting frequency ω_b corresponds to the frequency response function, $G(\omega)$, of an AMD low-pass filter as defined by:

$$G(\omega) = \frac{1}{2} sgn(\omega + \omega_b) - \frac{1}{2} sgn(\omega - \omega_b). \quad (55)$$

Once the signal is discretized with a sampling frequency of ω_s, as encountered in engineering applications, AMD introduces some distortions on the original signal with a modified frequency response function $G_m(\omega)$:

$$G_m(\omega) = \frac{1}{2} sgn\left[\frac{\omega_s}{2} - (\omega + \omega_b)\right] sgn(\omega + \omega_b) - \frac{1}{2} sgn\left[\frac{\omega_s}{2} - (\omega - \omega_b)\right] sgn(\omega - \omega_b). \quad (56)$$

To minimize the signal distortions, a recursive AMD is proposed to optimize the following frequency response function:

$$G_r(\omega) = \begin{cases} \frac{1}{2} G_m(\omega) + \frac{1}{2} {G_m}^2(\omega) & 0 < \omega_b < \frac{1}{4}\omega_s \\ 1 + \frac{1}{2} G_m(\omega) - \frac{1}{2} {G_m}^2(\omega) & \frac{1}{4}\omega_s < \omega_b < \frac{1}{2}\omega_s \end{cases}. \quad (57)$$

By further derivations, Equation (57) can be simplified into:

$$G_r(\omega) = \begin{cases} 1 & \omega < \omega_b \\ 0 & \omega > \omega_b \end{cases}, \quad (58)$$

which represents a non-distorted low-pass filter for the digital/discretized signal.

In time domain, Equation (57) can be implemented for time-invariant signals such as given in Equation (53) by:

$$s_i(t) = \begin{cases} \frac{1}{2} AMD[x(t)] + \frac{1}{2} AMD[AMD[x(t)]] & 0 < \omega_{bi} < \frac{1}{4}\omega_s \\ x(t) + \frac{1}{2} AMD[x(t)] - \frac{1}{2} AMD[AMD[x(t)]] & \frac{1}{4}\omega_s < \omega_{bi} < \frac{1}{2}\omega_s \end{cases} \quad (59)$$

Similarly, Equation (57) can be applied to time-variant signals in phase domain, such as given in Equation (54):

$$s_i(t) = \begin{cases} \frac{1}{2} AMD[x(\theta)] + \frac{1}{2} AMD\left[AMD[x(\theta)]\right] & 0 < \omega_{bi}(\mathrm{t}) < \frac{1}{4}\omega_s(t) \\ x(\theta) + \frac{1}{2} AMD[x(\theta)] - \frac{1}{2} AMD\left[AMD[x(\theta)]\right] & \frac{1}{4}\omega_s(\mathrm{t}) < \omega_{bi}(\mathrm{t}) < \frac{1}{2}\omega_s(t) \end{cases} \quad (60)$$

6.2. NUMERICAL EXAMPLES

After the introduction of the optimization approach of AMD, numerical examples are given in this section for the illustration of its effectiveness.

6.2.1. Sinusoidal Signal with Large Frequency Variation. The signal considered as an example is composed of two time-varying cosine functions with a sampling rate of 10,000 Hz, as illustrated in Figure 6.2(a):

$$f_1(t) = \cos[2\pi 2000t + 100\sin(2\pi 10t)] \tag{61}$$

$$f_2(\mathrm{t}) = \cos[2\pi 2500t + 100\sin(2\pi 10t)] \tag{62}$$

In the time-frequency plane, the signal with the projected bisecting frequency variation function (a dashed red curve) is shown in Figure 6.2(b).

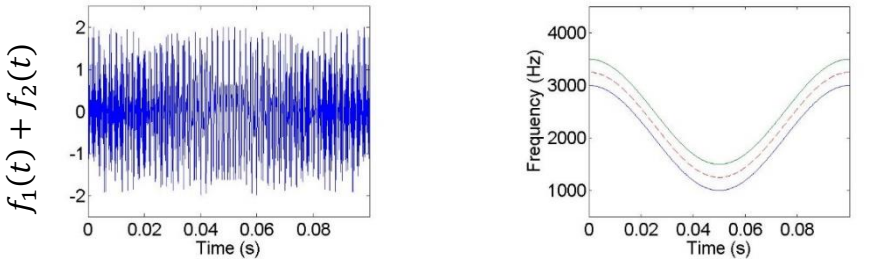

(a) Signal in time domain (b) Time-frequency representation

Figure 6.2. Sinusoidal signal

AWT of the signal is presented in Figure 6.3(a), which is better than any CWT as represented by Figure 6.3(b). The bisecting frequency corresponding to the dashed red curve in Figure 6.2(b) is thus obtained with a clear separation of two frequency components from the AWT.

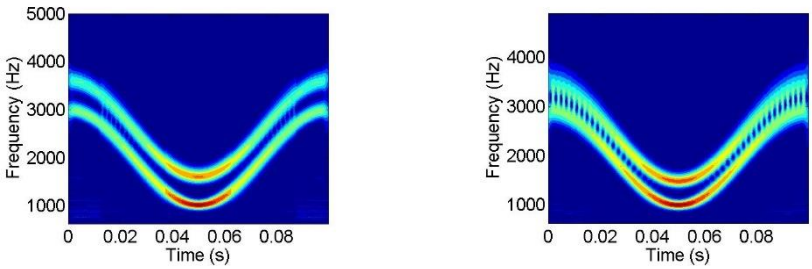

(a) AWT (b) CWT

Figure 6.3. Wavelet transforms of sinusoidal signal

Since the sampling rate of the signal, 10,000 Hz, is less than four times the higher frequency (2500 Hz - 3500 Hz), the signal may not be decomposed accurately with one application of AMD. As shown in Figure 6.4, the decomposed lower frequency part matches either the theoretic lower frequency component in the middle portion in Figure 6.4(a) or the theoretic higher frequency component at the beginning and ending portions in Figure 6.4(b). Multiple applications of AMD are thus performed using Equation (60) by fitting the frequency range into the suited condition. The recursive low-frequency component as shown in Figure 6.5 and its comparison with theoretic values indicates a successful decomposition of the signal.

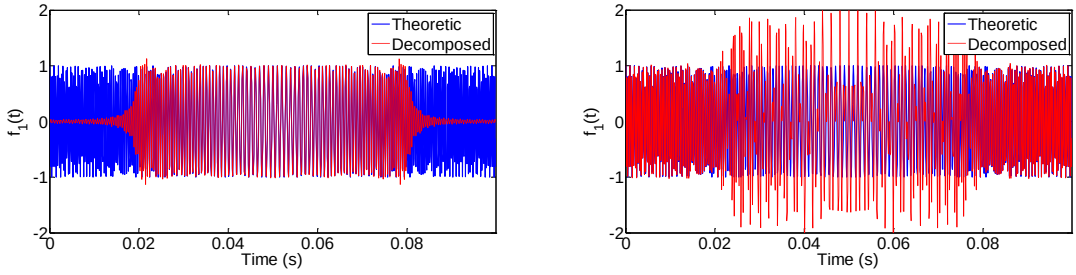

(a) $0 < \omega_b(t) < \frac{1}{4}\omega_s(t)$ (b) $\frac{1}{4}\omega_s(t) < \omega_b(t) < \frac{1}{2}\omega_s(t)$

Figure 6.4. Theoretic and decomposed low-frequency component of the sinusoidal signal from one AMD application

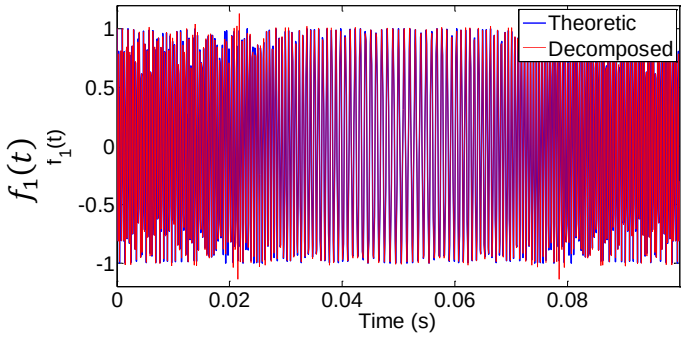

Figure 6.5. Comparison of the theoretic and decomposed low-frequency component of the sinusoidal signal from the recursive AMD applications

The index of accuracy (IA) is proposed here to quantify the difference between the decomposed and original signal components. For the quantification of accuracy of component $x_i(t)$, IA is defined by

$$IA_i = \frac{\sqrt{\int_0^T [x_{di}(t) - x_i(t)]^2 dt}}{\sqrt{\int_0^T [x_i(t)]^2 dt}} \tag{63}$$

where $x_{di}(t)$ is the i^{th} decomposed signal component, and $x_i(t)$ is the exact i^{th} component from the original signal. For the analytical signal as expressed in Equations (61) and (62), the IAs pf the two components equal 4.59%, indicating a satisfactory agreement between the decomposed and the original components of the signal.

6.2.2. Chirp Function. A two-chirp signal with two increasing frequencies over time is considered as a second example as shown in Figure 6.6. The bisecting frequency is chosen as the red dashed line between the two changing frequencies extracted by the AWA, as shown in Figure 6.7.

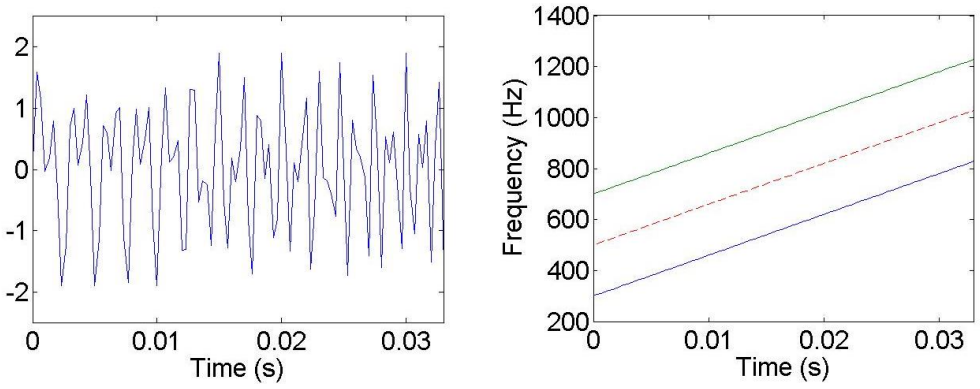

(a) Signal in time domain (b) Time-frequency representation

Figure 6.6. Theoretical representation of a two-chirp signal

The sampling rate of the signal is set to 3,000 Hz, which does not satisfy either conditions in Equation (60) and thus cannot accurately decompose the signal into

components in a single AMD application, as indicated in Figure 6.8 from the comparison between the decomposed and theoretic low frequency components. However, the recursive AMD applications provide a good agreement between the decomposed and theoretical low frequency components as shown in Figure 6.9. Based on Equation (62), IA is calculated to be 8.4% for both components.

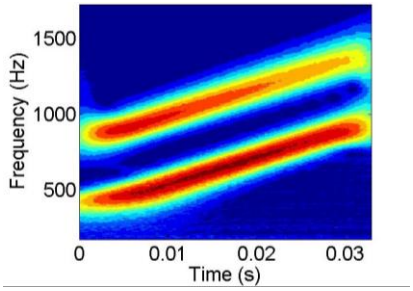

Figure 6.7. AWA of the two-chirp signal

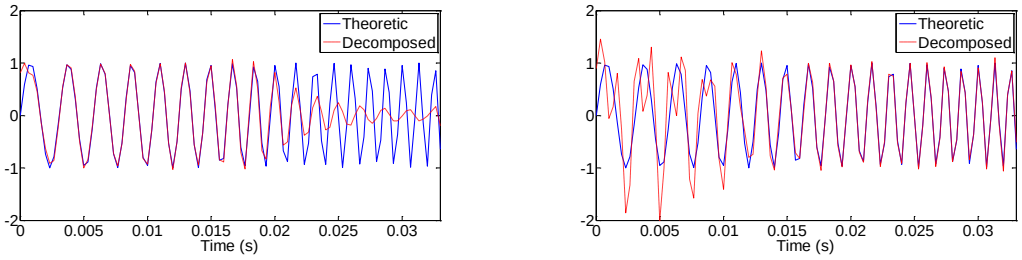

(a) $0 < \omega_b(t) < \frac{1}{4}\omega_s(t)$ (b) $\frac{1}{4}\omega_s(t) < \omega_b(t) < \frac{1}{2}\omega_s(t)$

Figure 6.8. Theoretic and decomposed low-frequency component of the chirp signal by a single AMD application

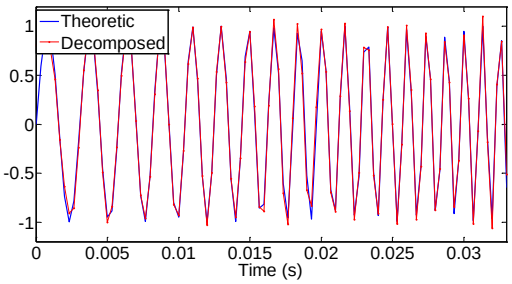

Figure 6.9. Comparison of the decomposed and theoretic low frequency chirp components

6.2.3. Two Closely-spaced Duffing Systems. The third example is a signal that consists of two closely-spaced Duffing systems, both with an initial displacements of 100. The two systems are described by:

$$\ddot{x} + 0.05\dot{x} + x + 0.01x^3 = 0 \tag{64}$$

$$\ddot{x} + 0.05\dot{x} + 3x + 0.02x^3 = 0 \tag{65}$$

The signal is sampled at a rate of 4 Hz. The time signal and its time-frequency representation are presented in Figures 6.10(a) and 6.10(b), respectively. AWT can give a satisfactory time-frequency representation as shown in Figure 6.11. The bisecting frequency can thus be selected as a dashed red parabolic curve, as shown in Figure 6.10(b), between the two signal frequencies.

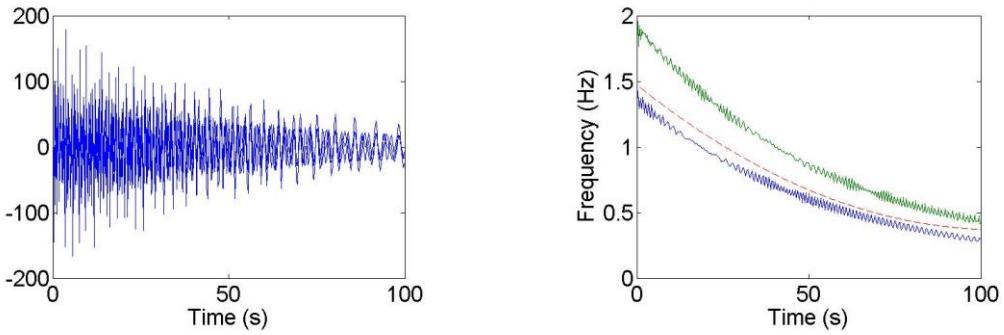

(a) Signal in time domain (b) Extracted instantaneous frequencies

Figure 6.10 Signal and time-frequency representation of two Duffing systems

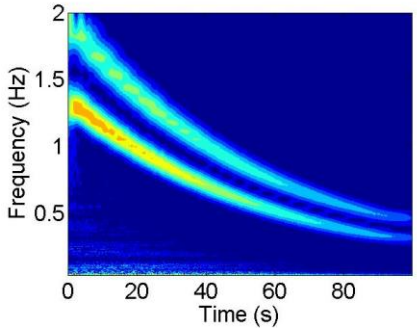

Figure 6.11. AWT of the two Duffing systems

Similarly, a single application of AMD gives an inaccurate decomposition of a portion of the Duffing signal as shown in Figure 6.12(a, b) for the two conditions in Equation (60). However, multiple applications of the AMD as required in the recursive AMD in Equation (60) results in an accurate decomposition of the low frequency component, as compared in Figure 6.13 with the theoretic value. Except for minor differences due to end effect, the extracted signal matches the theoretic signal very well with an IA value of 6.5%.

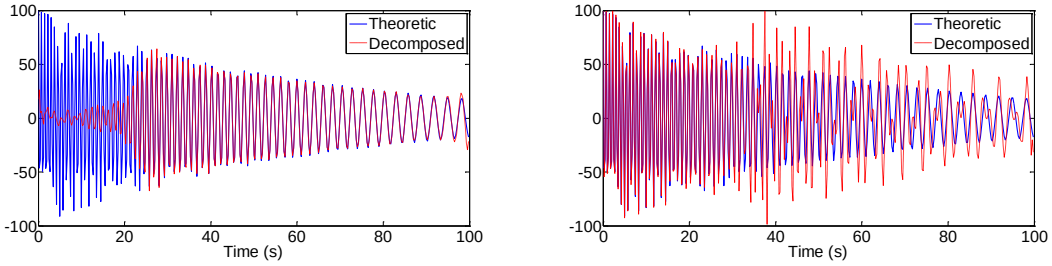

(a) $0 < \omega_b(t) < \frac{1}{4}\omega_s(t)$ (b) $\frac{1}{4}\omega_s(t) < \omega_b(t) < \frac{1}{2}\omega_s(t)$

Figure 6.12. Theoretic and decomposed low-frequency component of the Duffing signal by one application of AMD

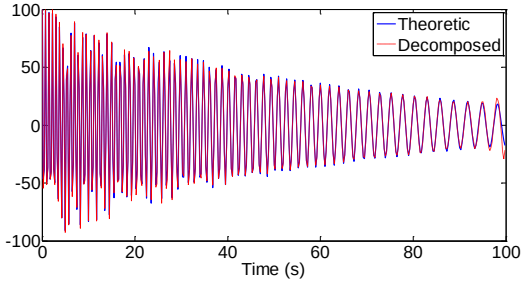

Figure 6.13. Comparison of the theoretic and decomposed low-frequency component of the Duffing signal by the recursive AMD applications

6.3. SHAKE TABLE TEST OF CABLE-STAYED BRIDGE MODEL

As the final validation, AWT and M-AMD are combined to identify the damage development of a 1/20-scale cable-stayed bridge model under earthquake excitation.

6.3.1. Test Setup. A typical cable-stayed bridge in China is considered as a benchmark in this study. As sketched in Figure 6.14, the bridge consists of a main span (380 m) of steel box girder and four side spans (60 m and 70 m) of concrete box girder. Both the steel and concrete box girders are 35.5 m wide and 3.5 m high. As shown in Figure 6.15, the main towers of 100.35 m high and piers are made of reinforced concrete. The towers are made of concrete materials (C50), which have 32.4 MPa in uniaxial compressive strength and 3.45×10^4 MPa in the modulus of elasticity, respectively. For bridge piers, concrete (C40) is used with 26.8 MPa in compressive strength and 3.25×10^4 MPa in the modulus of elasticity. The steel box girder is made of the special D-grade steel plate with a nominal yield strength of 345 MPa designed for bridges (Q345qD), while the concrete girder is C55 concrete with 35.5 MPa in strength and 3.55×10^4 MPa in the modulus of elasticity. Hot-rolled ribbed bars with a nominal yield strength of 400MPa (HRB400) and the modulus of elasticity of 2.1×10^5 MPa are used as longitudinal reinforcement for all reinforced concrete members.

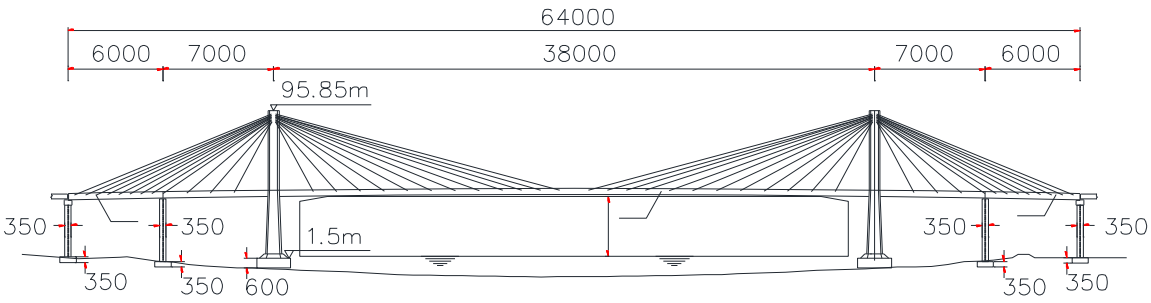

Figure 6.14. Elevation view of the cable-stayed bridge (unit: cm)

A 1/20-scale bridge model, as shown in Figure 6.16, was designed and built to replicate the cable-stayed bridge in Figure 6.14 [93]. It was tested on the world's largest multifunctional four-table facility at Tongji University to investigate and understand its

nonlinear behavior under extreme earthquake excitations. The bridge model sits on four shake tables that apply the same seismic excitation simultaneously.

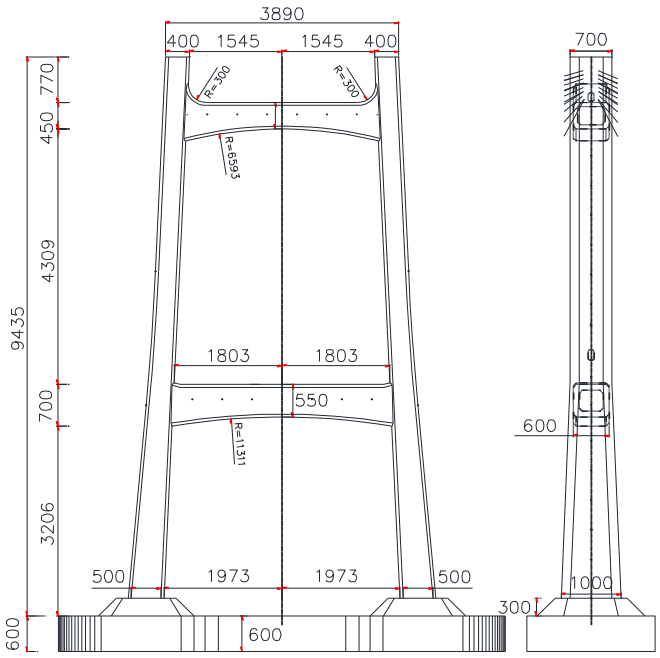

Figure 6.15 Design detail of the bridge tower (unit: cm)

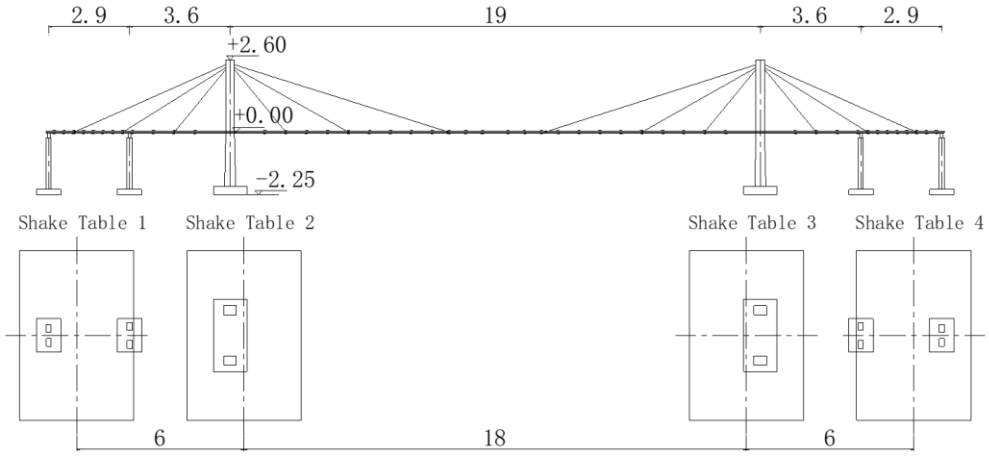

Figure 6.16. Test setup of the bridge model (unit: m)

The similitudes of the model bridge design are given in Table 6.1 for RC and steel members. In order to meet the similitudes for the RC members, 6 mm-diameter HRB335

was used as longitudinal reinforcement, and lead wires were used as stirrups. At the same time, micro-concrete was introduced to the bridge model for the towers and piers, with a concrete cover of 10 mm. The bridge girder was simplified into rectangular hollow beams formed with 10 mm-thick steel plates. The cross-section dimension of the beams is 700 mm × 65 mm in the main span and 900 mm × 65 mm in the side span, which strictly follows the similitude of bending stiffness with neglected torsional effect.

Table 6.1. Similitudes of the bridge model to the actual bridge

Parameter	**Reinforced Concrete Member**	**Steel Member**
Length	0.05	0.05
Elastic of Modulus	0.3	1
Acceleration	1	1
Density	6	20
Mass	0.00075	0.0025
Stiffness	0.015	0.05
Period	0.2236	0.2236
Force	0.00075	0.0025
Moment	0.0000375	0.000125
Moment of Inertia	0.00000625	0.00000625
Stress	0.3	1
Strain	1	1
Damping Ratio	1	1

To determine concrete properties of the bridge model, three 71 mm × 71 mm × 71 mm and three 100 mm × 100 mm × 300 mm concrete cubes made from the same concrete material were prepared and standard-cured for 28 days. The first three coupons were for the measurement of compressive strength, which averages at 14.9 MPa, while the second three give an averaged modulus of elasticity of 1.17×10^4 MPa. The details of each coupon are listed in Table 6.2. The model-to-bridge similitudes in terms of compressive strength and the modulus of elasticity of the micro-concrete are 0.298 and 0.339 respectively, which are in general agreement with the theoretical value (0.3). Based on the

tests of three coupons from the HRB335 steel, as detailed in Table 6.3, the average measured yield strength is 260 MPa, and the averaged ultimate strength is 432 MPa.

Table 6.2. Coupon test of concrete specimens

Coupon	Compressive Strength (MPa)	Modulus of Elasticity (MPa)
1	14.8	1.02×10^4
2	15.1	1.45×10^4
3	14.8	1.04×10^4
Average	14.9	1.17×10^4

Table 6.3. Coupon test of steel rebars

Coupon	Yield Stress (MPa)	Ultimate Strength (MPa)
1	253	404
2	263	429
3	265	462
Average	260	432

The overall dimensions of the bridge towers are given in Figure 6.17, and the cross-sectional designs of the bridge towers at key locations are shown in Figure 6.18. The wall thickness of the hollow section from the actual bridge tower is between 800 mm and 1000 mm, which is scaled to 40 to 50 mm in the bridge model according to the similitude requirements. Thus, the wall thickness of the hollow section in the bridge model was taken as 50 mm to ease the fabrication process of the tower. RC footings were designed for the bridge towers and piers, and used to mount the entire model on the shake tables with threaded bars through reserved holes. One size of cross section was used for all the piers with 14 longitudinal rebars shown in Figure 6.19. Steel wires with 10 mm in diameter were used for cables of the bridge model, and anchored to the towers and main girder.

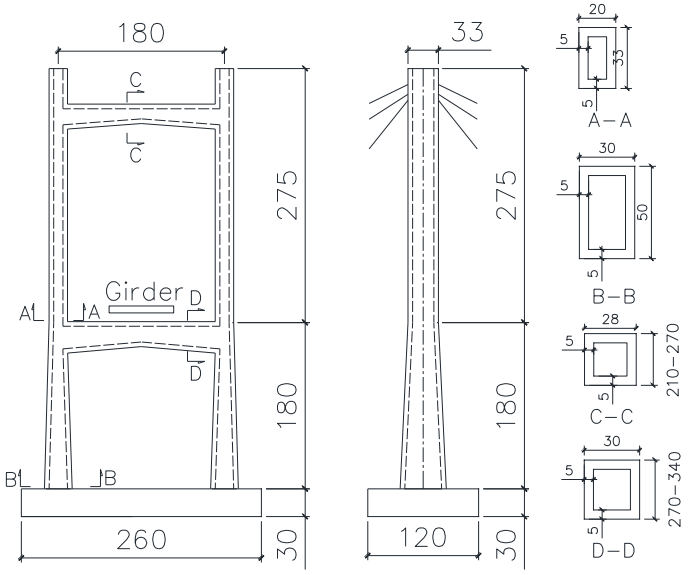

Figure 6.17. Tower design of the bridge model (unit: cm)

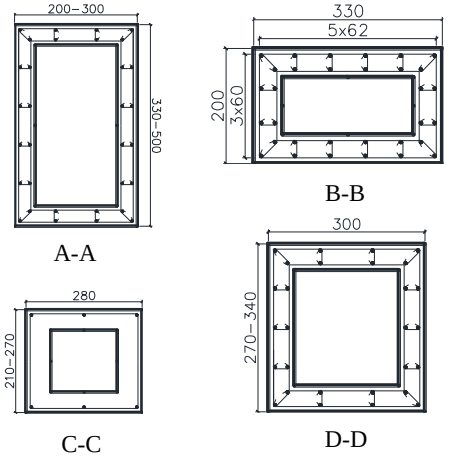

Figure 6.18. Reinforcement design of the bridge tower (unit: mm)

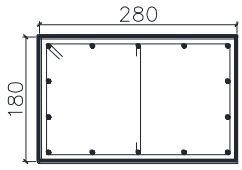

Figure 6.19. Reinforcement design of the bridge piers (unit: mm)

Due to the fact that inertia force is the major concern under earthquake excitations, the difference in material density between the actual bridge and the model must be taken

into consideration. To simulate the actual seismic behavior, masses were added to the bridge towers, piers and girder, as illustrated in Figure 6.20 in the case of the bridge towers. Each additional mass cube is 320 mm×330 mm×170 mm in size.

The fabrication process of the bridge model is illustrated in Figure 6.21. It began with the formation of reinforcement cage as shown in Figure 6.21(a). The concrete formwork was then built for the towers as shown in Figure 6.21(b). Next, concrete was cast and cured as shown in Figure 6.21(c), and the cured tower and pier were moved to and mounted on the shake tables, as shown in Figure 6.21(d-e). Extra weights were placed at the desired locations of these members as depicted in Figure 6.21(f), and the steel girder was hoisted into place as shown in Figure 6.21(g). Finally, the stay cables were mounted as detailed in Figure 6.21(h) and adjusted to desired forces (Figure 6.22).

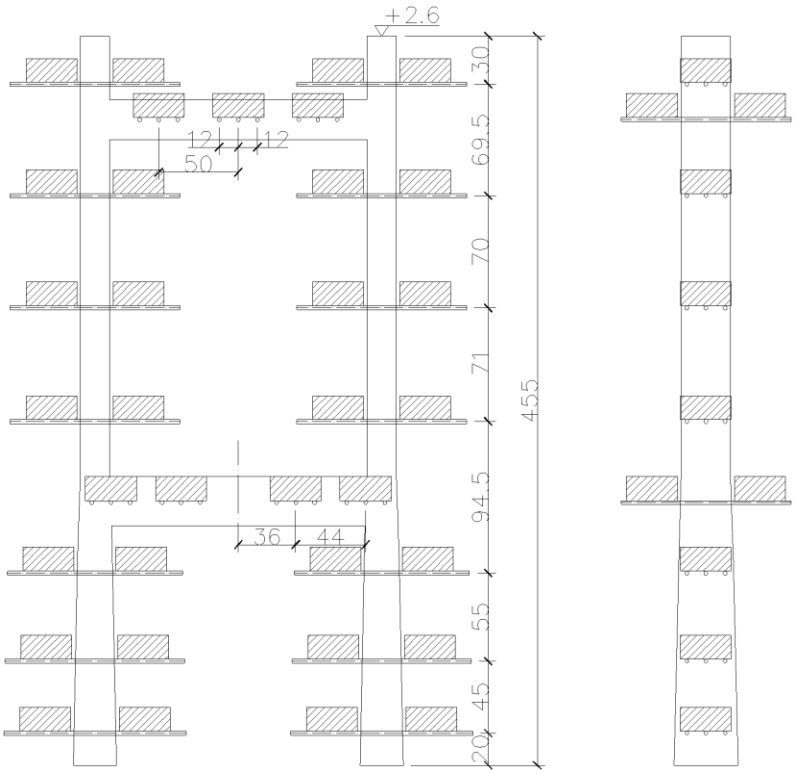

Figure 6.20. Added weights to the bridge towers

(a) Reinforcement cage of a bridge tower

(b) Establishment of concrete formwork

(c) Bridge towers and piers after curing

(d) Tower placement on shake table

(e) Pier placement on shake table

(f) Attachment of additional weights

(g) Placement of the bridge girder

(h) Installation of stay cables.

Figure 6.21. Photographs of construction process

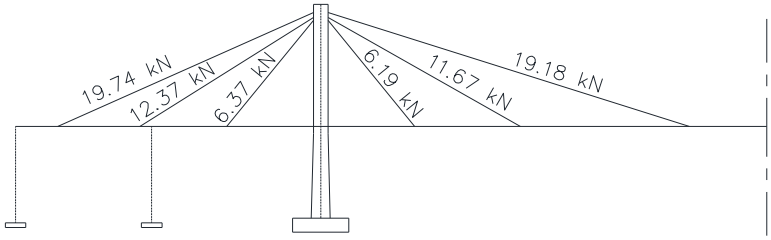

Figure 6.22. Adjusted stay cable forces

The bridge model was tested under the Chi-Chi earthquake wave with a peak ground acceleration (PGA) of $0.1g$ to $1.2g$ with an increment of $0.1g$. Between any two PGA levels, the same white noise excitation of $0.1g$ in peak acceleration was also applied to the bridge model for parameter identification. Displacement sensors and accelerometers were mounted along the bridge girder, towers and piers. Load cells were integrated into the anchors of stay cables, and strain gages were attached to the longitudinal reinforcement bars at the bottom portions of the towers and piers. In this study, only the accelerations at the key locations (TAY accelerometers) of the bridge towers, as shown in Figure 6.23, are analyzed. Here, TAY stands for the tower acceleration in Y (transverse) direction. In Figure 6.23, a designation, R (L), is also used, representing the right (left) tower of the model.

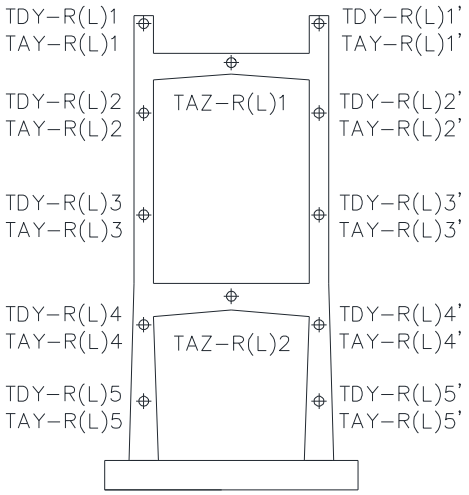

Figure 6.23. Sensor deployment of the bridge towers

6.3.2. Loading Protocol. In this study, the seismic excitation chosen is a modified wave of the Chi-Chi earthquake, which originally has a PGA of 0.138g and a strong motion duration of 40.9 s. The time of the modified wave is compressed based on a similitude of S_t=0.2236, and the PGA of the wave is adjusted to 0.1g to facilitate the incremental testing process. The modified earthquake wave is presented in Figure 6.24 with a strong motion of approximately 8 s and a peak of 0.1g. All the four shake tables were synchronized and subjected to the same excitations in the transverse direction, and no input in the longitudinal and vertical directions.

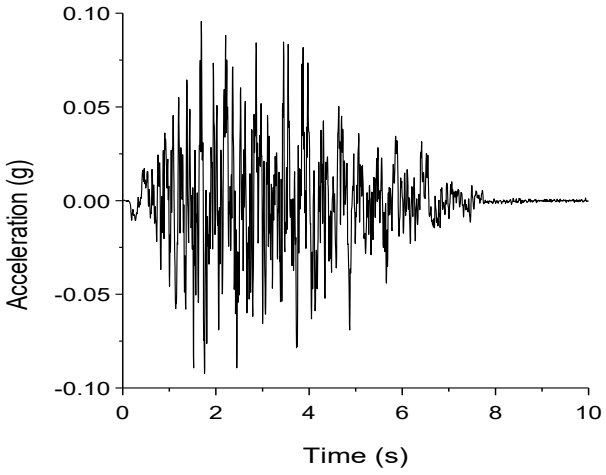

Figure 6.24. Earthquake wave

The incremental testing process is detailed in Table 6.4. For example, the process starts with a white noise of 0.1g in PGA over 30 s in a frequency bandwidth of 1-30 Hz. The modified wave with a PGA of 0.1g is then applied. Next, the white noise test at 0.1g PGA is repeated, and the modified wave is increased to 0.2g in PGA and applied to the bridge model. This process continues till a PGA of 1.2g has been achieved. Finally, the white noise test is repeated again.

Table 6.4. Testing process

Input	PGA (g)	Input	PGA (g)
White Noise 1	0.1	**Earthquake**	0.7
Earthquake	0.1	**White Noise 8**	0.1
White Noise 2	0.1	**Earthquake**	0.8
Earthquake	0.2	**White Noise 9**	0.1
White Noise 3	0.1	**Earthquake**	0.9
Earthquake	0.3	**White Noise 10**	0.1
White Noise 4	0.1	**Earthquake**	1.0
Earthquake	0.4	**White Noise 11**	0.1
White Noise 5	0.1	**Earthquake**	1.1
Earthquake	0.5	**White Noise 12**	0.1
White Noise 6	0.1	**Earthquake**	1.2
Earthquake	0.6	**White Noise 13**	0.1
White Noise 7	0.1	--	--

6.3.3. Test Data Interpretation. The frequency spectra of the white noise (WN) induced accelerations at TAY-R1 are presented in Figure 6.25. The first two transverse modes are successfully identified under the white noise excitations. Prior to the $0.8g$ earthquake input, the identified frequency (2.5 Hz) of the first mode changes little. At $0.9g$ PGA, the fundamental frequency starts to drop, corresponding to the cover concrete spalling at the lower end of the towers, and the exposure of transverse and longitudinal reinforcements. For the second mode, the frequency drop happens much earlier at approximately $0.4g$ in PGA, corresponding to concrete cracks. When the cracks are fully developed after a PGA of $0.8g$, the frequency value of the second mode becomes stable.

Although effective in identifying the change of the first two natural frequencies over time, white noise excitations are difficult to generate for large-scale civil infrastructures. Therefore, the dynamic responses of the bridge model under the earthquake excitations were analyzed to identify the system parameters or detect damage by means of AWT and AMD.

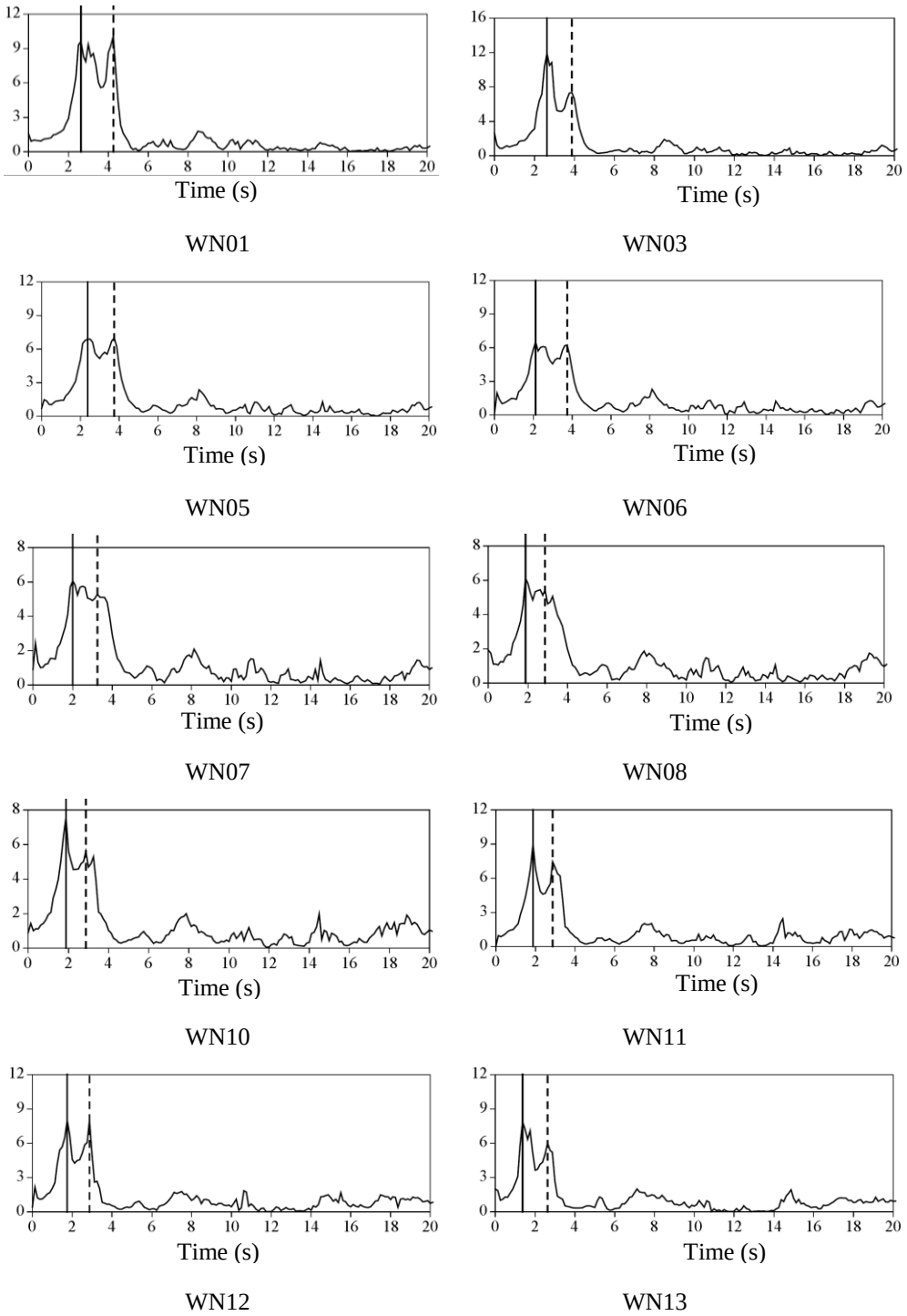

Figure 6.25. White noise induced accelerations at different input steps

Figure 6.26 shows the acceleration time history at the top of the tower (TAY-R1) and its time-frequency representation under the $0.6g$ earthquake excitation. The peak

acceleration occurs at approximately 4.1 s. Between 1 s and 4.1 s, both the first and second modes of vibration are significant due to the strong earthquake motion, as shown in Figure 6.24, and their frequencies are unchanged over time. At 4.1 s when the PGA occurs, the frequency of the first mode is reduced from 3 Hz to 2.5 Hz, indicating initial cracking at the base of the tower as observed during the test. After 4.1 s, the second mode of vibration becomes less significant likely due to the decreasing earthquake input energy at high frequencies.

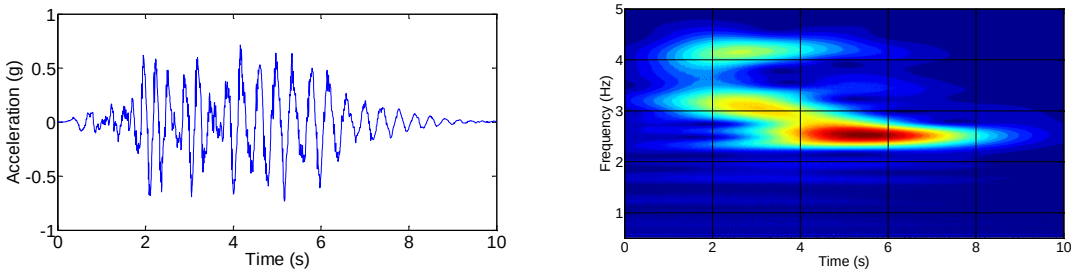

(a) Time history – signal in time domain (b) Time-frequency representation by AWT

Figure 6.26. TAY-R1 acceleration under the 0.6 g earthquake excitation

Based on the AWT of the acceleration response, as depicted in Figure 6.26(b), a bisecting frequency can be determined and AMD is applied to ensure success of the response decomposition. As demonstrated in Figures 6.27 and 6.28, the first and second vibration modes of the tower under the earthquake excitation are separated successfully. It is worth to note that the AMD also filters out the low-amplitude noise that is present in the AWT in Figure 6.26(b)). That is, Figures 6.27(b) and 6.28(b) show much cleaner time-frequency representations of the dynamic response for the approximate first and second modes of vibration. The M-AMD algorithm can thus be performed with better accuracy with the help of AWT and the denoising from AMD.

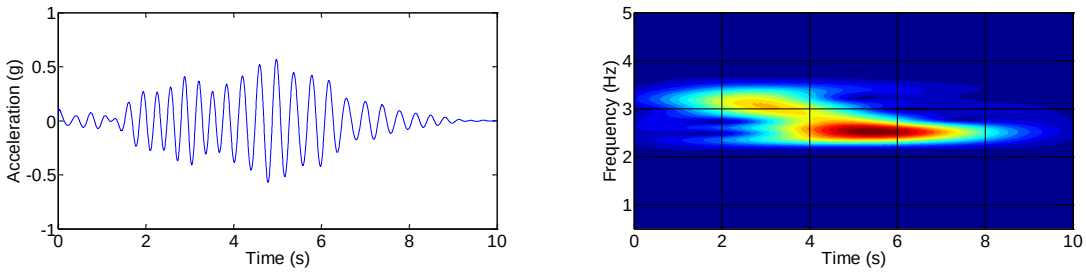

(a) Approximate modal acceleration (b) CWT

Figure 6.27. Decomposed acceleration for the first mode of vibration under the 0.6 g earthquake excitation

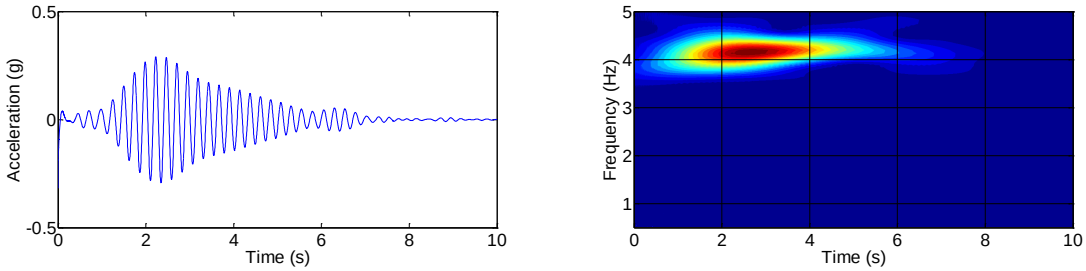

(a) Approximate modal acceleration (b) CWT

Figure 6.28. Decomposed acceleration for the second mode of vibration under the 0.6 g earthquake excitation

Figure 6.29 shows the acceleration response at the top of tower (TAY-R1) under the 1.2 g earthquake input. In comparison with the response under the 0.6 g earthquake excitation, as shown in Figure 6.26(a), the peak acceleration response in Figure 6.29(a) is more than twice, occurring at approximately 2.7 s, and the frequencies of the first and second modes are significantly lower. As shown in Figure 6.29(b), the frequency of the first mode changes little over time, while the frequency of the second mode drops from 3 Hz before 2.7 s to 2.7 Hz after approximately 4.1 s, which can also be observed from Figure 6.25 from WN12 to WN13. The frequency drop corresponds to the cover concrete spalling around the mid-height and bottom of the tower and partial separation of tower columns and beams due to core concrete crush and rebar fracture at each end of the tower beams.

Furthermore, the second mode of vibration appears more significant than that of the first mode, in terms of signal amplitude and energy.

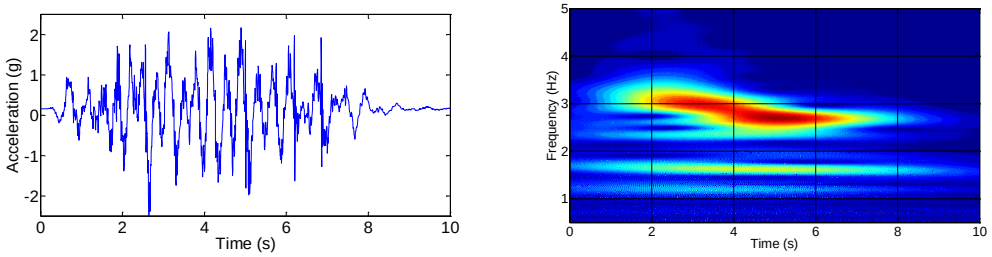

(a) Time history (b) Time-frequency representation by AWT

Figure 6.29. TAY-R1 acceleration under the 1.2 g earthquake excitation

Based on Figure 6.29(a), a bisecting frequency of 2 Hz between the first and second modes of vibration is selected in the AMD analysis. The decomposed and filtered signals are presented in Figures 6.30 and 6.31 for the first and second modes of vibration, respectively. With little or no mix of the vibration modes, the AMD successfully separates the two modes of vibration. By comparing Figure 6.31(a) with Figure 6.30(a), it can be seen that the second mode of vibration is significantly stronger than that of the first mode.

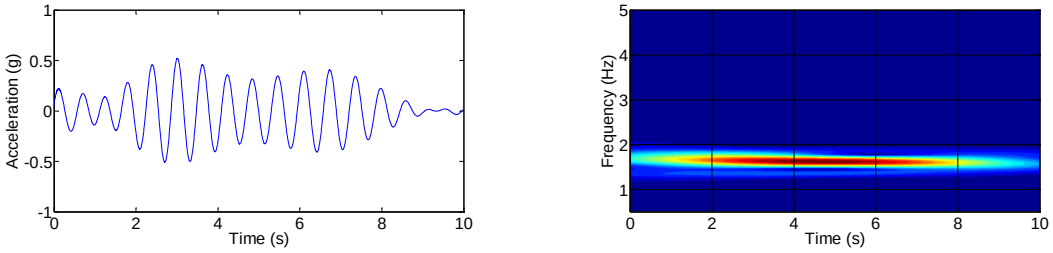

(a) Approximate modal acceleration (b) CWT

Figure 6.30. Decomposed acceleration for the first mode of vibration under the 1.2 g earthquake excitation

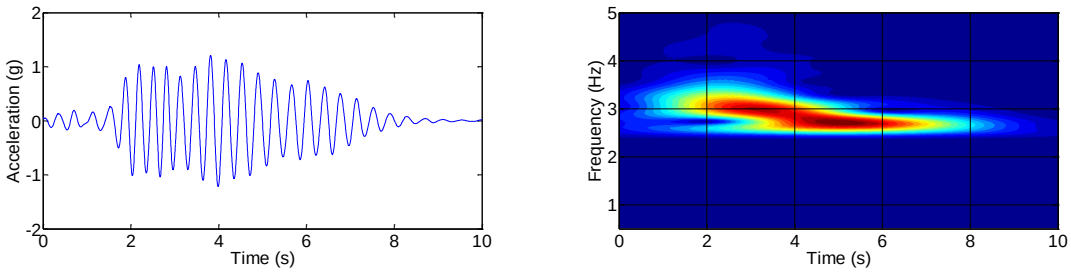

(a) Approximate modal acceleration response (b) CWT

Figure 6.31. Decomposed acceleration for the second mode of vibration under the 1.2 g earthquake excitation

M-AMD is also used to identify dynamic properties of the bridge model by considering the first mode of vibration of the tower to be a SDOF system. Following the same procedure as used in Section 5, the identified natural frequency and damping ratio under the 0.6g and 1.2g earthquake excitations are respectively presented in Figures 6.32 and 6.33.

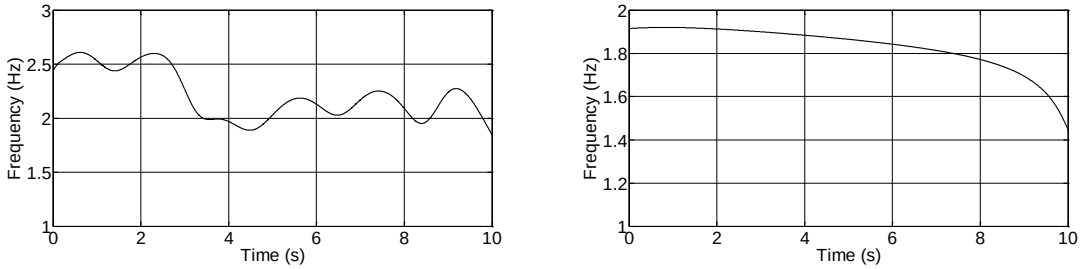

(a) 0.6 g earthquake input (b) 1.2 g earthquake input

Figure 6.32. M-AMD identified natural frequency of the first mode

The general trends of the frequency variations under the 0.6g and 1.2g earthquake excitations are similar to those seen from the AWT in Figures 6.27(b) and 6.30(b), as the frequency change over time does not contain fast-varying components. The damping ratio increases over time as the structural damage, such as concrete spalling and rebar yielding, is accumulated.

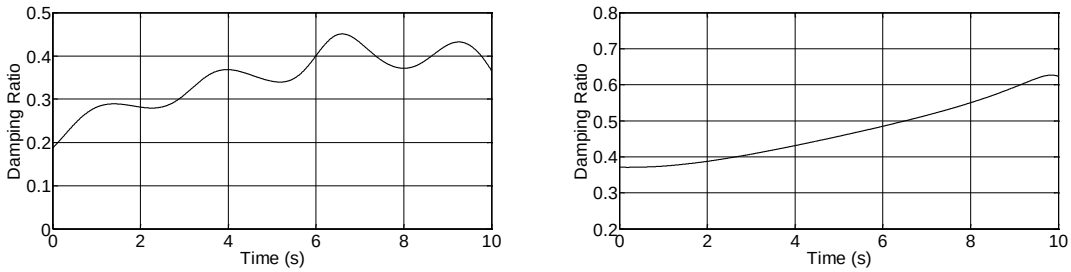

(a) 0.6 g earthquake input (b) 1.2 g earthquake input

Figure 6.33. M-AMD identified damping ratio of the first mode

6.4. SUMMARY

In this section, the optimized AMD has been developed to solve the mode mix issue when the original AMD is applied to a sampled/discretized data series. Its effectiveness has been demonstrated with sinusoidal, chirp and Duffing signals. By comparing the decomposed and theoretical signals, the errors in all three analytical examples are well below 10%, indicating satisfactory robustness and accuracy in the decomposition of frequency components.

Together with the AWT, the optimized AMD is applied for the damage detection and system identification of the 1/20-scale bridge model under earthquake excitations of various intensities. Although pre- and post-earthquake white noise excitations can be successfully used to identify the change in dynamic properties such as natural frequency and damping ration, the white noise test process is difficult, if not impossible, to execute in applications. Thus, this study is focused on the processing of earthquake responses. During each application, AWT is first applied to specific seismic responses of the bridge tower in order to identify each dominant mode of vibration. The time-varying or constant bisecting frequency can thus be determined from the time-frequency scalogram given by AWT. The optimized AMD is then performed to separate different modes of vibration. For

the first mode, M-AMD is implemented to further identify the changes of natural frequency and damping ratio more accurately. For the 1/20-scale bridge model, both the optimized AMD and M-AMD can detect damage from the reduction of natural frequencies of the first and second modes since the natural frequencies fluctuate slowly.

7. CONCLUSIONS

In this dissertation, the state-of-the-art signal processing techniques have been reviewed with an emphasis on the representation and decomposition. These techniques include Fourier transform, short-time Fourier transform, wavelet transform, Hilbert-Huang transform, Hilbert vibration decomposition, and analytical mode decomposition (AMD). In addition, nondestructive evaluation methods such as acoustic emission and impact echo have also been reviewed in detail as they are applied to detect structural damage. Challenges and critical issues identified with the previous methods include non-changeable time-frequency resolution over time, inaccurate identification of system parameters, and mode mix due to low sampling rate.

To address the above challenges and critical issues in structural health monitoring, three new algorithms have been proposed. First, the adaptive wavelet transform (AWT) is formulated with a fully automatic optimization strategy for the determination of a desirable time-frequency representation of signals and thus the extraction of engineering features. A flowchart of two optimization algorithms for time and frequency resolution updating is developed to identify center frequencies, scaling factors, and window lengths over time. Synchro-squeezing is then applied to the algorithm of AWT for more accurate representation. Second, the multiple analytical mode decomposition (M-AMD) is developed and applied for the system identification from both free and forced vibrations. It can correctly identify both the slow- and fast-varying damping and stiffness coefficients for nonlinear systems, which represents a significant advancement of the current methods in the literature. Third and last, the optimized AMD is developed to reduce or eliminate potential errors associated with the discretization of measured signals, depending upon the

sampling rate of date. The decomposed components no longer retain the mode mix issue after the optimization process.

AWT can provide an effective and efficient time-frequency representation of any signal as testified by the analytical, acoustic emission and impact echo signals analyzed in this study. The fully automatic optimization algorithm implemented as part of the transform improves the ability of identifying time-varying frequency components in nonstationary and nonlinear responses that occur in mechanical and structural systems. Due to the nature of wavelet transform, it can also capture the transient components (e.g. delta functions). For example, different types of acoustic emission signals from the cable tension tests are identified successfully for potential damage localization and classification. Impact echo signals obtained from the delaminated concrete slab are analyzed with high accuracy to detect the spatial distribution of delamination defects. By implementing the synchro-squeezing approach, AWT is taken to the next level of clearness and sharpness, where the dispersive curves from the conventional wavelet transform become thin lines. The improvement of synchro-squeezing AWT is also demonstrated from the analysis of the impact echo signals of the same concrete slab test with less number of false detections.

M-AMD involves the multiple applications of AMD for denoising and signal decomposition. M-AMD takes into account the high-frequency component of an instantaneous parameter identified from the dynamic response of a nonlinear system. The high-frequency component is often ignored in the literature, thus leading to an erroneous statement that the instantaneous parameter is equal to its corresponding parameter of the system. In fact, the two parameters differ in magnitude and trend over time. M-AMD also incorporates the Hilbert transform to formulate simultaneous equations for the explicit

solution of dynamic parameters. By taking advantage of the Hilbert transform and AMD, the time-varying damping (stiffness) coefficient of an oscillator is divided into slow- and fast-varying components by a bisecting frequency in reference to velocity (displacement). Both components can be successfully decomposed, and the system parameters can thus be correctly reconstructed.

For discrete time series as commonly encountered in engineering application, the original AMD method tends to distort the decomposed components of a certain signal due to the mode mix issue. To overcome this drawback, the optimized AMD is developed to ensure the robustness in use of AMD. The effectiveness of the optimization process is demonstrated by several analytical examples. The combined AWT and AMD are then applied to the recent shake table test data with significant damage of the cable-stayed bridge model, which represents the nonlinear behavior of a complex engineering system under extreme earthquake excitations. Damage can be effectively observed over time from the signals analyzed with the combined algorithm.

The slow-varying damping and stiffness components are estimated from the oscillator's responses and their Hilbert transforms, and filtered with the adaptive low-pass filter AMD. Each fast-varying component is estimated from the oscillator's responses and the determined slow-varying components, and corrected with AMD using an approximate bisecting frequency of the two fast-varying components.

While this study has demonstrated the effectiveness of the proposed methods in both signal representation and decomposition, there are still several aspects that need to be addressed in future research work for both the mathematical formulation and robustness in potential applications. They include:

(1) To further understand the characteristics of the proposed AWT, the signal reconstruction must be achieved by incorporating the inverse transform of AWT. The time-varying wavelet parameters (center frequency, scaling factor, and window length) give the challenge on the inverse transform, which needs to be further investigated.

(2) The application of M-AMD has been limited to SDOF nonlinear systems or MDOF systems with one nonlinear component only. In practical applications, however, nonlinear MDOF systems are of greater value. In addition, to effectively identify the system properties from incomplete measurements (e.g. nodal accelerations) is a topic of interest in the earthquake engineering community.

(3) The integration and validation of AWT and M-AMD in practical applications remains in infant stage. Although the analyzed data from the shake table test of a 1/20-scale bridge model proved effective in damage detection, the potential of the combined AWT and M-AMD has not yet been exploited to full extent, since the natural frequency and damping ration change slowly. Further investigation and application of the AWT and M-AMD expect to be fruitful.

BIBLIOGRAPHY

[1] Huang, Norden E., Zheng Shen, Steven R. Long, Manli C. Wu, Hsing H. Shih, Quanan Zheng, Nai-Chyuan Yen, Chi Chao Tung, and Henry H. Liu. "The empirical mode decomposition and the Hilbert spectrum for nonlinear and non-stationary time series analysis." In *Proceedings of the Royal Society of London A: Mathematical, Physical and Engineering Sciences* 454, no. 1971: 903-995, The Royal Society, 1998.

[2] Chen, Genda, and Zuocai Wang. "A signal decomposition theorem with Hilbert transform and its application to narrowband time series with closely spaced frequency components." *Mechanical Systems and Signal Processing* 28 (2012): 258-279.

[3] Daubechies, Ingrid, Jianfeng Lu, and Hau-Tieng Wu. "Synchrosqueezed wavelet transforms: an empirical mode decomposition-like tool." *Applied and Computational Harmonic Analysis* 30, no. 2 (2011): 243-261.

[4] Jacobsen, Eric, and Richard Lyons. "The sliding DFT." *IEEE Signal Processing Magazine* 20, no. 2 (2003): 74-80.

[5] Qian, Shie, and Dapang Chen. "Decomposition of the Wigner-Ville distribution and time-frequency distribution series." *IEEE Transactions on Signal Processing* 42, no. 10 (1994): 2836-2842.

[6] Huang, Norden E., Zheng Shen, and Steven R. Long. "A new view of nonlinear water waves: the Hilbert spectrum." *Annual Review of Fluid Mechanics* 31, no. 1 (1999): 417-457.

[7] Feldman, Michael. "Time-varying vibration decomposition and analysis based on the Hilbert transform." *Journal of Sound and Vibration* 295, no. 3 (2006): 518-530.

[8] Mallat, Stéphane. *A Wavelet Tour of Signal Processing*. Academic Press, 1999.

[9] Lilly, Jonathan M., and Sofia C. Olhede. "On the analytic wavelet transform." *IEEE Transactions on Information Theory* 56, no. 8 (2010): 4135-4156.

[10] Ghanem, Roger, and Francesco Romeo. "A wavelet-based approach for the identification of linear time-varying dynamical systems." *Journal of Sound and Vibration* 234, no. 4 (2000): 555-576.

[11] Zhang, Qinghua, and Albert Benveniste. "Wavelet networks." *IEEE Transactions on Neural Networks* 3, no. 6 (1992): 889-898.

[12] Holland, John Henry. *Adaptation in Natural and Artificial Systems: An Introductory Analysis with Applications to Biology, Control, and Artificial Intelligence*. MIT press, 1992.

[13] Nazimov, A. I., A. N. Pavlov, A. E. Hramov, V. V. Grubov, E. Yu Sitnikova, and A. A. Koronovskii. "Adaptive wavelet transform-based method for recognizing characteristic oscillatory patterns." *Journal of Communications Technology and Electronics* 58, no. 8 (2013): 790-795.

[14] Wang, Chao, Wei-Xin Ren, Zuo-Cai Wang, and Hong-Ping Zhu. "Instantaneous frequency identification of time-varying structures by continuous wavelet transform." *Engineering Structures* 52 (2013): 17-25.

[15] Li, Chuan, and Ming Liang. "A generalized synchrosqueezing transform for enhancing signal time–frequency representation." *Signal Processing* 92, no. 9 (2012): 2264-2274.

[16] Feldman, Michael. "Investigation of the natural vibrations of machine elements using the Hilbert transform." *Soviet Machine Science* 2, no. 0739-8999 (1985): 3.

[17] Feldman, Michael. "Non-linear system vibration analysis using Hilbert transform--I. Free vibration analysis method 'FREEVIB'." *Mechanical Systems and Signal Processing* 8, no. 2 (1994): 119-127.

[18] Feldman, Michael. "Non-linear system vibration analysis using Hilbert transform--II. Forced vibration analysis method 'FORCEVIB'." *Mechanical Systems and Signal Processing* 8, no. 3 (1994): 309-318.

[19] Feldman, Michael. "Non-linear free vibration identification via the Hilbert transform." *Journal of Sound and Vibration* 208, no. 3 (1997): 475-489.

[20] Huang, Norden E., Man-Li C. Wu, Steven R. Long, Samuel SP Shen, Wendong Qu, Per Gloersen, and Kuang L. Fan. "A confidence limit for the empirical mode decomposition and Hilbert spectral analysis." In *Proceedings of the Royal Society of London a: Mathematical, Physical and Engineering Sciences*, vol. 459, no. 2037, pp. 2317-2345. The Royal Society, 2003.

[21] Liu, Bao, S. Riemenschneider, and Y. Xu. "Gearbox fault diagnosis using empirical mode decomposition and Hilbert spectrum." *Mechanical Systems and Signal Processing* 20, no. 3 (2006): 718-734.

[22] Chen, H. G., Y. J. Yan, and J. S. Jiang. "Vibration-based damage detection in composite wingbox structures by HHT." *Mechanical Systems and Signal Processing* 21, no. 1 (2007): 307-321.

[23] Yang, Jann N., Ying Lei, Shuwen Pan, and Norden Huang. "System identification of linear structures based on Hilbert–Huang spectral analysis. Part 1: normal modes." *Earthquake Engineering & Structural Dynamics* 32, no. 9 (2003): 1443-1467.

[24] Yang, Jann N., Ying Lei, Shuwen Pan, and Norden Huang. "System identification of linear structures based on Hilbert–Huang spectral analysis. Part 2: Complex modes." *Earthquake Engineering & Structural Dynamics* 32, no. 10 (2003): 1533-1554.

[25] Yang, Jann N., Yu Lei, S. Lin, and N. Huang. "Hilbert-Huang based approach for structural damage detection." *Journal of Engineering Mechanics* 130, no. 1 (2004): 85-95.

[26] Chen, J., and Y. L. Xu. "Identification of modal damping ratios of structures with closely spaced modal frequencies." *Structural Engineering and Mechanics* 14, no. 4 (2002): 417-434.

[27] Peng, Z. K., W. Tse Peter, and F. L. Chu. "An improved Hilbert–Huang transform and its application in vibration signal analysis." *Journal of Sound and Vibration* 286, no. 1 (2005): 187-205.

[28] Chen, Yangbo, and Maria Q. Feng. "A technique to improve the empirical mode decomposition in the Hilbert-Huang transform." *Earthquake Engineering and Engineering Vibration*2, no. 1 (2003): 75-85.

[29] Wang, Wei. "Decomposition of wave groups with EMD method." *The Hilbert-Huang Transform in Engineering* (2005): 267-280.

[30] Zhang, Qinghua, and Albert Benveniste. "Wavelet networks." *IEEE Transactions on Neural Networks* 3, no. 6 (1992): 889-898.

[31] Braun, S., and M. Feldman. "Decomposition of non-stationary signals into varying time scales: Some aspects of the EMD and HVD methods." *Mechanical Systems and Signal Processing* 25, no. 7 (2011): 2608-2630.

[32] Feldman, Michael. "Considering high harmonics for identification of non-linear systems by Hilbert transform." *Mechanical Systems and Signal Processing* 21, no. 2 (2007): 943-958.

[33] Davis, Allen G., Kevin L. Rens, Terry J. Wipf, and F. Wayne Klaiber. "Review of nondestructive evaluation techniques of civil infrastructure." *Journal of Performance of Constructed Facilities* 13, no. 1 (1999): 47-48.

[34] Holford, Karen Margaret, A. W. Davies, R. Pullin, and D. C. Carter. "Damage location in steel bridges by acoustic emission." *Journal of Intelligent ,Material Systems and Structures* 12, no. 8 (2001): 567-576.

[35] Gong, Z., E. O. Nyborg, and G. Oommen. "Acoustic emission monitoring of steel railroad bridges." *NDT and E International*6, no. 28 (1995): 392.

[36] Lozev, Margarit G. *Acoustic Emission Monitoring of Steel Bridge Members*. No. FHWA/VTRC 97-R13. 1997.

[37] Colombo, S., M. C. Forde, I. G. Main, J. Halliday, and M. Shigeishi. "AE energy analysis on concrete bridge beams." *Materials and Structures* 38, no. 9 (2005): 851-856.

[38] Brandt, A. M., J. Olek, M. A. Glinicki, C. K. Y. Leung, and J. Lis. "The application of acoustic emission to diagnose the destruction process in FSD cement composites." *Brittle Matrix Composites*: 299.

[39] Ramadan, Salah, Laurent Gaillet, C. Tessier, and Hassane Idrissi. "Detection of stress corrosion cracking of high-strength steel used in prestressed concrete structures by acoustic emission technique." *Applied Surface Science* 254, no. 8 (2008): 2255-2261.

[40] Mangual, Jesé, Mohamed K. ElBatanouny, Paul Ziehl, and Fabio Matta. "Acoustic-Emission-Based Characterization of Corrosion Damage in Cracked Concrete with Prestressing Strand." *ACI Materials Journal* 110, no. 1 (2013).

[41] Rizzo, Piervincenzo, and Francesco Lanza di Scalea. "Acoustic emission monitoring of CFRP cables for cable-stayed bridges." In *Proceedings SPIE*, vol. 4, no. 337, pp. 129-138. 2001.

[42] Rizzo, P., and F. Lanza di Scalea. "Acoustic emission monitoring of carbon-fiber-reinforced-polymer bridge stay cables in large-scale testing." *Experimental Mechanics* 41, no. 3 (2001): 282-290.

[43] Kretz, Thierry, Pierre Brevet, Christian Cremona, Bruno Godart, and Pierre Paillusseau. "Continuous monitoring and structural assessment of the Aquitaine suspension bridge." *Bull LPC* (2006): 13-32.

[44] Li, D., and J. Ou. "Acoustic emission monitoring and critical failure identification of bridge cable damage [6934-19]." In *Proceedings-SPIE The International Society for Optical Engineering*, vol. 6934, p. 6934. International Society for Optical Engineering; 1999, 2008.

[45] Jin, Ting, Zhi Sun, and Li-Min Sun. "Acoustic emission monitoring of stayed cables based on wavelet analysis." In *The 15th International Symposium on: Smart Structures and Materials & Nondestructive Evaluation and Health Monitoring*, pp. 693236-693236. International Society for Optics and Photonics, 2008.

[46] Betti, Raimondo, Matthew Jake Deeble Sloane, Dyab Khazem, and Claudio Gatti. "Monitoring the structural health of main cables of suspension bridges." *Journal of Civil Structural Health Monitoring* 6, no. 3 (2016): 355-363.

[47] Casey, N. F., and P. A. A. Laura. "A review of the acoustic-emission monitoring of wire rope." *Ocean Engineering* 24, no. 10 (1997): 935-947.

[48] Website Article. Mistras Monitoring Suspension Cables on Major Ohio Bridge [Internet]. 2011 [Cited 22 March 2017]. Available from: http://www.physicalacoustics.com/pac-ae-newsletter/mistras-monitoring-suspension-cables-on-major-ohio-bridge/

[49] Paulson, P. "Evaluation of Continuous Acoustic Monitoring as a Means of Detecting Failures in Post-tensioned and Suspension Bridges." In *Proc. of the XII-Ith FIP Congress, London*, vol. 2, pp. 657-659. 1998.

[50] Drummond, G., J. F. Watson, and P. P. Acarnley. "Acoustic emission from wire ropes during proof load and fatigue testing." *NDT & E International* 40, no. 1 (2007): 94-101.

[51] Woodward, R. J. "Detecting fractures in steel cables." *Wire Industry* 56, no. 401406 (1989): 18.

[52] Sun, Limin, and Ji Qian. "Experimental study on wire breakage detection by acoustic emission." *Frontiers of Architecture and Civil Engineering in China* 5, no. 4 (2011): 503-509.

[53] Zejli, Hasnae, A. Laksimi, C. Tessier, L. Gaillet, and S. Benmedakhene. "Detection of the broken wires in the cables' hidden parts (anchorings) by acoustic emission." In *Advanced Materials Research*, vol. 13, pp. 345-350. Trans Tech Publications, 2006.

[54] Oskouei, A. R., M. Ahmadi, and M. Hajikhani. "Wavelet-based acoustic emission characterization of damage mechanism in composite materials under mode I delamination at different interfaces." *Express Polym Lett* 3, no. 12 (2009): 804-813.

[55] Hamstad, M. A., A. O'GALLAGHER, and J. Gary. "A wavelet transform applied to acoustic emission." *Journal of Acoustic Emission* 20 (2002): 39-61.

[56] Yoon, Dong-Jin, W. Jason Weiss, and Surendra P. Shah. "Assessing damage in corroded reinforced concrete using acoustic emission." *Journal of Engineering Mechanics* 126, no. 3 (2000): 273-283.

[57] Grosse, Christian U., Florian Finck, Jochen H. Kurz, and Hans W. Reinhardt. "Improvements of AE technique using wavelet algorithms, coherence functions and automatic data analysis." *Construction and Building Materials* 18, no. 3 (2004): 203-213.

[58] Qi, Gang, Alan Barhorst, Javad Hashemi, and Girish Kamala. "Discrete wavelet decomposition of acoustic emission signals from carbon-fiber-reinforced composites." *Composites Science and Technology* 57, no. 4 (1997): 389-403.

[59] Qi, Gang. "Wavelet-based AE characterization of composite materials." *NDT & E International* 33, no. 3 (2000): 133-144.

[60] Lu, Chao, Peng Ding, and Zhenhua Chen. "Time-frequency analysis of acoustic emission signals generated by tension damage in CFRP." *Procedia Engineering* 23 (2011): 210-215.

[61] Xu, Changhang, Suping Ai, Jing Xie, Guoming Chen, and Changji Li. "Fatigue Failure Process Characterization for Carbon Fiber Sheet Reinforced Steel Rods Using the Acoustic Emission Technique." *Journal of Nondestructive Evaluation*35, no. 2 (2016): 24.

[62] Carino, Nicholas J., Mary Sansalone, and Nelson N. Hsu. "Flaw detection in concrete by frequency spectrum analysis of impact-echo waveforms." *International Advances in Nondestructive Testing* 12 (1986): 117-146.

[63] Sansalone, Mary J., and William B. Streett. "Impact-echo. Nondestructive evaluation of concrete and masonry." (1997).

[64] Sansalone, Mary, and Nicholas J. Carino. "Impact-echo method." *Concrete International* 10, no. 4 (1988): 38-46.

[65] Sansalone, Mary, and Nicholas J. Carino. "Detecting delaminations in concrete slabs with and without overlays using the impact-echo method." *Materials Journal* 86, no. 2 (1989): 175-184.

[66] Sansalone, M. "Detecting delaminations in concrete bridge decks with and without asphalt overlays using an automated impact-echo field system." In *Conference Proceedings of The British Institute of Non-Destructive Testing International Conference, NDT in Civil Engineering 14-16 April 1993, Liverpool University. Volume 2*. 1993.

[67] Gucunski, Nenad, Strahimir Antoljak, and Ali Maher. "Seismic methods in post construction condition monitoring of bridge decks." In *Use of Geophysical Methods in Construction*, pp. 35-51. 2000.

[68] Yuan, D., and S. Nazarian. "Feasibility of detecting flaws in concrete walls of nuclear power plants." *The Center for Highway Materials Research, University of Texas at El Paso, El Paso* (2000).

[69] Azari, Hoda, Deren Yuan, Soheil Nazarian, and Nenad Gucunski. "Sonic methods to detect delamination in concrete bridge decks: Impact of testing configuration and data analysis approach." *Transportation Research Record: Journal of the Transportation Research Board* 2292 (2012): 113-124.

[70] Malik, M. A., and J. Saniie. "Gabor transform with optimal time-frequency resolution for ultrasonic applications." In *Ultrasonics Symposium, 1998. Proceedings., 1998 IEEE*, vol. 1, pp. 817-820. IEEE, 1998.

[71] Song, Ki-Il, and Gye-Chun Cho. "Numerical study on the evaluation of tunnel shotcrete using the Impact-Echo method coupled with Fourier transform and short-time Fourier transform." *International Journal of Rock Mechanics and Mining Sciences* 47, no. 8 (2010): 1274-1288.

[72] Shokouhi, P., N. Gucunski, and A. Maher. "Time–frequency techniques for the impact-echo data analysis and interpretations." In *Proceedings of the 9th European NDT Conference (ECNDT 2006), Berlin*. 2006.

[73] Bouden, Toufik, Fares Djerfi, Samira Dib, Mokhtar Nibouche, and Toufik Benkedidah. "Improving Hilbert Huang and wavelet transforms for the impact-echo method of NDT." *Journal of Automatic System Engineering* 6, no. 4 (2012): 172-184.

[74] Chiang, C. H., and C. C. Cheng. "Detecting rebars and tubes inside concrete slabs using continuous wavelet transform of elastic waves." *Journal of Mechanics* 20, no. 4 (2004): 297-302.

[75] Yeh, Po-Liang, and Pei-Ling Liu. "Application of the wavelet transform and the enhanced Fourier spectrum in the impact echo test." *NDT & E International* 41, no. 5 (2008): 382-394.

[76] Epasto, Gabriella, E. Proverbio, and V. Venturi. "Evaluation of fire-damaged concrete using impact-echo method." *Materials and Structures* 43, no. 1-2 (2010): 235.

[77] Celaya, Manuel, Parisa Shokouhi, and Soheil Nazarian. "Assessment of debonding in concrete slabs using seismic methods." *Transportation Research Record: Journal of The Transportation Research Board* 2016 (2007): 65-75.

[78] Auger, François, and Patrick Flandrin. "Improving the readability of time-frequency and time-scale representations by the reassignment method." *IEEE Transactions on Signal Processing* 43, no. 5 (1995): 1068-1089.

[79] Qu, Hongya, Mengxing Li, Genda Chen, Lesley H. Sneed, and Neil L. Anderson. "Multi-bandwidth wavelet transform of impact echo signals for delamination detection of thin concrete slabs." *Journal of Civil Structural Health Monitoring* 6, no. 4 (2016): 649-664.

[80] Zhu, Jinying, and John S. Popovics. "Imaging concrete structures using air-coupled impact-echo." *Journal of Engineering Mechanics* 133, no. 6 (2007): 628-640.

[81] Kee, Seong-Hoon, and Nenad Gucunski. "Interpretation of flexural vibration modes from impact-echo testing." *Journal of Infrastructure Systems* 22, no. 3 (2016): 04016009.

[82] Cheng, C., and Mary Sansalone. "The impact-echo response of concrete plates containing delaminations: numerical, experimental and field studies." *Materials and Structures* 26, no. 5 (1993): 274-285.

[83] Gibson, Alexander, and John S. Popovics. "Lamb wave basis for impact-echo method analysis." *Journal of Engineering Mechanics* 131, no. 4 (2005): 438-443.

[84] Shin, Sung Woo, Chung-Bang Yun, John S. Popovics, and Jae Hong Kim. "Improved Rayleigh wave velocity measurement for nondestructive early-age concrete monitoring." *Research in Nondestructive Evaluation* 18, no. 1 (2007): 45-68.

[85] Bedrosian, Edward. *A Product Theorem for Hilbert Transforms*. (1962).

[86] Charalampakis, A. E., and V. K. Koumousis. "On the response and dissipated energy of Bouc–Wen hysteretic model." *Journal of Sound and Vibration* 309, no. 3 (2008): 887-895.

[87] Constantinou, Michalakis C., and Mahmoud C. Kneifati. "Dynamics of soil-base-isolated-structure systems." *Journal of Structural Engineering* 114, no. 1 (1988): 211-221.

[88] Chen, Chaoqiang, and Genda Chen. "Shake table tests of a quarter-scale three-storey building model with piezoelectric friction dampers." *Structural Control and Health Monitoring* 11, no. 4 (2004): 239-257.

[89] Clough, R. W., and J. Penzien. *Dynamics Of Structures, Vol. 2*. McGraw-Hill New York (1993).

[90] Garrett, Gabriel T., Genda Chen, Franklin Y. Cheng, and Wayne Huebner. "Experimental characterization of piezoelectric friction dampers." In *Smart Structures and Materials 2001: Smart Systems for Bridges, Structures, and Highways*, vol. 4330, pp. 405-416. International Society for Optics and Photonics, 2001.

[91] Chen, Genda, and Chaoqiang Chen. "Semiactive control of the 20-story benchmark building with piezoelectric friction dampers." *Journal of Engineering Mechanics* 130, no. 4 (2004): 393-400.

[92] Anson, M., J. M. Ko, and E. S. S. Lam. "Building hazard mitigation with piezoelectric friction dampers." In *Advances in Building Technology: Proceedings of the International Conference on Advances in Building Technology, 4-6 December, 2002, Hong Kong, China*, vol. 1, p. 465. Elsevier Science, 2002.

[93] Wang, Ruilong, Yan Xu, and Jianzhong Li. "Transverse seismic behavior studies of a medium span cable-stayed bridge model with two concrete towers." *Journal of Earthquake Engineering* 21, no. 1 (2017): 151-168.

VITA

Hongya Qu was born in Changchun of Jilin Province, China. He moved to Dalian of Liaoning Province at the age of 6, where he received his elementary and secondary education. He received his Bachelor of Science (B.S.) degree in Civil Engineering in July 2009 and Master of Science (M.S.) degree in Bridge and Tunnel Engineering in July 2012, both from Tongji University, Shanghai, China. During his graduate study at Tongji, his main research activities involved the seismic study of bridge structures and finite element analysis.

In 2013, he enrolled as a Ph.D. student in the Department of Civil, Architectural, and Environmental Engineering at Missouri S&T. In the course of his study, he was involved in several projects, including "Analytical Mode Decomposition of Structural Dynamic Response for the Detection of Damage" and "Breaking Wire Detection and Strain Distribution of Seven-Wire Steel Cables with Acoustic Emission and Optical Fiber Sensors". These projects were supported in part by National Science Foundation (NSF) and by Missouri S&T. His main research work was focused on structural data analysis, engineering interpretation, system identification and damage detection. He published four journal papers and had three additional papers under review.

In May 2018, he received his Ph.D. in Civil Engineering from Missouri University of Science and Technology.